

**APPLICATION OF FINITE
VOLUME METHOD FOR SOLVING
FLUID STRUCTURE INTERACTION PROBLEM**

by

MD. MAHBUBAR RAHMAN

**MASTER OF PHILOSOPHY
IN
MATHEMATICS**



Department of Mathematics
**BANGLADESH UNIVERSITY OF ENGINEERING AND
TECHNOLOGY, DHAKA.**

April, 2008

The thesis titled
**Application of Finite Volume Method for Solving Fluid Structure
Interaction Problem**

Submitted by

Md. Mahbubar Rahman

Student No. 040509002, Registration No. 0405402, Session: April-2005. a part time student of M. Phil. (Mathematics) has been accepted as satisfactory in partial fulfillment for the degree of

Master of Philosophy in Mathematics

April 26, 2008


BOARD OF EXAMINERS

A. Alim

1. Dr. Md. Abdul Alim
Assistant Professor
Dept. of Mathematics, BUET, Dhaka.
Chairman
(Supervisor)
2. Dr. Md. Mashud Karim
Associate Professor
Dept. Naval Architecture and Marine Eng., BUET,
Dhaka.
Member
(Co-Supervisor)
3. Dr. Md. Abdul Maleque
Professor & Head of the Dept.
Dept. of Mathematics, BUET, Dhaka.
Member
(Ex-Officio)
4. Dr. Md. Mustafa Kamal Chowdhury
Professor
Dept. of Mathematics, BUET, Dhaka.
Member
5. Dr. Md. Shahjada Tarafder
Associate Professor
Dept. of Naval Architecture and Marine Eng., BUET,
Dhaka.
Member
(External)

DECLARATION

It is hereby declared that this thesis or any part of it has not been submitted elsewhere for the award of any degree or diploma.



Md. Mahbubur Rahman

ACKNOWLEDGEMENT

I would like to thank all of the people who helped me making this thesis possible. First and foremost my gratitude goes to my esteemed supervisors Dr. M. A. Alim, Assistant Professor, Department of Mathematics and Dr. Md. Mashud Karim, Associate Professor, Department of Naval Architecture and Marine Engineering, Bangladesh University of Engineering and Technology, Dhaka, Bangladesh. Especially, I acknowledge my indebtedness to Dr. Karim for his tireless guidance and support throughout the research. His time input and advise was of immense help in completing this thesis in due time and I will be ever grateful to him

Besides I would like to be grateful to all of my teachers in the Department of Mathematics, BUET, for their kind help and cooperation.

I would like to express cordial thanks to my colleagues and friends in Stamford University, Bangladesh for their support and cooperation at different times.

I must mention here that the researchers listed in the reference section and the members of Fluent User Forum (FUF) with whom I have exchanged ideas through internet, especially Dr. David Glenn, who provided me the important research reports.

Moreover I would be pleased to my family members, specially my wife and son, because of their sacrifice, cooperation and mental support during my research.

Above all, all thanks are due to Almighty Allah for making things and situations congenial and favorable for me for the task undertaken.

ABSTRACT

Two-dimensional Finite Volume Method (FVM) has been applied to solve Fluid Structure Interaction (FSI) problems in this research work. The numerical solutions of the governing equations have been obtained using commercial CFD software package FLUENT 6.2. Circular cylinder and four axisymmetric bodies of revolution, such as, sphere, DREA standard submarine bare hull, pod and underwater vehicle hull forms based on Gortler's geometry are used as test cases for this study. In case of circular cylinder, steady laminar flow at Reynold's number of 20 and 40, unsteady laminar flow at $Re=100$ and turbulent flow at $Re =1000$ and 3900 are simulated. Three turbulence models, namely, standard $k-\epsilon$, realizable $k-\epsilon$, shear stress transport (SST) $k-\omega$ are used to capture turbulent flow. Two-dimensional axisymmetric flow solver has been used to analyze turbulent flow around sphere, DREA submarine bare hull, pod and underwater vehicle hull forms at Reynold's number of 5×10^6 , 2.3×10^7 , 3×10^6 and 2×10^7 respectively. For sphere, Spalart-Allmaras (S-A) and shear stress transport (SST) $k-\omega$ turbulence models and for all other axisymmetric bodies, only shear stress transport (SST) $k-\omega$ turbulence model are used. The numerical results in terms of the skin friction coefficient, pressure coefficient and drag coefficient for different Reynold's numbers have been shown either graphically or in the tabular form. Velocity vectors as well as contour of pressure distribution have also been displayed graphically. The computed results show good agreement with the experimental measurements/numerical results obtained by other researchers.

CONTENTS

DECLARATION	iii
DEDICATION	iv
ACKNOWLEDGEMENT	v
ABSTRACT	vi
NOMENCLATURE.....	x
LIST OF TABLES	xii
LIST OF FIGURES.....	xiii
CHAPTER 1	1
1. INTRODUCTION	1
1.1 Computational Fluid Dynamics in Research and Development	1
1.2 Fluid Structure Interaction Problem and Its Importance	2
1.3 Previous Research	3
1.4 Research Objectives	6
CHAPTER 2	7
2. COMPUTATIONAL FLUID DYNAMICS MODELING CONSIDERATIONS	7
2.1 Discretization Methods in Computational Fluid Dynamics.....	7
2.1.1 Finite Difference Method (FDM).....	7
2.1.2 Finite Element Method (FEM).....	8
2.1.3 Finite Volume Method (FVM).....	8
2.2 Basics of Fluid Dynamics.....	8
2.3 Laminar and Turbulent Flow.....	9
2.4 Drag Forces.....	10
2.4.1 Viscous drag.....	11
2.4.2 Pressure drag and flow separation.....	12
2.5 Grid Generation.....	13
2.5.1 Solution dependence on grid	13
2.5.2 Structured grids	14
2.5.3 Unstructured grids	16
2.6 Two-Dimensional Versus Three-Dimensional Modeling	17
2.7 Steady-State versus Time-Varying Solution Techniques.....	17
CHAPTER 3	19

3. THEORETICAL BACKGROUND	19
3.1 Governing Equations	19
3.2 Solution using Finite Volume Method	20
3.2.1 Control volume faces location	20
3.2.2 Integration of the Transport Equation.....	22
3.2.3 Approximation of integrals.....	23
3.2.4 Interpolation.....	24
3.2.5 Linear equation system	25
3.2.6 Finite volume method for unsteady flow.....	26
3.2.7 Solution algorithm for pressure-velocity coupling.....	27
3.2.8 Implementation of boundary condition.....	30
3.3 Turbulence Modeling	33
3.3.1 The Spalart-Allmaras (S-A).....	37
3.3.2 The $k-\epsilon$ model	38
3.3.3 The $k-\omega$ model	40
3.4 Grid considerations for turbulent flow simulations (Y^+).....	42
3.5 2D Axisymmetric Model.....	43
CHAPTER 4.....	45
4. NUMERICAL SIMULATION.....	45
4.1 Simulation Using FLUENT 6.2 Based on Finite Volume Method	45
4.2 Laminar and Turbulent Flow over Circular Cylinder.....	46
4.2.1 Model geometry and boundary condition.....	46
4.2.2 Grid Generation	47
4.3 Axisymmetric Model Geometry and Grid Generation	49
4.3.1 Axisymmetric grid around sphere.....	49
4.3.2 Axisymmetric grid around DREA submarine bare hull	52
4.3.3 Axisymmetric grid around pod.....	53
4.3.4 Axisymmetric grid around underwater vehicle hull based on Gertler's geometry	54
4.4 Solver initialization and flow solution.....	55
CHAPTER 5.....	58
5. RESULT AND DISCUSSION.....	58
5.1 Definitions	58
5.2 Flow over Circular Cylinder.....	60
5.2.1 The laminar flow.....	60

5.2.2 The Turbulent Flow	63
5.2.3 Forces on the cylinder	71
5.3 Flow Around Axisymmetric Body of Revolution	77
5.3.1 Flow around sphere	77
5.3.2 Flow around DREA submarine bare hull	81
5.3.3 Flow around axisymmetric pod	87
5.3.4 Flow around underwater vehicle hull based on Gortler's geometry	92
CHAPTER 6.....	101
6. CONCLUSION AND RECOMMENDATIONS	101
6.1 Conclusion	101
6.2 Recommendations for further study	103
REFERENCE	104
APPENDICES.....	109
Appendix A:	109
Appendix B:	110
Appendix C:	111

NOMENCLATURE

\vec{A}	surface area vector
C_D	drag coefficient
C_f	frictional coefficient
C_p	pressure coefficient
C_{t1}, C_{t2}	turbulence constants
C_L	lift coefficient
d	diameter of the circular body
D	diameter of the slender body
D_m	cross-diffusion term
D_V	drag force
f	frequency of the vortex shedding
f_i	flux in the i th direction
F	convective flux
G_t	generation of turbulent kinetic energy
G_b	generation of turbulent kinetic energy due to buoyancy
\hat{G}_s	generation of turbulent kinetic energy due to mean velocity gradients
G_ω	generation of ω
G_ν	production of turbulent viscosity
I	turbulence intensity
k	turbulent kinetic energy
l	length scale
l_c	characteristic length
n	unit vector
N_{faces}	number of faces enclosing cell
p	pressure
Re	Reynolds number
S	reference area
S_u	user-defined source term (for S-A)
S_φ	source of φ per unit volume
St	Strouhal number

S_k, S_ϵ	user-defined source terms (for k - ϵ)
S_k, S_ω	user-defined source terms (for k - ω)
u, v	i th and j th velocity components in Cartesian coordinates
\vec{u}	flux
u'	Fluctuating velocity
V	cell volume
U_{avg}	mean flow velocity
U_{ref}	reference velocity
U	free stream velocity
x_i, x_j	i th and j th location components in Cartesian coordinates
Y_k, Y_ω	dissipation of k and ω due to turbulence
y	distance from wall surface
y^+	dimensionless parameter representing a local Reynold's number

Greek symbols

r	radial coordinate
ρ	density of fluid
ϕ	unknown parameter
ν	kinematic viscosity
ω	specific dissipation
ν	molecular kinematic viscosity
ϵ	turbulent dissipation
v_x	axial velocity
v_r	radial velocity
τ_η	momentum transport
τ_w	wall shear
$\bar{\nu}_t$	turbulent kinematic viscosity
ρ_{ref}	reference density
$\sigma_k, \sigma_\epsilon$	turbulent Prandtl numbers for k and ϵ respectively
ω_w	dimensionless wall vorticity
Γ_k, Γ_ω	effective diffusivity of k and ω respectively
τ_w	shear stress at the wall,
Γ_ϕ	diffusion coefficient for ϕ

LIST OF TABLES

Table No.	Caption	Page No.
4.1	Boundary Layer Parameters of Axisymmetric Sphere Grids	50
4.2	The Node Spacing of Sphere on the Edges of the Domains for Each Edge Node Distribution	50
4.3	Axisymmetric Sphere Boundary Node Spacing Distributions	50
4.4	Axisymmetric Submarine Boundary Node Spacing Distributions	53
4.5	Axisymmetric Pod Boundary Node Spacing Distributions	54
4.6	Distributions of Boundary Node Spacing of Axisymmetric Underwater Body Based on Gertler's Geometry	54
5.1	Components of Total Drag Coefficient	74
5.2	Comparison of Drag Coefficient at Different Reynolds Numbers	76
5.3	Angle of Separation for Axisymmetric Turbulent flow around Sphere	79
5.4	Drag Coefficient for Axisymmetric Turbulent Flow around Sphere	79
5.5	Drag Coefficient with Its Components for DREA Submarine Bare Hull	81
5.6	Run Parameters for Axisymmetric Viscous Model	87
5.7	Total Drag Coefficient with Its Component at $Re = 3 \times 10^6$ Computed on Pod Hull	88

Table No.	Caption	Page No.
5.8	The Frictional Coefficient of Pod	89
5.9	Computed Drag Coefficient Using Different Turbulence Model For Axisymmetric Body With $L/D=4$.	92
5.10	Computational Versus Experimental Results for Axisymmetric Bodies of Revolution Using SST $k-\omega$ Turbulence Model	93
5.11	Skin-Friction Coefficient as Percentage on Total Drag Coefficient for $L/D = 4-10$	94
5.12	Drag Coefficient ($C_D \times 10^{-3}$) from Different Prediction Methods at $Re = 2 \times 10^7$ For $L/D = 4-10$	94

LIST OF FIGURES

Figure No.	Caption	Page No.
2.1	(a)Laminar and (b) turbulent Path Line	9
3.1	2-D Cartesian Grid with General Notation in Finite Volume Method	21
3.2	The Upwind Differencing scheme	25
3.3	Flow Chart for PISO Algorithm	29
3.4	The Grid Arrangement at Boundaries of Finite Volume Method	31
4.1	Schematic Diagram of the Flow Field around Circular Cylinder with Boundary Condition	47
4.2	Grid Lines in Mesh: (a) Overall View,(b) Close-Up View Near the Cylinder.	48

4.3	(a) Axisymmetric Sphere Unstructured Grid With Boundary Conditions (b). Close Up View Near Boundary Layer of Sphere	51
4.4	DREA Bare Submarine Hull	52
4.5	Grid on DREA Bare Submarine Hull	53
4.6	2D- Axisymmetric Pod Grid	54
4.7	Grid of the Axisymmetric Underwater Body Based on Gertler's Geometry ($L/D=6$).	55
5.1	Stream Functions for (a) $Re = 20$ and (b) $Re = 40$	61
5.2	(a) Velocity Vectors for $Re = 20$ & 40 . (B) Velocity Vectors with Ray for $Re = 20$ & 40 .	62
5.3	Contours of Stream Function at (a) $T = 48.2s$, (b) $T = 51.2s$, (c) $T = 54.2s$ & (d) $T = 57.2s$ for $Re=100$	63
5.4	Contours of Stream Function at (a) $T = 48.2s$, (b) $T = 51.2s$, c) $T = 54.2s$ & (d) $T = 57.2s$ For $Re=100$	64
5.5	Contours of Static Pressure at (a) $T = 48.2s$, (b) $T = 51.2s$, (c) $T = 54.2s$ & (d) $T = 57.2s$ for $Re=100$	65
5.6	Strouhal Number Vs Reynolds Number	66
5.7	Stream Function (a) $T=120.12s$, (b) $T=121.80$ (c) $T=123.48s$, (d) $T=125.16s$ for $Re=1000$	67
5.8	Velocity Vector at (a) $T=120.12s$, (b) $T=121.80$ (c) $T=123.48s$, (d) $T=125.16s$ for $Re=1000$	68
5.9	Static Pressure at (a) $T=120.12s$, (b) $T=121.80$ (c) $T=123.48s$, (d) $T=125.16s$ for $Re=1000$	69
5.10	(a) Contours of Velocity Magnitude (b) Close up view of Flow around Circular Cylinder at $Re=3900$	70
5.11	Stream Function (a) $T=62.8s$, (b) $T=64.2s$, (c) $T=65.5s$ and (d) $T=66.9s$ for $Re=3900$	71
5.12	Contours of Vorticity Magnitude at (a) $T=62.8s$, (b) $T=64.2s$, (c) $T=65.5s$ and (d) $T=66.9s$ for $Re=3900$	72
5.13	Wall Vorticity Vs Angular Position	73

5.14	Pressure Coefficient Vs Angular Position	74
5.15	Time History of Lift Coefficient at $Re = 1000$	75
5.16	Time History of Drag Coefficient at $Re = 1000$	75
5.17	Drag Coefficient Vs Reynolds Number	76
5.18	Plot of Pressure Coefficient on the surface of Sphere at $Re = 5 \times 10^6$	77
5.19	Plot of Skin Friction Coefficient on the surface of Sphere at $Re = 5 \times 10^6$	78
5.20	(a) Velocity Vectors Around Sphere (b) Close Up View that Shows the Separation Point	80
5.21	(a) Contours of Pressure Coefficient for DREA Submarine Hull at $Re = 23$ Million	83
	(b) Close Up View of the Contours of Pressure Coefficient for DREA Submarine Hull	
5.22	(a) Contours of Velocity Magnitude for DREA Submarine Hull at $Re = 23$ Million	84
	(b) Close Up View of The Contours of Velocity Magnitude for DREA submarine Hull	
5.23	(a) Contours of Wall Shear Stress for DREA Submarine Hull at $Re = 23$ Million	83
	(b) Close Up View of the Rear Section of Contours of Wall Shear Stress for DREA Submarine Hull	
5.24	(a) Contours of Turbulence Kinetic Energy for DREA Submarine Hull at $Re = 23$ Million	86
	(b) Close Up View of Rear Section of the Contours of Turbulent Kinetic Energy for DREA Submarine Hull	
5.25	Time History of Drag Coefficient for Pod	89
5.26	Plots of y^+ of Pod for SST $k-\omega$ Model	90
5.27	Plots of Pressure Coefficient of Pod	90
5.28	Plots of Axial Velocity of Pod	91
5.29	Plots of Skin Friction Coefficient of Pod	91

5.30	Effect of L/D ratio on Skin-Friction Coefficient for Axisymmetric Body Based on Gertler's Geometry at $Re = 2 \times 10^7$	93-96
5.31	Effect of L/D ratio on Pressure Coefficient for Axisymmetric Body Based on Gertler's Geometry at $Re = 2 \times 10^7$	97-100

CHAPTER 1



1. INTRODUCTION

1.1 Computational Fluid Dynamics in Research and Development

Computational fluid dynamics (CFD) is one of the branches of fluid mechanics that uses numerical methods and algorithms to solve and analyze problems that involve fluid flows. Computers are used to perform the millions of calculations required to simulate the interaction of fluids and gases with the complex surfaces used in engineering. Whether in the private or public sector, research into fluid flow problems is necessary for the development of new fluid based systems. Computational Fluid Dynamics (CFD) has the power to model fluid flow and heat transfer in an abundance of situations. With the advent of more powerful computers and more comprehensive computer codes, CFD has come to the forefront as a legitimate and effective research tool. CFD analysis can be much more cost effective compared to experimental models since changes can be made quickly and easily to almost any characteristic of the simulation. Simulations can also be set up more quickly and easily than experimental methods. However, since it is a computer based solution technique, the results must be verified against experimental data. This seems counter intuitive since no profitable company or agency has the money to duplicate their experimentation. This is not entirely the case. Not every simulation needs to be compared with experimental values. Only a few base cases are compared for validation purposes and then it is assumed safe to say that the other CFD simulations in that range are valid. Even if some simulations are analyzed both experimentally and numerically, CFD is still beneficial since it has the ability to offer more information to researchers about the flow. CFD not only gives the overall values that experimentation offers, but gives a value at every node in the domain. If the overall values match, it can be assumed that all the detail described by the CFD solution is legitimate, giving researchers the ability to investigate small but important regions of the flow more closely.

Unfortunately, there are drawbacks to computational fluid dynamics as well. First, it can be difficult to model extremely complex physics accurately in all situations with current numerical algorithms. Boundary layer transition and separation are two phenomena that can be particularly troublesome to predict with a high degree of accuracy. Second, many problems must be simplified to make them tractable. With some problems, computer resources may not be available to solve the problem to the level of accuracy originally desired. Examples of problem simplification include modeling a three-dimensional problem as a two-dimensional or axisymmetric problem, reducing the computational domain size or solution resolution of a given flow field, or modeling a time-varying problem as a steady-state problem. Third, certain assumptions must be made to obtain a solution. Usually these assumptions appear as boundary conditions and are relatively accurate – examples are asymptotic behavior at far-field boundaries or prescribed inlet or exit conditions. Fourth, a particular solution algorithm might not produce a converged solution for a given flow field. In many cases, simply using intuition and applying specifically suited algorithms to the problem at hand can avoid this problem.

1.2 Fluid Structure Interaction Problem and Its Importance

The solution of Fluid Structure Interaction (FSI) problems using Computational Fluid Dynamics (CFD) analysis is now becoming tractable through the accessibility of high performance computing. Fluid structure interaction occurs when a fluid interacts with a solid structure, exerting pressure that may cause deformation in the structure and, thus, alter the flow of the fluid itself.

Fluid-Structure Interaction (FSI) problems are of great relevance to many fields in engineering and applied sciences. It has a wide range of application in many industrial and non-industrial fields such as aerospace industry, automobile industry, detonation wave effects on structure, underwater explosion, pressure vessel analysis, wind-force analysis on tall building etc.

Fluid Structure Interaction (FSI) problem is one of the most important topics in Naval Architecture, Offshore and Ocean Engineering. The ability to predict accurately fluid structure interaction is of fundamental importance for design, analysis and reconstruction in many areas of Naval Architecture and Ocean

engineering. A new area of research is the interaction between wave and flow problems, which occurs when structures, such as ships and platforms are positioned near each other or in the case of moored vessels.

The effect of FSI can be classified in two ways: one case is occurred when only the flow is affected for the interaction. In this study, this phenomenon is considered only for simplicity. The problem becomes complicated when the body is also moving or is flexible and may change its shape. The unsteady loading acting on the body in the flow may damage it. The lack of understanding the underlying phenomena related to fluid-structure interaction has caused to such catastrophes as the collapse of the 'Bay Bridge' in Scotland (1879), the 'Tacoma Bridge' near Seattle (1948), the cooling towers in Ferrybridge (England, 1965), 'Transvaal-Park' in Moscow (2004) and recent disasters in the Gulf of Mexico highlighted the need for a better understanding in this field.

Multidisciplinary problems involving fluid structure interaction are common in engineering design. Fluid flow and adjacent structures often interact through displacement and/or thermal effects. Such interactions may be a desirable part of a design or may cause unwanted behaviors that need to be considered and eliminated during the design process. Therefore, the ability to predict and counter-act potentially negative effects of fluid-structures interactions is very important and challenging for most of the engineering field.

1.3 Previous Research

Considering the importance of fluid structure interaction, an extensive research work has been carried out by naval architects, offshore and ocean engineers, hydrodynamists and mathematicians. Both experimental and numerical investigations have been carried out to examine the characteristic of both laminar and turbulent flow around different structures, e.g., circular cylinder, pod, strut, hydrofoil, sphere, surface ship, under-water vessel, propeller etc.

The laminar and turbulent unsteady viscous flow behind a circular cylinder has been the subject of numerous experimental and numerical studies, especially from the hydrodynamics point of view. According to the observation of Sumer (1997); the

flow field over the circular cylinder is symmetric at low values of Reynolds number. As the Reynolds number increases, flow begins to separate behind the cylinder causing vortex shedding which is an unsteady phenomenon. For the $40 < Re < 200$ there is a laminar vortex shedding in the wake of the cylinder. The laminar wake transient to turbulence in the region of $Re = 200$ to 300 . In the subcritical region $300 < Re < 3 \times 10^5$ the wake behind the circular cylinder becomes completely turbulent and a laminar boundary layer separation occurs. The unsteady flow was first studied by Payne (1958) for Reynolds number equal to 40 & 100. The numerical study and physical analysis of the pressure and velocity fields in the near wake of a circular cylinder for laminar and turbulent flow has been investigated by Braza *et al.* (1986) and Braza *et al.* 1990. Recently Lakshminpathy (2004), Reichl *et al.* (2005) and Rahman *et al.* (2007) have also investigated this problem for different Reynolds numbers. The common points of interest of these works are the development of the primary unsteady wake behind the circular cylinder and the evaluation of the drag coefficient and the separation angle with time. Most of the experimental studies investigated the steady and unsteady behaviors of the alternating vortices in the wake. The experimental investigation of Tritton (1959) and Anderson (2005) should be mentioned.

A considerable amount of research work has been published on flow around the axisymmetric body of revolution such as: sphere, pod, submarine, axisymmetric under-water body etc. The basic structure of the flow past a sphere has been experimentally investigated using a variety of approaches, including flow visualization by Achenbach (1972), Taneda (1978), Kim (1988), Sakamoto (1990), Bakic (2002) etc. Recent time-accurate computations of laminar and turbulent flow around spheres using different methods are reported by many researchers, among them the work of Chomaz (1993), Amone (1995), Kalro (1998), and Sun *et al* (2006) are remarkable.

Multi-component propulsors are becoming increasingly popular in modern commercial marine vessels on account of the increase of their efficiency due to the cancellation of the flow swirl downstream of the propeller. The major advantage of using a podded propulsor is that the inflow to the propeller is more uniform compared to that of a conventional propulsion system. The study of flow around the

propeller and the pod and strut unit is of increasing importance due to the extensive use of podded propulsors.

An optimum design can be chosen to minimize the drag and flow separation by Varidal *et al* (1999), and can lead to better efficiency of the podded propulsor. The flow around pod was investigated and the force acting on it was calculated by a large number of researchers. Among them the work of Stern (1994), Choi (2000), Choi (2003), Gupta (2004), Kimas (2004) and Mishra (2005) are very much related with the present work. Priyono (1994) and Fan (1995) also investigate the pressure and viscous drag on the axisymmetric body

Applications of computational fluid dynamics (CFD) to the maritime industry continue to grow as this advanced technology takes advantage of the increasing speed of computers. Numerical approaches have evolved to a level of accuracy which allows them to be used during the design process to predict ship resistance. Simulation of flows past underwater vehicle hull forms is of considerable importance in marine hydrodynamics. This is mainly due to lack of reliable and sufficiently accurate experimental data. Generation of quality experimental data requires a large number of hull forms and experimental facilities. In the last two decades, different areas of incompressible flow modeling - including grid generation techniques, solution algorithms and turbulence modeling, and computer hardware capabilities - have witnessed tremendous development. In view of these developments, computational fluid dynamics (CFD) can offer a cost-effective solution to many problems in underwater vehicle hull forms. However, effective utilization of CFD for marine hydrodynamics depends on proper selection of turbulence model, grid generation and boundary resolution. On the other hand grid generation and boundary layer resolution depends on the kind of turbulence model that is used in a solution process. However, it can be said that the main issue is turbulence modeling and grid generation and boundary layer resolution are sub-issues.

Many researchers used turbulence modeling to simulate flow around axisymmetric bodies since late seventies. The flow around under water ship or submarine was investigated and the force acting on it was calculated by a large number of researchers. The present research is influenced by the work of Gertler (1950), White

(1977), White (1978), Lin *et al.* (1995), Schwabacher (2000), Sohaib (2003), Joubert (2006) etc

1.4 Research Objectives

The main objective of the present study is to apply Finite Volume Method for the hydrodynamic analysis of fluid structure interaction (FSI). The investigation is carried out to simulate incompressible flow around some marine structures (e.g., circular cylinder, sphere, pod and submarine) and investigate the viscous drag and flow pattern for different Reynolds numbers. The specific aims of this study are:

- to apply finite volume method to analyze the flow around marine structures
- to divide the flow domain with different types of grid and check the grid independency on the predicted results.
- to visualize the flow in wake for laminar and turbulent flow
- to compute the viscous drag acting on the body for different Reynolds numbers
- to validate predicted results comparing with experimental and other numerical results.

CHAPTER 2

2. COMPUTATIONAL FLUID DYNAMICS MODELING CONSIDERATIONS

2.1 Discretization Methods in Computational Fluid Dynamics

Every computational fluid dynamics, in one form or another, is based on the governing equations of fluid dynamics: the continuity, energy, and momentum equations. These equations mathematically state three things, respectively: that mass is conserved, that energy is conserved, and that force equals mass times acceleration. In general, these governing equations can be written in two forms: the integral form and the partial differential equation, or PDE form. Though the form of the equations results little difference with regard to hydrodynamic theory, different form leads to vastly different CFD solution algorithm. Since computers are unable to directly solve the governing equations of fluid motion, these equations must be transformed into forms that computers can handle; namely, the partial derivative (or integral) equations must be replaced with discrete numbers. In short, the computational domain is discretized so that the dependent variables are computed only at discrete points. Derivatives and integrals are approximated, which lead to an algebraic representation of the governing equations. In this way, a calculus problem is effectively transformed into an algebraic problem. There are three discretization schemes in CFD: (i) Finite Difference Method (FDM) (ii) Finite Element Method (FEM) (iii) Finite Volume Method (FVM) which are discussed elaborately by Versteeg & Malalasekera, (1995).

2.1.1 Finite Difference Method (FDM)

The FDM is the oldest of the methods, considered to have been developed by Euler in 1768, and is used to obtain numerical solution to differential equations by simple calculations. Taylor's series expansions are used to generate finite difference approximations to the derivatives of the RANS equations. The derivatives appearing in the governing equations are then replaced by these finite difference expressions.

yielding an algebraic equation for the flow solution at each grid point. It is the simplest method to apply, but requires a high degree of regularity of the mesh.

2.1.2 Finite Element Method (FEM)

The FEM was developed initially as a procedure for constructing matrix solutions to stress and displacement calculations in structural analysis. The method uses simple piecewise polynomial functions on elements to describe the variations of the unknown flow variables. When these approximation functions are substituted into the governing equations it will not hold exactly, and the concept of a residual is introduced to measure the errors. These residuals are then minimized by multiplying by a set of weighting functions and then integrating. This result is a set of algebraic equations for the unknown terms of the approximating functions and hence the flow solutions can be found. Finite element method is not used extensively as it requires greater computational resources and CPU effort than equivalent finite volume method.

2.1.3 Finite Volume Method (FVM)

The FVM method discretises the integral form of the governing equations directly in physical space. The resulting statements express the exact conservation of relevant properties for each finite cell volume. Finite-difference type approximations are then substituted for the terms of the integrated equations, forming algebraic equations that are solved by an iterative method which will be discussed in Chapter 3. As this method works with the cell volumes and not the grid intersection points, both structured and unstructured meshes can be used. Flow variables can be stored either at Cell Centre or Cell Vertex locations. Conveniently, the cells coincide with the control volumes if using the Cell Centered scheme. For the Cell Vertex scheme, additional volumes are required to be constructed; however, the scheme has the advantage that boundary conditions are more easily applied since the variables are known on all boundaries.

2.2 Basics of Fluid Dynamics

In order to understand the results of this study, one must first understand the basics of fluid flow concepts including viscosity (μ), density (ρ), turbulent and laminar flow and Reynolds number. Firstly, all fluids, whether they are liquids or gasses, have a certain density and viscosity. While the definition of density is widely understood as the

weight of set volume of material, the definition of viscosity is much less widely known. Viscosity is a measure of a fluids resistance to flow. When a fluid is sheared (a force is applied), it begins to strain at a rate inversely proportional to the viscosity (Versteeg & Malalasekera, 1995). Accordingly, a high viscosity translates to a slower moving fluid. Together with the geometry and velocity of the flow situation a value known as the Reynolds number can be assigned. Reynolds number is represented by the expression:

$$Re = \frac{\rho UL}{\mu} \quad (2.1)$$

Where, U is the free stream flow velocity and L is the length value suited for the situation, typically the length of a surface or the diameter of a pipe. Reynolds number is a dimensionless value describing the viscous behavior of all Newtonian fluids. Because density (ρ), viscosity (μ) and L remain constant throughout the experiment, the Reynolds number is directly proportional to the free-stream velocity.

2.3 Laminar and Turbulent Flow

In general, viscous flow over a surface can be characterized in two ways. If the path lines of the various fluid elements that make up the flow move smoothly and evenly, as shown in Figure 2.1 (a), the flow is called laminar. Conversely, if the movement of the fluid elements is rough and erratic, as shown in Figure 2.1 (b), the flow is called turbulent. Reynolds number is also necessary for discussing the difference between laminar and turbulent flow. Laminar flow is orderly in nature and follows smooth streamlines. Turbulence is a random phenomenon of flow disorder paradoxically due to the destabilizing effects of viscosity (Versteeg & Malalasekera, 1995).

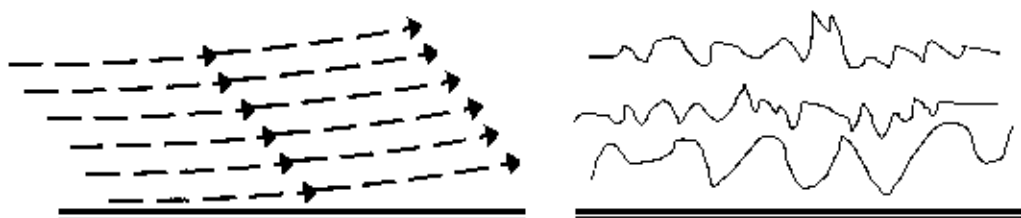


Figure 2.1: (a) Laminar and (b) Turbulent Path Line

Reynolds number is used as a measure of when or where turbulent flow will occur. In open flow, such as flow over a flat plate, turbulence transition occurs at Reynolds number of 5×10^5 based on plate length whereas in case of flow over cylinder it is 200 to 300 (Sumer, 1997). The laminar to turbulence transition point in either flow situation is based on the disturbance from the leading edge of the plate by the boundary layer growth. It is not possible to predict exactly when the transition from laminar to turbulent flow will occur since factors such as free stream mixing and environmental noise levels influence the transition. Realistically, most engineering problems are in the turbulent domain. Understanding the difference between these two types of flow is critical in analyzing a fluid dynamics problem, since much different answers can be determined based on the flow condition. The characterization of the flow field is particularly important in this study because laminar and turbulent flow fields contribute very differently to the total drag on a given body.

2.4 Drag Forces

Flow past an immersed body causes forces to be applied to that body, which are dependent on its shape and the nature of the flow. When fluid flows over a circular cylinder then generally the cylinder is considered stationary. On the other hand, with regard to pod/submarine, the body moves through the fluid, while the fluid is more or less stationary. However, analyzing flow patterns past a moving body with stationary fluid is dynamically equivalent to analyzing the flow pattern around a stationary body as the flow moves. For ease of CFD simulation the later frame of reference is employed to determine the forces. In order to compare data between experimental tests run using different speeds or even fluids one can make use of dynamic similarity. With drag values this common ground is found using a dimensionless coefficient C_D , which is determined using Equation (2.2):

$$C_D = \frac{DRAG}{\frac{1}{2} \rho U^2 A} \quad (2.2)$$

As shown, the drag force is made non-dimensional by dividing by the dynamic pressure

and the area. The particular area used depends on the shape involved. As a general rule, the frontal area is used for bluff bodies (e.g. cylinder, sphere) and the wetted area is used for stream line bodies (e.g. pod, submarine). The drag value in the above equation is the drag force on the body, which is caused by both viscous (frictional) and pressure (form) effects.

2.4.1 Viscous drag

The viscous effects are a result of the friction between the fluid and the body and are generated in the boundary layer. Fluid near the body is in a no slip condition, meaning the flow directly next to the body wall is at zero velocity relative to the velocity of the wall. This causes shear stresses to be introduced to the flow. Turbulence kinetic energy builds up as the flow passes over the body creating swirling vortices that eventually dissipate into heat energy. This viscous effect accounts for nearly all of the drag on a flat plate can be found using the Equation (2.3). Much more detail is available from other resources (Versteeg & Malalasekera, 1995)

$$D_v(x) = \int \tau_w DA \quad (2.3)$$

For this equation D_v is the drag force, τ_w is the wall shear and the integral is over the surface. Blasius (1908) was also able to determine the skin friction coefficient of the flat plate, which relates to viscous drag. Equations are as follow:

$$c_f = \frac{0.664}{Re_x^{1/2}} \quad \text{Laminar} \quad (2.4)$$

$$c_f = \frac{0.027}{Re_x^{1/4}} \quad \text{Turbulent} \quad (2.5)$$

C_f is the skin friction coefficient and is a measure of the wall shear on the flat plate. It can be used to determine if CFD results are at least in the right range for its final results. Based on flat plate calculations, the viscous drag coefficient is equal to twice the skin friction coefficient over the surface. Again, this is only an approximation since an ideal flat plate is rare in practical applications.

2.4.2 Pressure drag and flow separation

Determining the boundary layer thickness from flat plate theory can only act as an approximation since flat plate boundary layer development is not affected by pressure gradients. In most practical cases there will be pressure gradients that very much affect the boundary layer thickness. Negative pressure changes or where pressure is decreasing and velocity is increasing, are known as favorable pressure gradients and lead to a thinner boundary layer. Positive pressure changes or where pressure is increasing and velocity is decreasing, are known as adverse pressure gradients (Versteeg & Malalasekera, 1995) and lead to a thicker boundary layer.

Flow separation describes the phenomenon of boundary layer separating from the body and often recirculating back towards the flow. Flow separation cannot occur under favorable pressure gradient, it occurs only under an adverse pressure gradient. For the case of a pod or a submarine hull facing directly into the flow, there is a favorable pressure gradient at the front of the hull, near zero pressure gradient along the body of the hull and an adverse pressure gradient along the rear of the hull. Naturally, there is a potential for the flow to separate at the rear of the hull. If the adverse pressure gradient is too high the fluid near the wall will stall and separation will occur. A very interesting and useful point to note about separation is that at the separation point the wall shear equals zero, and hence there is no viscous drag contribution. A zero wall shear condition can be looked for to determine if flow separation has occurred.

Pressure effects are dependent on the perturbation that a body makes on the flow. As fluid moves around an object, there exists a pressure difference between the front and the rear of that object. At the front of the pod/submarine hull exists a stagnation point, where high pressure is the result of a near stop in fluid flow. Surrounding the stagnation point there is a favorable pressure gradient with higher velocities. At the rear there is an adverse pressure gradient with low velocity and the possibility of separation. The effects of pressure differences appear in the general equation for pressure drag as given by,

$$D_p = \int_s p dA \quad (2.6)$$

The effects of boundary layer displacement, separation and viscous losses contribute to a pressure difference between the front and the rear of an object. It is the pressure difference over the area of the shape that makes up the pressure drag. Streamlined objects have relatively little pressure difference between the front and the rear and hence the viscous drag is dominant. Bluff bodies induce flow separation at the rear, which increases the pressure difference, thus making the pressure drag dominant.

2.5 Grid Generation

Analytical solutions of fluid dynamics problems involve closed-form mathematical expressions that describe the variation of the dependent variables continuously throughout the flow domain. However, numerical solvers cannot generate closed-form analytical expressions, but it can calculate values of the dependent variables only at discrete points in the domain. These points are called grid points, or nodes. In order for a computational fluid dynamics code to provide a complete flow field description for a particular problem, the user must specify a grid that tells the flow solver at what locations in the problem domain the solution is to be computed. The specifications of the grid construction can have a major influence on the fidelity of the solution and can, in fact, determine whether a solution is even attainable.

2.5.1 Solution dependence on grid

The quality and efficiency of the numerical solution is highly dependent on the construction of the grid used in the computational model. Several factors must be considered when generating a grid to ensure that the best possible numerical results are obtained with a particular solution algorithm. Grid point placement can have a substantial effect on the stability and convergence of the numerical solver. For example, if grid points are not adequately concentrated in regions of high flow parameter gradients (such as near shock waves, in boundary layer separation regions, or near stagnation points), the numerical solver may not be able to adequately resolve these gradients in the flow field. Because obtaining the solution numerically is an iterative process, it is possible, and quite likely, that an insufficiently fine mesh will preclude the adequate calculation of important flow features, leading to oscillations in computed parameters or even divergence of the solution.

In numerical grid construction, there is an important trade-off between mesh density, solution efficiency, and solution accuracy. Generally, the more grid points contained in a given grid, the more accurate the final, converged solution will be. However, the density of the grid cannot be arbitrarily increased without bound. Computer processor speed and memory limitations often dictate how fine a mesh can realistically be. Increasing the density of a mesh too much can quickly cause a given problem to become intractable. Along these same lines, it is important for the CFD analyst to carefully concentrate grid points in high-gradient regions while keeping the grid density throughout the majority of the computational domain fine enough for accuracy yet sparse enough for speed. Clearly, the maximum allowable grid point density of a particular simulation is highly dependent on the speed and capabilities of the computer platform being used.

In the case of unstructured grids, solution accuracy, convergence, and efficiency are also highly dependent on the shape of the elements used to form the mesh. Two primary element shapes are used when generating unstructured grids: triangles and quadrilaterals. Due to fewer constraints on their use, grids constructed of triangular elements are often easier to build around complex geometries than are quadrilateral grids, especially when using an automatic grid generation program like GAMBIT. Element skewness also tends to be less of a factor with triangular element grids. Since the relative skewness of elements has a direct influence on the robustness of the numerical model, particularly in high-gradient regions, triangular element-based grids hold an advantage in this regard. However, the price one pays when using triangular elements is in efficiency. Since for a given node distribution there is a higher concentration of triangular elements than there would be of quadrilateral elements, the use of triangular elements incurs a large speed penalty on the numerical solver. Analysts must also take into account the size of the computational domain when modeling a CFD problem.

2.5.2 Structured grids

There are two types of grids commonly used in CFD research today – structured grids and unstructured grids. Naturally, each type has its own advantages and disadvantages, and these factors must be carefully weighed to determine which type of grid is best suited to a particular problem. Frequently, the computational domain of a given

problem is selected to be rectangular in shape and its interior grid points are distributed at regularly-spaced intervals along grid lines. Since the grid points can be identified easily with their respective grid lines, such a grid is called a structured grid. Structured grids require a transformation from the physical space to the computational space. On the other hand, another type of grid system can be constructed where the grid points cannot be directly associated with orderly, defined grid lines; though not random, the distribution of grid points cannot be predicted in a well-defined manner. This type of grid is called an unstructured grid (Hoffmann, 1998).

Within a rectangular physical domain, the generation of a computational grid with uniform spacing is a relatively simple task. Unfortunately, the majority of physical domains of interest are not strictly rectangular in shape. Trying to impose a rectangular computational grid on a non-rectangular physical domain will require interpolation for the implementation of boundary conditions. This is not desired, since the boundary conditions have a major impact on the quality of the numerical solution. Further, complications in discretization at the edges of the computational domain make this approach less than ideal. In order to overcome these difficulties, a transformation from physical space to computational space is introduced that will map a non-rectangular coordinate system in the physical space to a rectangular system in the computational space. To eliminate the discretization difficulties associated with non-equal step sizes in the computational domain, particularly for the finite-difference approach, physical domains are generally transformed into rectangular, constant step-size, computational domains. Also, it can be seen that deformation of the physical domain is usually necessary to obtain the computational domain.

To determine the mapping of grid points in physical space to computational space, a few limitations are necessary. First, the mapping must be one-to-one; grid lines cannot cross one another. Second, a smooth grid point distribution, minimum grid line skewness, near-orthogonality, and concentration of grid points in regions of interest (i.e. high flow gradients or large dependent variable fluctuations) are all desired. There are three primary structured grid generation techniques prevalent today: algebraic methods, partial differential methods, and conformal mappings based on complex variables. Each of these techniques involves solving a system of equations: given fixed step sizes in the computational domain, the solution of these equations provides the

coordinates of the grid points in the physical domain. Modifying certain parameters within these equations allows the analyst to tailor the grid (to some degree) to provide higher grid resolution in physical areas of interest (boundary layers, separation regions, etc). Finally, the grid system may be either fixed or adaptive. A fixed system is generated prior to the solution of the governing equations and does not change as a result of the solution, where an adaptive grid system morphs as a result of the solution (for example, grid points may become concentrated in regions of high gradients, such as in the neighborhood of a shock wave).

2.5.3 Unstructured grids

It is interesting to note that discretization of a domain can be accomplished either directly in the physical space or in the transformed computational space; the choice depends mainly on the numerical solution method and the domain of the solution. For those solution schemes where the governing fluid dynamics equations are integrated numerically on the physical domain and solved, the corresponding grid system is usually generated directly in the physical domain. In such cases, the domain of solution is divided into individual cells (usually triangles or quadrilaterals in 2D or pyramids or tetrahedrons in 3D) and for these cases, the grid points generally cannot be associated with grid lines. Instead, locations of points must be individually specified. This type of grid system is known as an unstructured grid. In this study the unstructured grid is used only in case of sphere model.

Besides being a natural choice for use with finite volume numerical solvers, there are also a number of advantages that unstructured grids enjoy over structured grids. The main advantage of an unstructured grid is that it can be used with equal ease and success over a wide variety of surface geometries. Unstructured grids can also be used for both irregular, singly-connected domains as well as multiply-connected domains. Since unstructured grids do not rely on a mathematical transformation, or mapping, from physical space to computational space, they lend themselves more readily to node placement optimization. In other words, it is much easier to arbitrarily concentrate points in regions in the domain of high interest; for example, near large pressure gradients, inside boundary layers, or around shocks. By the same token, unstructured grids are also more easily coupled with grid refinement techniques for automated grid adaptation. However, unstructured grids have their drawbacks as well. Since the

position of each node is not determined by the solution to a set of equations, but instead, is defined explicitly, there is a substantial amount of book-keeping associated with defining the position of every node in the unstructured mesh. This added data manifests itself in increased program complexity and reduced computational efficiency of CFD solutions of problems using unstructured grids compared to structured grids.

2.6 Two-Dimensional Versus Three-Dimensional Modeling

Since most physical flows are three-dimensional, it seems logical that a three-dimensional model would be the ideal choice for solving most real-world problems. However, in those real flows where the salient features are primarily two-dimensional or axisymmetric in nature (for example, flow over a high aspect ratio wing or flow around a sphere/pod/submarine respectively), two-dimensional computational models often provide a sufficiently accurate description of the major flow features to render the inclusion of the third dimension unnecessary. In fact, the additional computational load incurred by modeling and solving a full three-dimensional flow field can be substantial; increases in solution time on the order of ten or more are common. Two-dimensional solutions are, of course, unable to resolve complex three-dimensional flow features (like 3D vortex interactions), but in those cases where the physical geometry warrants it, 2D models are often preferred for the significant efficiency advantages they provide. In addition, the sophistication of grids required for two-dimensional problems is greatly reduced compared to those required for full three-dimensional simulations. This has advantages both for the analyst and the grid generation software – the analyst can design a 2D computational mesh much more quickly than a 3D mesh, and the grid generation software (in this case, GAMBIT), can compute the associated node distribution for a given mesh boundary spacing much more efficiently and with a greater degree of success for a 2D case than for a 3D case. Since GAMBIT has been shown to have difficulty generating quadrilateral element-based meshes for 2D geometries, adding a third dimension would provide even more complexity and increase the likelihood of unstructured mesh generation problems.

2.7 Steady-State versus Time-Varying Solution Techniques

The last major consideration to be made when solving a particular CFD problem is to decide whether to model the problem using a steady-state technique or a time-varying

technique. Since all real-world problems take place over time, it seems natural to model problems as time-varying. However, there are several compelling reasons against this approach. First, if the flow parameters do not vary with time then a steady-state technique is the obvious choice. Second, even if time-varying elements are present in the real flow, there may be good reason to model the flow using a steady-state approach, in which case the analyst must determine how important the time-varying elements of the flow are to the overall behavior of the system. For one, in a time-varying approach, the governing fluid dynamics equations must be discretized in space and time. Not only does this complicate the set of algebraic equations the numerical solver must manipulate, but sub-iterations become necessary to compute a flow field solution for each instant of time. In other words, the solver must achieve a converged solution for each increment of time that the analyst has chosen to model. This can increase the total rate of convergence by several orders of magnitude and reduce the computational efficiency of the model to the point where the problem is no longer tractable. Also, since convergence of each sub-iteration must be attained prior to proceeding on to the next time step, the likelihood of solution oscillations or divergence is increased.

The major drawback in modeling a problem as steady-state is that the possibility exists those important aspects of the flow will be overlooked. For example, time-varying and periodic behaviors such as vortex mixing and vortex streets, and transient behaviors such as flow acceleration and deceleration will not be captured when using a steady-state approach. Again, intuition on the part of the fluid dynamics is necessary to determine whether the omission of such aspects of the flow will have a large impact on the overall accuracy of the solution generated by the flow solver.

CHAPTER 3

3. THEORETICAL BACKGROUND

3.1 Governing Equations

The conservative or divergence form of the system of equations which governs the time dependent two dimensional flow of an incompressible Newtonian fluid is [Versteeg and Malalasekera, 1995].

$$\text{Mass/continuity : } \text{div}(\vec{u}) = 0 \quad (3.1)$$

$$\text{x-momentum : } \rho \left[\frac{\partial u}{\partial t} + \text{div}(\vec{u} u) \right] = -\frac{\partial p}{\partial x} + \text{div}(\mu \text{ grad } u) + S_x \quad (3.2)$$

$$\text{y-momentum : } \rho \left[\frac{\partial v}{\partial t} + \text{div}(\vec{v} u) \right] = -\frac{\partial p}{\partial y} + \text{div}(\mu \text{ grad } v) + S_y \quad (3.3)$$

Where, ρ = density, p = pressure, t = time, $\vec{u} = ui + vj$ = velocity vector, μ = viscosity, and S = source term. The above equations are known as conservation equations as these equations obey the conservation principles of mass, momentum and energy. It is clear that there are significant commonalities among above the various equations. So these equations can be written in a general form and that general equation can be solved numerically instead of solving each equation individually. By introducing a general variable ϕ the conservative form of all fluid flow equations can be written as:

$$\rho \left[\frac{\partial \phi}{\partial t} + \text{div}(\vec{\phi} u) \right] = \text{div}(\Gamma \text{ grad } \phi) + S_\phi \quad (3.4)$$

In words

Rate of increase of ϕ of fluid element (Unsteady term)	+	Net rate of flow of ϕ out of fluid element (Convective term)	=	Rate of increase of ϕ due to diffusion (Diffusive term)	+	Rate of increase of ϕ due to source (Source term)
--	---	--	---	---	---	---

Equation (3.4) is the so-called transport equation for property ϕ . In order to bring out the common features we have, of course, had to hide the terms that are not shared between the equations in the source terms. By setting ϕ equal to 1, u , v and selecting appropriate values for the diffusive coefficient Γ and source term we may obtain Equations (3.1) to (3.3). Equation (3.4) is used as the starting point for computational procedures in the finite volume method.

3.2 Solution using Finite Volume Method

As we have seen, all differential equations are conservation equations for mass, momentum, energy so it is necessary that all discretized equations also obey the conservation principle. Finite volume method is inherently conservative method because the flux going out through a face of one control-volume is exactly equal to the flux coming into the adjacent control-volume through the same face. Including discretization following steps are involved in finite volume method.

- i. Divide the domain into finite control volumes.
- ii. Integrate the differential equations over each control volume.
- iii. Approximation of volume and surface integrals.
- iv. Discretization and interpolation using UDS or CDS.

3.2.1 Control volume faces location

Before going to discretization scheme it is important to define the gridding with sign convention used in this method. A portion of the 2-dimensional Cartesian grid with general notation in finite volume method is shown in Figure 3.1. In the finite volume method, to calculate all fluxes through the control volume, location of its faces is important since control-volume faces define physically a control volume.

Discretization is done in general terms so that it can be applicable to each control-volume. There are two ways to locate faces of control-volume with respect to grid points.

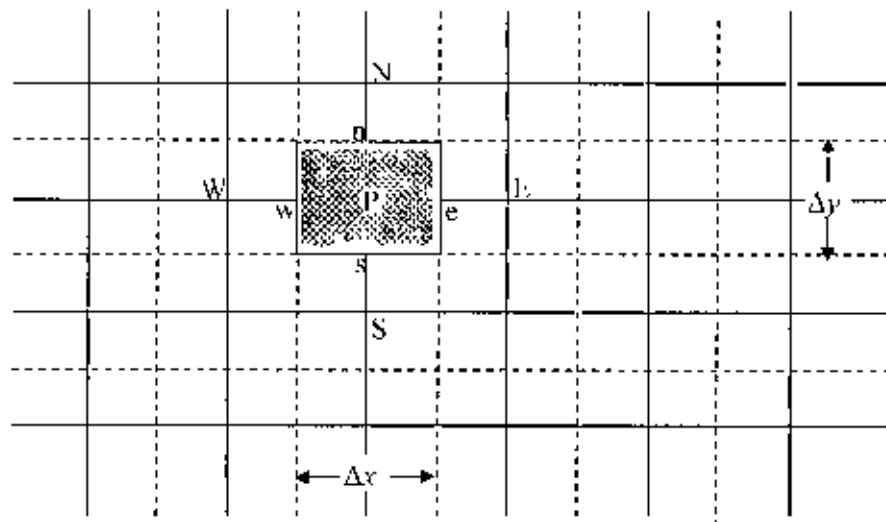


Figure 3.1. 2-D Cartesian Grid with General Notation in Finite Volume Method

1. Faces of control-volumes (CV) located midway between the grid points.
2. Grid points are placed at centers of control volume.

In the first case, grid points are constructed first and then CV faces are placed midway between these grid points. In this case, the grid points do not lie on geometric centers of the control-volumes. Special care should be taken while dealing with boundary control volumes. At boundary, this practice leads to a set of half control-volumes and therefore discretization scheme for boundaries have to be changed.

In the second case, control-volume boundaries are drawn first and then grid points are placed at the centre of each control-volume. In case of uniform grid both schemes are identical.

The first scheme is more accurate than the second one in calculating diffusive flux because the slope of line (for linear profile of variable) is nearly the same as that of slope of tangent to the parabola (parabolic profile) evaluated midway between the grid points. Second scheme is more convenient than the first one because it covers the whole domain with small finite control-volumes. The control-volume centers lie on the geometric centre of the control-volume and therefore midpoint approximation which is done during discretization in next section will be more accurate.

3.2.2 Integration of the Transport Equation

The key step of finite volume method is the integration of the transport Equation (3.4) over each control volume yielding

$$\rho \left[\int_{V'} \frac{\partial \phi}{\partial t} dv + \int_{V'} \text{div}(\phi \vec{u}) dv \right] = \int_{C'} \text{div}(\Gamma \text{grad } \phi) dv + \int_{V'} S_{\phi} dv \quad (3.5)$$

The volume integrals in the second term on the left hand side, the convective term, and in the first term on the right hand side, the diffusive term, are re-written as integrals over the entire bounding surface of the control volume by using Gauss' divergence theorem

For a vector \vec{a} this theorem states

$$\int_V \text{div } \vec{a} dv = \int_A \vec{n} \cdot \vec{a} dA$$

Where \vec{n} is the vector normal to surface element dA .

Applying Gauss' divergence theorem, Equation (3.5) can be written as

$$\rho \left[\frac{\partial}{\partial t} \left(\int_{V'} \phi dv \right) + \int_A \vec{n} \cdot (\phi \vec{u}) dA \right] = \int_A \vec{n} \cdot (\Gamma \text{grad } \phi) dA + \int_{V'} S_{\phi} dv \quad (3.6)$$

In steady state problems, first term of Equation (3.6) is equal to zero. This leads to the integrated form of the steady transport equation

$$\rho \int_A \vec{n} \cdot (\phi \vec{u}) dA = \int_A \vec{n} \cdot (\Gamma \text{grad } \phi) dA + \int_{V'} S_{\phi} dv \quad (3.7)$$

Here we are solving this problem in two dimensions that is, in x-y plane, so it can be written as

$$\begin{aligned} \rho \left[\int_u (u\phi) dx - \int_u (u\phi) dx + \int_v (v\phi) dx - \int_v (v\phi) dx \right] = \\ \int_v \left(\Gamma \frac{\partial \phi}{\partial x} \right) dy - \int_u \left(\Gamma \frac{\partial \phi}{\partial x} \right) dy + \int_v \left(\Gamma \frac{\partial \phi}{\partial y} \right) dx - \int_u \left(\Gamma \frac{\partial \phi}{\partial y} \right) dx + \int_{V'} S_{\phi} dx dy \end{aligned} \quad (3.8)$$

Here, the term $\rho \vec{u} \phi$ is the convective flux and $\Gamma \text{grad } \phi$ is the diffusive flux.

3.2.3 Approximation of integrals

The next step is to approximate the flux integrals which are done by two levels of approximation. Consider, f_i = the flux in the i^{th} direction. In first level the integral is approximated in terms of the variable values at one or more location on the cell face. The simplest way is the midpoint rule flux, where the f_i is approximated as the value at the centre of CV face. The midpoint rule is a second order approximation, so in order to preserve the second order accuracy the interpolation should also be of second order. On the east face of control-volume, the midpoint rule applied as:

$$\int_{\text{face}} f_i dy = f_e \Delta y$$

Source term approximation is done by applying the centre value of the source as representative value for the whole CV. Thus, Equation (3.8) becomes

$$\begin{aligned} & \rho [(u\varphi)_e \Delta y - (u\varphi)_w \Delta y + (v\varphi)_e \Delta x - (v\varphi)_w \Delta x] = \\ & \left(\Gamma \frac{\partial \varphi}{\partial x} \right)_e \Delta y - \left(\Gamma \frac{\partial \varphi}{\partial x} \right)_w \Delta y + \left(\Gamma \frac{\partial \varphi}{\partial y} \right)_e \Delta x - \left(\Gamma \frac{\partial \varphi}{\partial y} \right)_w \Delta x + \bar{S} \Delta x \Delta y \end{aligned} \quad (3.9)$$

This can also be written

$$\begin{aligned} & \rho [u_e \varphi_e \Delta y - u_w \varphi_w \Delta y + v_e \varphi_e \Delta x - v_w \varphi_w \Delta x] = \\ & \Gamma_e \left(\frac{\partial \varphi}{\partial x} \right)_e \Delta y - \Gamma_w \left(\frac{\partial \varphi}{\partial x} \right)_w \Delta y + \Gamma_n \left(\frac{\partial \varphi}{\partial y} \right)_n \Delta x - \Gamma_s \left(\frac{\partial \varphi}{\partial y} \right)_s \Delta x + \bar{S} \Delta x \Delta y \end{aligned} \quad (3.10)$$

To simplify the above equation, the convective flux is denoted by F , that is.

$$F_i = \rho u_i \Delta x_i$$

Equation (3.10) now be simplified to

$$\begin{aligned} & F_e \varphi_e - F_w \varphi_w + F_n \varphi_n - F_s \varphi_s = \\ & \Gamma_e \left(\frac{\partial \varphi}{\partial x} \right)_e \Delta y - \Gamma_w \left(\frac{\partial \varphi}{\partial x} \right)_w \Delta y + \Gamma_n \left(\frac{\partial \varphi}{\partial y} \right)_n \Delta x - \Gamma_s \left(\frac{\partial \varphi}{\partial y} \right)_s \Delta x + \bar{S} \Delta x \Delta y \end{aligned} \quad (3.11)$$

3.2.4 Interpolation

After the approximation of the integrals we obtain Equation (3.11) involving the values of fluxes at each CV face, with ϕ as unknown. Since we want to calculate the variable at each grid point, it is required to write ϕ at face location in terms of their values at the grid points. Thus, we have to interpolate ϕ between grid points. There are many schemes available for approximation. Two basic schemes are the Central Differencing Scheme (CDS) or Linear Interpolation, and Upwind Differencing Scheme (UDS). Diffusive term is generally discretized using CDS approximation whereas convection term can be discretized by any scheme depending on the strength of the convection (Versteeg and Malalasekera, 1995).

In the present study, the convective term is discretized by upwind differencing scheme. In the upwind method the variation of ϕ between two grid points is approximated by a zeroth order polynomial, i.e., a constant value from the grid node in upstream direction, as for example for a flow in positive x direction we take ϕ_e is equal to the value of ϕ in upstream direction which is ϕ_p .

$$\phi_e = \begin{cases} \phi_p & \text{if } F_e > 0 \\ \phi_s & \text{if } F_e < 0 \end{cases} \quad \phi_n = \begin{cases} \phi_p & \text{if } F_n > 0 \\ \phi_w & \text{if } F_n < 0 \end{cases} \quad (3.12)$$

$$\phi_n = \begin{cases} \phi_s & \text{if } F_n > 0 \\ \phi_p & \text{if } F_n < 0 \end{cases} \quad \phi_e = \begin{cases} \phi_w & \text{if } F_e > 0 \\ \phi_p & \text{if } F_e < 0 \end{cases}$$

Flux approximation for F

$$F_e \phi_e = \max(F_e, 0) \phi_p + \min(F_e, 0) \phi_s$$

$$F_w \phi_w = \max(F_w, 0) \phi_s + \min(F_w, 0) \phi_p \quad (3.13)$$

$$F_n \phi_n = \max(F_n, 0) \phi_w + \min(F_n, 0) \phi_p$$

$$F_s \phi_s = \max(F_s, 0) \phi_w + \min(F_s, 0) \phi_p$$

Equations (3.12) and (3.13) are identical, both of them give the same information, but for generalization Equation (3.13) is used here. For implementation into the computer code, the expressions in Equation (3.13) are applied.

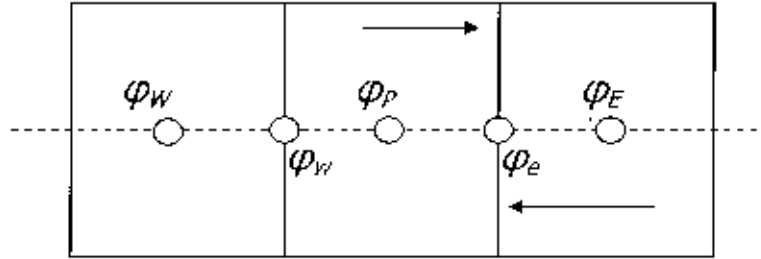


Figure 3.2: The Upwind Differencing scheme.

Like the convective flux, the diffusive flux integral is approximated by midpoint rule. The derivatives of ϕ are generally approximated by the CDS as follows:

$$\left(\frac{\partial \phi}{\partial x}\right)_i = \frac{\phi_i - \phi_P}{x_P - x_i} \quad \left(\frac{\partial \phi}{\partial x}\right)_n = \frac{\phi_i - \phi_W}{x_n - x_P} \quad (3.14)$$

$$\left(\frac{\partial \phi}{\partial x}\right)_n = \frac{\phi_P - \phi_P}{y_n - y_P} \quad \left(\frac{\partial \phi}{\partial x}\right)_i = \frac{\phi_P - \phi_P}{y_i - y_P}$$

3.2.5 Linear equation system

It may be possible that sometimes source term is a non-linear function of unknown ϕ to improve convergence it can be linearized as:

$$\bar{S} \Delta x \Delta y = S_0 + S_P \phi_P$$

Where, S_0 = constant term

S_P = is a function of ϕ .

Using the above schemes for the diffusive and convective fluxes and source term linearization the discretization Equation (3.11) can be rearranged to:

$$a_P \phi_P = a_i \phi_i + a_W \phi_W + a_n \phi_n + a_S \phi_S + b \quad (3.15)$$

$$\text{Where, } a_i = -\min(F_i, 0) + \frac{\Gamma_c \Delta y}{x_i - x_P}$$

$$a_{\delta} = \max(F_{\delta}, 0) + \frac{\Gamma_{\delta} \Delta y}{x_p - x_{\delta}} \quad (3.16)$$

$$a_{\delta} = -\min(F_{\delta}, 0) - \frac{\Gamma_{\delta} \Delta x}{y_w - y_p}$$

$$a_{\delta} = \max(F_{\delta}, 0) + \frac{\Gamma_{\delta} \Delta x}{y_l - y_p}$$

$$a_p = a_l + a_{\delta} + a_w + a_{\delta} - S_p$$

$$b = S_p$$

Equation (3.15) can be written in the general form,

$$a_p \phi_p = \sum a_{nb} \phi_{nb} + b \quad (3.17)$$

Here, 'nb' represents neighboring points.

Discretized equation of the form (3.17) must be set up at each of the nodal points in order to solve a problem. For control volumes that are adjacent to the domain boundaries the general discretized equation (3.17) is modified to incorporate boundary conditions. The resulting system of linear algebraic equations is then solved to obtain the distribution of the property at nodal points.

Equation (3.19) is a linear algebraic equation which can be solved by applying several algebraic solvers e.g. Gauss elimination, LU decomposition, TDMA using boundary conditions. Iterations should be done until a converged solution is achieved [Versteeg and Malalasekera, 1995].

3.2.6 Finite volume method for unsteady flow

The first term of Equation (3.6) represent the rate of change term which is considered zero for steady flows. To predict transient problem we must retain this term in the discretization process. The finite volume integration of transport equation over a control volume (CV) must be augmented with a further integration over a finite time step Δt . This yield the most general integrated form of transport equation:

$$\rho \left[\int_{CV} \frac{\partial}{\partial t} \left(\int_{CV} \phi dV \right) dt + \int_{CV} \int_A \vec{n} \cdot \left(\vec{\phi} \vec{u} \right) dA dt \right] = \int_{CV} \int_A \vec{n} \cdot (\Gamma \text{grad } \phi) dA dt + \int_{CV} \int_V S_\phi dV dt \quad (3.18)$$

That can be written as,

$$\rho \left[\int_{CV} \left(\int_1^{n+M} \frac{\partial \phi}{\partial t} dt \right) dV + \int_1^{n+M} \left(\int_A \vec{n} \cdot \left(\vec{u} \phi \right) dA dt \right) \right] = \int_1^{n+M} \left(\int_A \vec{n} \cdot (\Gamma \text{grad } \phi) dA \right) dt + \int_1^{n+M} \int_{CV} S_\phi dV dt \quad (3.19)$$

The discretization of convection, diffusion and source term are same as discussed in the previous sections. Here we focus our attention on methods necessary for time integration. The implicit method is used in this study for discretization of unsteady convection-diffusion equation [see Versteeg and Malalasekera, 1995 for detailed description]. The implicit method is recommended for general purpose CFD computations on the ground of its superior stability. The implicit discretization two-dimensional equation is

$$a_p \phi_p = a_e \phi_e + a_w \phi_w + a_n \phi_n + a_s \phi_s + a_p^0 \phi_p^0 + b \quad (3.20)$$

where $a_p = a_e + a_w + a_n + a_s + a_p^0 + \Delta F - S_p$

with $a_p^0 = \frac{\rho \Delta V}{\Delta t}$

the other coefficient are same as Equation (3.16)

3.2.7 Solution algorithm for pressure-velocity coupling

The solution procedure of the generalized transport equations discussed in Section 3.2 can be summarized as:

1. Define the geometry of the case
2. Split the region of flow into cells (CV)
3. Integrate the equations of interest over each cell (Discretization)

4. Invert the resulting matrix
5. Repeat for as many time steps as necessary

Navier-Stokes Equations [3.1 to 3.3] for two dimensional flow of incompressible fluid can be written in vector notation as:

$$\left. \begin{aligned} \nabla \cdot \vec{u} &= 0 & (I) \\ \frac{\partial u}{\partial t} + \nabla \cdot \left(u \vec{u} \right) &= -\frac{1}{\rho} \frac{\partial p}{\partial x} + \nu \nabla^2 u & (II) \\ \frac{\partial v}{\partial t} + \nabla \cdot \left(v \vec{u} \right) &= -\frac{1}{\rho} \frac{\partial p}{\partial y} + \nu \nabla^2 v & (III) \end{aligned} \right\} \quad (3.21)$$

Where, $\nu = \frac{\mu}{\rho}$

For momentum, ignore 1st equation and concentrate on the momentum equation(s) (II & III). These are transport equation form, with a source term i.e., $-\frac{1}{\rho} \frac{\partial p}{\partial x_i}$ and a diffusion term on the RHS. However there are two main problems:

- The equation is non-linear that needs to be known \vec{u} to evaluate the transport of (u, v) into the domain
- The source term involves p , which is one of the variables we want to solve for

Both of these problems relate to the tangled nature of the NSE. Of the four equations making up the NSE: (continuity and the three components of velocity) all components of velocity appears in all the equations, and the pressure appears in the three velocity equations. It is not possible to evaluate the velocity until to know the pressure, and vice-versa. In order to find both, one value should be guessed and solve for the other, then go back and correct the first. It might start by guessing the pressure, and use this to get a better estimate of the velocity and then correct the pressure, etc.

In CFD there are two basic algorithms for doing this:

- PISO - Pressure Implicit Splitting of Operators - for time dependent flows

- SIMPLE - Semi-Implicit Method for Pressure Linked Equations - used for steady state problems

It is noted that, from Equation (II) if p and the flux (\vec{u}), are known then u_j can be found. Also, Equations (II-III) and (I) can be combined to give an equation for p given the flux,

$$\nabla \cdot \left[\frac{1}{A} \nabla p \right] = (\text{flux term}) \text{ that has to satisfy the continuity Equation (I).}$$

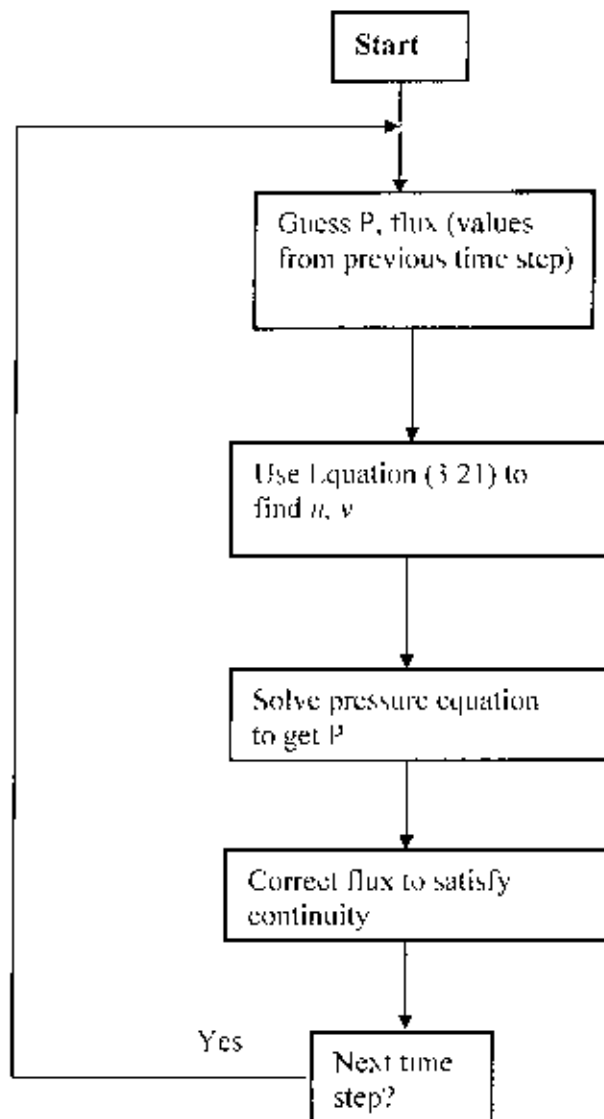


Figure 3.3: Flow Chart for PISO Algorithm

The PISO algorithm is as follows.

- Guess p , flux (use values from the previous time step)
- Use Equation (11) to find u , v etc.
- Solve the pressure equation for p
- Correct the flux to satisfy continuity

Steps 3 and 4 can be iterated if necessary, but this is usually not necessary. This advances the solution one time step - the whole procedure is then repeated from 1 to 4 for the next time step. The flow chart of PISO algorithm is given in Figure 3.2.

In this study PISO algorithm is used as velocity-pressure coupling for all unsteady simulations. As it is useful for unsteady flow and allow faster convergence than SIMPLER and is useful for irregular cells.

3.2.8 Implementation of boundary condition

The present section describes the implementation of boundary conditions in the discretized equations of the finite volume method. In constructing a staggered grid arrangement we set up additional nodes surrounding the physical boundary, as illustrated in Figure 3.4. The calculations are performed at internal nodes only ($I=2$ and $J=2$ onwards). Two notable features of the arrangement are (i) the physical boundaries coincide with the scalar control volume boundaries and (ii) the nodes just outside the inlet of the domain (along $I=1$ in Figure 3.4) are available to store the inlet conditions. This enables the introduction of boundary conditions to be achieved with small modifications to the discretized equations for near-boundary internal nodes.

The boundary conditions enter the discretized equations by suppression of the link to the boundary side and modification of the source terms. The appropriate coefficient of the discretized equation is set to zero and the boundary side flux – exact or linearly approximated – is introduced through source terms S_u and S_p . We shall frequently make use of this device to fix the flux of a variable at a cell face, but we also need a technique to cope with situation where we need to set the value of a variable at a node. This can be done by introducing two overwhelmingly large source terms into the relevant discretized

equation. For example to set the variable ϕ at node p to a value ϕ_{fix} the following source term modification is used in its discretized equation:

$$S_p = -10^{30} \text{ and } S_{nb} = 10^{30} \phi_{fix}$$

With these sources added to the discretized equation we have

$$(a_p + 10^{30})\phi_p = \sum a_{nb} \phi_{nb} + 10^{30} \phi_{fix}$$

The actual magnitude of the number 10^{30} is arbitrary as long as it is very large compared with the coefficients in the original discretized equation. Thus if a_p and a_{nb} are all negligible the discretized equation effectively states that

$$\phi_p = \phi_{fix}$$

Which fixes the value of ϕ at P .

Control volume at a boundary

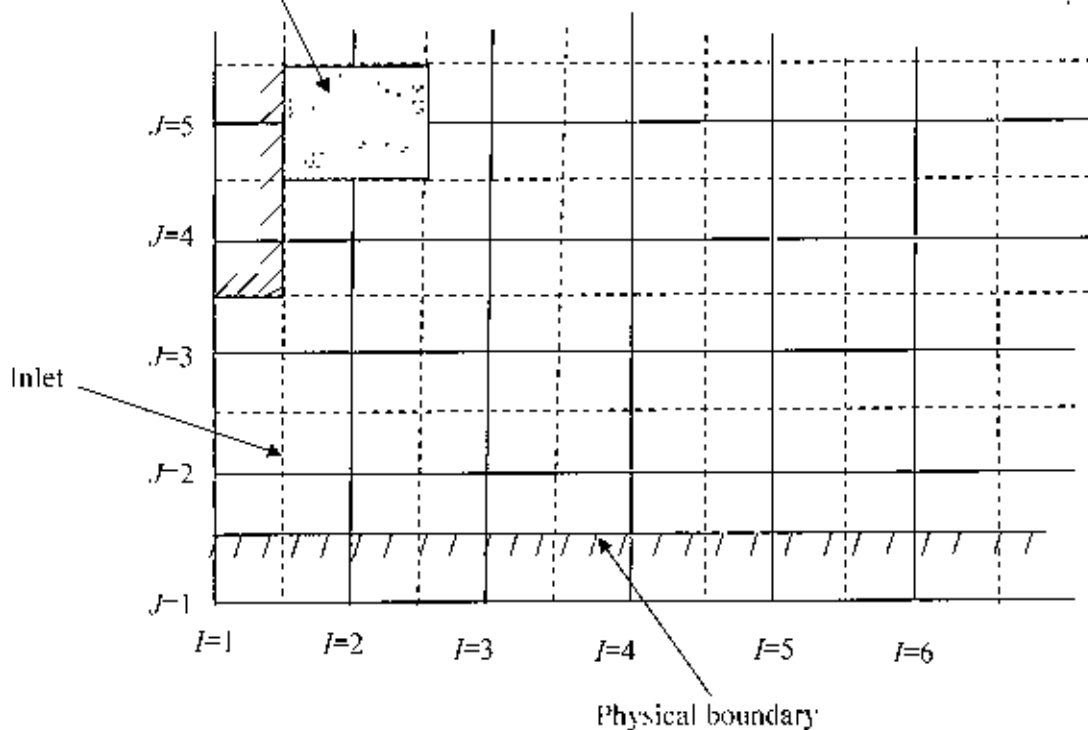


Figure 3.4 The Grid Arrangement at Boundaries of Finite Volume Method

In addition to set the value of a variable at internal nodes this treatment is also useful for dealing with solid obstacles within a domain by taking $\phi_{,jx} = 0$ (or any other desired value) at nodes within a solid region.

The system of discretized flow equations can be solved as normal without having to deal with the obstacles separately. Details of the modifications needed to implement the boundary conditions are explained by Versteeg and Malalasekera, 1995.

The boundary conditions applied in this study are:

- velocity inlet
- outflow
- wall
- periodic
- axis

Velocity inlet: The distribution of all flow variables needs to be specified at inlet boundaries. The velocity inlet boundary condition is intended for use with incompressible flows where the magnitude and direction of the inlet velocity is known. This boundary condition allows the stagnation, or total, properties of the flow to rise to whatever value is necessary to generate the prescribed velocity distribution. The velocities are set to a given value, and the first derivative of the pressure with respect to the axial direction is taken equal to zero.

$$(u, v) = (u, v)_{inlet} \quad \text{and} \quad \frac{\partial p}{\partial x} = 0$$

Outflow: The outflow boundary condition is used to model flow exits where the details of the flow velocity and pressure are not known prior to the solution of the problem. As long as the flow at the exit is expected to be well-developed and incompressible, application of the outflow boundary condition to the exit boundary is a reasonable choice. In this case, the derivatives of all the velocity components and the pressure with respect to the axial direction are taken equal to zero.

$$\frac{\partial(u, v, p)}{\partial x} = 0$$

Wall: the wall boundary condition is used to separate fluid and solid regions. In viscous flows (such as in this study), the no-slip ($u = v = 0$), or zero tangential velocity boundary condition, is enforced when the wall boundary condition is imposed; the shear stress and associated friction drag is computed based on the flow details in the local flow field.

Periodic: Periodic or cyclic boundary conditions are arised from a different type of symmetry in a problem. To apply periodic boundary conditions we need to set the flux of all flow variables leaving the outlet cyclic boundary equal to the flux of entering the inlet cyclic boundary. This is achieved by equation the values of each variable at the nodes just upstream and downstream of the inlet plane to the nodal values just upstream and downstream of the outlet plane.

Axis: In the present study, the axis boundary condition is applied for the simulation of flow around four axisymmetric bodies of revolution. Since the geometry of an axisymmetric bodies are, in effect, a semicircle rotated about an axis parallel to the free stream velocity, the bottom boundary of the domain is modeled as an axis boundary. The axis boundary type must be used as the centerline of an axisymmetric geometry (Fluent Inc. 2005). To determine the physical values for a particular variable at a point on the axis, FLUENT uses the cell value in the adjacent cell. For the axisymmetric solver, the first derivative of the axial velocity and the pressure along the radial direction is taken equal to zero. The radial velocity is taken equal to zero.

$$\frac{\partial u}{\partial r} = 0$$

$$\frac{\partial p}{\partial r} = 0$$

$$v = 0$$

3.3 Turbulence Modeling

Turbulence modeling is a key issue in most CFD simulations. Since most of the flows of engineering interest are turbulent, the appropriate treatment of turbulence will be crucial to the success of CFD. Turbulence could be thought of as instability of laminar flow that

occurs at high Reynolds numbers. Whenever turbulence is present in a certain flow it appears to be the dominant over all other flow phenomena. The flow field of a Newtonian fluid is fully described by the Navier-Stokes equation. However, turbulent flows contain small fluctuations. The resolution of such small motions requires fine grids and time steps, such that a direct simulation becomes unfeasible for high Reynolds numbers. That is why successful modeling of turbulence greatly increases the quality of numerical simulations.

Nowadays turbulent flows may be computed using several different approaches. Three common computational methods are used for the simulation of turbulent flows (Turbulence-Modelling Wiki., 2007):

- Direct Numerical Simulation (DNS)
- Large Eddy Simulation (LES)
- Reynolds-Averaged Navier-Stokes (RANS)

In the present study, Reynolds-Averaged Navier-Stokes (RANS) is used for the simulation of turbulent flow. The RANS equations are time-averaged equations of motion for fluid flow. They are primarily used while dealing with turbulent flows. These equations can be used with approximations based on knowledge of the properties of flow turbulence to give approximate averaged solutions to the Navier-Stokes equations. To illustrate the influence of turbulent fluctuations on the mean flow we re-write the instantaneous continuity and Navier-Stokes equations for two dimensional flow of an incompressible Newtonian fluid.

$$\left. \begin{aligned} \operatorname{div} \vec{u} &= 0 & (a) \\ \frac{\partial u}{\partial t} + \operatorname{div} \left(u \vec{u} \right) &= -\frac{1}{\rho} \frac{\partial p}{\partial x} + \nu \operatorname{div} \operatorname{grad} u & (b) \\ \frac{\partial v}{\partial t} + \operatorname{div} \left(v \vec{u} \right) &= -\frac{1}{\rho} \frac{\partial p}{\partial y} + \nu \operatorname{div} \operatorname{grad} v & (c) \end{aligned} \right\} \quad (3.22)$$

Since div and grad are both differentiations then for a fluctuating vector $\vec{a} = \vec{A} + \vec{a}'$ and its combinations with a fluctuating scalar $\varphi = \Phi + \varphi'$ we have the following relations [Versteeg and Malalasekera, 1995]:

$$\overline{\text{div } \vec{a}} = \text{div } \vec{A}; \quad \overline{\text{div grad } \varphi} = \text{div grad } \varphi$$

$$\overline{\text{div}(\varphi \vec{a})} = \text{div}(\overline{\varphi \vec{a}}) = \text{div}(\overline{\varphi} \vec{A}) + \text{div}(\overline{\varphi' \vec{a}'}) \quad (3.23)$$

To investigate the effects of fluctuations we replace in Equation (3.22) the flow variables \vec{u} (hence also u , v and w) and p by the sum of a mean and fluctuating components. Thus

$$\vec{u} = \vec{U} + \vec{u}'; \quad u = U + u'; \quad v = V + v'; \quad p = P + p'$$

Then the time average is taken applying the rules stated in (3.23). Considering the continuity equation first we note that $\overline{\text{div } \vec{u}} = \text{div } \vec{U}$. This yields the continuity equation for the mean flow

$$\text{div } \vec{U} = 0 \quad (3.24a)$$

A similar process is now carried out on the x -momentum equation. The time average of the individual terms in this equation can be written as follows:

$$\frac{\partial \overline{u}}{\partial t} = \frac{\partial U}{\partial t}; \quad \overline{\text{div}(u \vec{u})} = \text{div}(U \vec{U}) + \text{div}(\overline{u' \vec{u}'})$$

$$-\frac{1}{\rho} \frac{\partial \overline{p}}{\partial x} = -\frac{1}{\rho} \frac{\partial P}{\partial x}; \quad \overline{v \text{ div grad } u} = v \text{ div grad } U \quad (3.24b)$$

Substitution of these results gives the time-average x -momentum equation

$$\frac{\partial U}{\partial t} + \text{div}(U \vec{U}) + \text{div}(\overline{u' \vec{u}'}) = -\frac{1}{\rho} \frac{\partial P}{\partial x} + v \text{ div grad } U \quad (3.25a)$$

$$\frac{\partial V}{\partial t} + \text{div}(V \vec{U}) + \text{div}(\overline{v' \vec{u}'}) = -\frac{1}{\rho} \frac{\partial P}{\partial y} + v \text{ div grad } V \quad (3.25b)$$

It is important to note that the 1st, 2nd, 4th and 5th terms in Equations (3.25a & b) also appear in instantaneous Equations (3.22a-c), but the process of time averaging has introduced new 3rd terms in the resulting time-average momentum equations. The terms involve products of fluctuating velocities and constitute convective momentum transfer due to the velocity fluctuations. It is customary to place these terms on the right hand sides of the Equations (3.25a & b) to reflect their role as additional turbulent stresses on the mean velocity components U and V .

$$\frac{\partial U}{\partial t} + \text{div} \left(U \vec{U} \right) = -\frac{1}{\rho} \frac{\partial P}{\partial x} + \nu \text{div grad } U + \left[-\frac{\overline{\partial u'^2}}{\partial x} - \frac{\overline{\partial u'v'}}{\partial y} - \frac{\overline{\partial u'w'}}{\partial z} \right] \quad (3.26a)$$

$$\frac{\partial V}{\partial t} + \text{div} \left(V \vec{U} \right) = -\frac{1}{\rho} \frac{\partial P}{\partial y} + \nu \text{div grad } V + \left[-\frac{\overline{\partial u'v'}}{\partial x} - \frac{\overline{\partial v'^2}}{\partial y} - \frac{\overline{\partial v'w'}}{\partial z} \right] \quad (3.26b)$$

The extra stress terms have been written out in longhand to clarify their structure. The result from six additional stresses, three normal stresses and three share stresses:

$$\tau_{xx} = -\rho \overline{u'^2}, \quad \tau_{yy} = -\rho \overline{v'^2}, \quad \tau_{xy} = \tau_{yx} = -\rho \overline{u'v'}. \quad (3.27)$$

These extra turbulent stresses are termed the Reynolds stresses. In turbulent flows the normal stresses $-\rho \overline{u'^2}$ and $-\rho \overline{v'^2}$ are always non-zero because they contain squared velocity fluctuations. The share stresses $-\rho \overline{u'v'}$ are associated with correlations between different velocity components. If, for instance, u' and v' are statistically independent fluctuations, the time-average of their product $\overline{u'v'}$ would be zero. However, the turbulent share stresses are also non-zero and usually very large compared to the viscous stresses in a turbulent flow. The set of Equations (3.26a & b) is called Reynolds equations. Similar extra turbulent transport terms arise when we derive a transport equation for an arbitrary scalar quantity. The time average transport equation for scalar ϕ is

$$\frac{\partial \Phi}{\partial t} + \text{div} \left(\Phi \vec{U} \right) = \text{div} \left(\Gamma_{\phi} \text{grad } \Phi \right) + \left[-\frac{\overline{\partial u'\phi'}}{\partial x} - \frac{\overline{\partial v'\phi'}}{\partial y} \right] + S_{\phi} \quad (3.28)$$

Some models are used to solve the RANS equations. In this study the following models are used for the investigation of the incompressible turbulent flow over the underwater body.

- The Spalart-Allmaras
- The $k-\epsilon$ model
- The $k-\omega$ model

Both are the most common type of turbulence model and well-known as 'two equation turbulence models'. Models like the $k-\epsilon$ and the $k-\omega$ have become industry standard models and are commonly used for most of the fluid-engineering problems. Two equation turbulence models are also very much an active area of research and new refined two-equation models are still being developed.

3.3.1 The Spalart-Allmaras (S-A)

The Spalart-Allmaras turbulence model that is used in this study is a simple one-equation model that solves a modeled transport equation for the turbulent viscosity. This model is designed for wall-bounded flows and gives good results for boundary layers subjected to adverse pressure gradients, much like the flow fields encountered in this study. Although the original Spalart-Allmaras model requires that the viscous-affected region of the boundary layer be properly resolved through the use of a fine mesh inside the boundary layer, the model has been modified for its implementation in FLUENT so that wall functions are used when the mesh resolution is not sufficiently fine near object surfaces. The fact that the S-A model is a one-equation model with relatively lax grid density requirements further enhances its suitability for this particular study since, for the computer platform used, maximum computational efficiency is critical. The transported variable in the Spalart-Allmaras model, $\bar{\nu}$, is identical to the turbulent kinematic viscosity except in the near-wall (viscous-affected) region (Fluent Inc, 2005).

The transport equation for $\bar{\nu}$ is

$$\frac{\partial}{\partial t}(\rho \bar{\nu}) + \frac{\partial}{\partial x_i}(\rho \bar{\nu} u_i) = G_{\bar{\nu}} + \frac{1}{\sigma_{\bar{\nu}}} \left[\frac{\partial}{\partial x_j} \left\{ (\mu + \rho \bar{\nu}) \frac{\partial \bar{\nu}}{\partial x_j} \right\} + C_{b2} \rho \left(\frac{\partial \bar{\nu}}{\partial x_i} \right)^2 \right] - Y_{\bar{\nu}} + S_{\bar{\nu}} \quad (3.29)$$

Where, $G_{\bar{\nu}}$ is the production of turbulent viscosity and $Y_{\bar{\nu}}$ is the destruction of turbulent viscosity that occurs in the near-wall region due to wall blocking and viscous damping $\sigma_{\bar{\nu}}$ and C_{b2} are constants and ν is the molecular kinematic viscosity. $S_{\bar{\nu}}$ is a user-

defined source term. Note that since the turbulence kinetic energy k is not calculated in the Spalart-Allmaras model.

To obtain the modified turbulent viscosity, ν , for the Spalart-Allmaras model from the turbulence intensity, I and length scale, l , the following equation can be used:

$$\nu = \sqrt{\frac{3}{2}} U_{inlet} l \quad (3.30)$$

Where, $l = 0.07 \times L$

and $I = 0.16(\text{Re})^{-\frac{1}{8}}$

In this model the constants are considered as:

$$C_k = 0.1355, \quad C_{b2} = 0.622, \quad C_{i1} = 7.1, \quad C_{w2} = 0.03, \quad C_w = 2, \quad P_r = 0.667$$

3.3.2 The k - ϵ model

The k - ϵ model is one of the most common turbulence models. It is a two equation model that means, it includes two extra transport equations to represent the turbulent properties of the flow. This allows a two equation model to account for history effects like convection and diffusion of turbulent energy. The first transported variable is turbulent kinetic energy, (k). The second transported variable in this case is the turbulent dissipation, (ϵ). It is the variable that determines the scale of the turbulence, whereas the first variable, k , determines the energy in the turbulence (Fluent Inc, 2005).

In this study, Standard k - ϵ model and Realizable k - ϵ model are used to simulate the flow over circular cylinder. The standard k - ϵ model is a semi-empirical model based on model transport equations for the turbulence kinetic energy (k) and its dissipation rate (ϵ). The model transport equation for k is derived from the exact equation, while the model transport equation for ϵ is obtained using physical reasoning and bears little resemblance to its mathematically exact counterpart. In the derivation of the k - ϵ model, it is assumed that the flow is fully turbulent, and the effects of molecular viscosity are negligible. The standard k - ϵ model is therefore valid only for fully turbulent flows.

Transport Equations for the Standard k - ϵ Model for turbulence kinetic energy, k , and its rate of dissipation ϵ , are:

$$\frac{\partial}{\partial t}(\rho k) + \frac{\partial}{\partial x_i}(\rho k u_i) = \frac{\partial}{\partial x_i} \left[\left(\mu + \frac{\mu_t}{\rho_k} \right) \frac{\partial k}{\partial x_i} \right] + G_k + G_b - \rho c - Y_M + S_k \quad (3.31)$$

and

$$\begin{aligned} \frac{\partial}{\partial t}(\rho \varepsilon) + \frac{\partial}{\partial x_i}(\rho \varepsilon u_i) &= \frac{\partial}{\partial x_j} \left[\left(\mu + \frac{\mu_t}{\sigma_\varepsilon} \right) \frac{\partial \varepsilon}{\partial x_j} \right] + \\ C_{1\varepsilon} \frac{\varepsilon}{k} (G_k + C_{3\varepsilon} G_b) - C_{2\varepsilon} \rho \frac{\varepsilon^2}{k} + S_\varepsilon \end{aligned} \quad (3.32)$$

In these equations, G_k represents the generation of turbulence kinetic energy due to the mean velocity gradients, G_b is the generation of turbulence kinetic energy due to buoyancy, Y_M represents the contribution of the fluctuating dilatation in compressible turbulence to the overall dissipation rate, $C_{1\varepsilon}$, $C_{2\varepsilon}$, and $C_{3\varepsilon}$ are constants, σ_k and σ_ε are the turbulent Prandtl numbers for k and ε , respectively, S_k and S_ε are user-defined source terms.

On the other hand the term "Realizable" means that the model satisfies certain mathematical constraints on the normal stresses, consistent with the physics of turbulent flows. The most straightforward way to ensure the realizability is to make $C_{1\varepsilon}$ variable by sensitizing it to the mean flow (mean deformation) and the turbulence (k , ε). The modeled transport equations for k is similar to Equation (3.31) and ε in the realizable k - ε model are

$$\begin{aligned} \frac{\partial}{\partial t}(\rho k) + \frac{\partial}{\partial x_i}(\rho k u_i) &= \frac{\partial}{\partial x_i} \left[\left(\mu + \frac{\mu_t}{\sigma_k} \right) \frac{\partial k}{\partial x_i} \right] + \\ \rho C_1 S_\varepsilon - \rho C_2 \frac{\varepsilon^2}{k + \sqrt{\nu \varepsilon}} + C_{1\varepsilon} \frac{\varepsilon}{k} (G_k + G_b) + S_\varepsilon \end{aligned} \quad (3.33)$$

$$\text{Where, } C_1 = \max \left[0.43, \frac{\eta}{\eta + 5} \right], \quad \eta = S \frac{k}{\varepsilon}, \quad S = \sqrt{2 S_{ij} S_{ij}}$$

In these equations, G_k represents the generation of turbulence kinetic energy due to the mean velocity gradients, G_b is the generation of turbulence kinetic energy due to buoyancy, Y_M represents the contribution of the fluctuating dilatation in compressible turbulence to the overall dissipation rate, C_2 and $C_{1\varepsilon}$ are constants, σ_k and σ_ε are the

turbulent Prandtl numbers for k and ε , respectively. S_k and S_ε are user defined source terms.

The turbulence kinetic energy k is given by

$$k = \frac{3}{2} (U_{avg} I)^2 \quad (3.34)$$

Where, U_{avg} is the mean flow velocity.

The turbulence intensity I and is the turbulence length l can be found from the following equations:

$$I = 0.07 \times L \quad \text{and} \quad l = 0.16(\text{Re})^{-\frac{1}{8}}$$

Also, the turbulence dissipation rate ε defined as

$$\varepsilon = C_\rho \frac{3}{4} \frac{k^{\frac{3}{2}}}{l} \quad (3.35)$$

The constants in Standard k - ε model are considered as:

$$C_{1\varepsilon} = 1.44, \quad C_{2\varepsilon} = 1.92, \quad C_\mu = 0.09, \quad \sigma_k = 1.0, \quad \sigma_\varepsilon = 1.3.$$

And the constants in Realizable k - ε model are considered as:

$$\sigma_k = 1.0, \quad \sigma_\varepsilon = 1.2, \quad C_2 = 1.9, \quad A_0 = 4.04.$$

3.3.3 The k - ω model

The k - ω model is another common turbulence models and is used to analyze the turbulent flow over the axisymmetric bodies. This also allows a two equation model to account for history effects like convection and diffusion of turbulent energy. The first transported variable is turbulent kinetic energy k . The second transported variable in this case is the specific dissipation ω which is the variable that determines the scale of the turbulence, whereas the first variable k , determines the energy in the turbulence. k - ω model are two types; standard k - ω and Shear-Stress Transport (SST) k - ω (Fluent Inc. 2005). The SST k - ω is useful for the calculation of shear stress so this model is

considered for the simulation of submarine, pod and axisymmetric body based on Gertler' geometry.

Transport equations for the SST k - ω model are given by:

$$\frac{\partial}{\partial t}(\rho k) + \frac{\partial}{\partial x_j}(\rho k u_j) = \frac{\partial}{\partial x_j} \left(\Gamma_k \frac{\partial k}{\partial x_j} \right) + \tilde{G}_k - Y_k + S_k \quad (3.36)$$

$$\frac{\partial}{\partial t}(\rho \omega) + \frac{\partial}{\partial x_j}(\rho \omega u_j) = \frac{\partial}{\partial x_j} \left(\Gamma_\omega \frac{\partial \omega}{\partial x_j} \right) + G_\omega - Y_\omega + D_\omega + S_\omega \quad (3.37)$$

In these equations, \tilde{G}_k represents the generation of turbulence kinetic energy due to mean velocity gradients. G_ω represents the generation of ω , Γ_k and Γ_ω represent the effective diffusivity of k and ω , respectively. Y_k and Y_ω represent the dissipation of k and ω due to turbulence, D_ω represents the cross-diffusion term. S_k and S_ω are user-defined source terms.

It is so named because the definition of the turbulent viscosity is modified to account for the transport of the principal turbulent shear stress. It is such a feature that gives the SST k - ω model an advantage in terms of performance over both the standard k - ϵ and realizable k - ϵ model. Other modification includes the addition of a cross-diffusion term in the ω -equation and a blending function to ensure that the model equations behave appropriately in both the near-wall and far-field zones. In SST k - ω model the specific dissipation rate ω can be found by

$$\omega = \frac{k^{\frac{1}{2}}}{C_\mu^{\frac{1}{4}} l} \quad (3.38)$$

The constants in SST k - ω model are considered as:

$$\sigma_{k,1} = 1.176, \sigma_{\omega,1} = 2.0, \sigma_{k,2} = 1.0, \sigma_{\omega,2} = 1.168, \alpha_1 = 0.31, \beta_{1,1} = 0.075, \beta_{1,2} = 0.0828, \kappa = 0.41, C_\mu = 0.09.$$

3.4 Grid Considerations for Turbulent Flow Simulations (Y^+)

Successful computations of turbulent flows require some consideration during the mesh generation. Since turbulence (through the spatially-varying effective viscosity) plays a dominant role in the transport of mean momentum and other parameters, one must ascertain that turbulence quantities in complex turbulent flows are properly resolved if high accuracy is required. Due to the strong interaction of the mean flow and turbulence, the numerical results for turbulent flows tend to be more susceptible to grid dependency than those for laminar flows. It is therefore recommended that, one resolve with sufficiently fine meshes, the regions where the mean flow changes rapidly and there are shear layers with a large mean rate of strain.

Three parameters are significant for a computational grid: total number of grid points, location of outer computational boundaries, and minimum spacing (initial spacing normal to body surface). A RANS computation on similar geometry usually guides the determination of minimum spacing of grid from wall. The minimum spacing is generally based on y^+ , a dimensionless parameter representing a local Reynold's number in the near-wall region. This parameter is defined as:

$$y^+ \approx \frac{y u_*}{\nu} \quad (3.39)$$

Where, y = distance from wall surface,

u_* = frictional velocity,

τ_w = shear stress at the wall,

ρ = density, and

ν = kinematic viscosity.

It is recommended that, for standard wall function in k - ϵ model or when transitional flows option is not active in k - ω model the y -plus value should be $30 < y^+ < 300$. (A y^+ value close to the lower bound $y^+ = 30$ is most desirable.)

On the other hand, for enhanced wall treatment in k - ϵ model or when transitional flows option is enabled in SST k - ω model the y^+ at the wall-adjacent cell should be on the

order of $y^+ = 1$. However, a higher y^+ is acceptable as long as it is well inside the viscous sublayer ($y^+ < 5$).

It should be noted here that the y^+ value from Equation (3.39) is based on a turbulent boundary layer on a flat plate. Therefore, it is used only as an estimate in the present case as the geometry is not actually a flat plate. The y^+ values are also solution-dependant. The actual value of y^+ for the hull form is obtained with the viscous flow solution. Furthermore, the real y^+ is not a constant but varies over the wall surface according to the flow in the boundary layer.

3.5 2D Axisymmetric Model

In this study, axisymmetric model is used to simulate the turbulent flow over four axisymmetric bodies of revolution is such as: sphere, submarine (DREA) bare hull, pod, and under-water vehicle hull based on Gertler's geometry. Computer platform limitations necessitated the use of 2D axisymmetric model instead of full three-dimensional model. The use of fully 3D model is very complicated and the problems would no longer be solvable in reasonable amounts of time. As for example, the axisymmetric grids used in case of the simulation of sphere contains 17,000 cells. Assuming a similar node density in three-dimensional space, a minimum of one million cells would be needed for 3D grids of equal resolution. Also assuming that an increase in CPU time is proportional to an increase in cell count, simulations that took two to three hours in the axisymmetric cases could take 200 to 300 hours using 3D model (Gregory, 2000). This estimated increase in solution time is quite conservative – it does not consider computer platform memory limitations, additional terms required in the governing 3D fluid dynamics equations, or the additional faces added to each cell when moving from 2D to 3D. Though out-of-plane flow and complex 3D interactions (like vortex mixing) would not be modeled using axisymmetric simulations, enough similarities remained between the 3D experimental models and the axisymmetric numerical models used in this study. This necessary simplification would still allow the numerical solutions to capture the majority of the physics taking place in these complex flow fields.

Axisymmetric indicates that the domain is axisymmetric about the x -axis. When axisymmetric model is enabled, the 2D axisymmetric form of the governing equation is

solved instead of 2D Cartesian form. For 2D axisymmetric geometries, the continuity equation for incompressible flow in cylindrical co-ordinate is given by (Fluent Inc., 2005):

$$\rho \left[\frac{\partial u}{\partial x} + \frac{\partial v}{\partial r} + \frac{v}{r} \right] = S_m \quad (3.40)$$

Where, x is the axial coordinate, r is the radial coordinate, u is the axial velocity and v is the radial velocity. The source term S_m is the mass added to the continuous phase from the dispersed second phase and any user-defined sources.

Also, the axial and radial momentum equations are given by:

$$\begin{aligned} \rho \left[\frac{\partial u}{\partial t} + \frac{1}{r} \frac{\partial}{\partial x} (ru^2) + \frac{1}{r} \frac{\partial}{\partial r} (ruv) \right] = \\ - \frac{\partial p}{\partial x} + \frac{1}{r} \frac{\partial}{\partial x} \left[r\mu \left(2 \frac{\partial u}{\partial x} - \frac{2}{3} (\nabla \cdot \vec{u}) \right) \right] + \frac{1}{r} \frac{\partial}{\partial r} \left[r\mu \left(\frac{\partial u}{\partial r} + \frac{\partial v}{\partial x} \right) \right] + F_x \end{aligned} \quad (3.41)$$

$$\begin{aligned} \rho \left[\frac{\partial v}{\partial t} + \frac{1}{r} \frac{\partial}{\partial x} (ruv) + \frac{1}{r} \frac{\partial}{\partial r} (rv^2) \right] = \\ - \frac{\partial p}{\partial r} + \frac{1}{r} \frac{\partial}{\partial x} \left[r\mu \left(\frac{\partial v}{\partial x} + \frac{\partial u}{\partial r} \right) \right] + \frac{1}{r} \frac{\partial}{\partial r} \left[r\mu \left(2 \frac{\partial v}{\partial r} - \frac{2}{3} (\nabla \cdot \vec{u}) \right) \right] - 2\mu \frac{v}{r^2} + \frac{2}{3} \frac{\mu}{r} (\nabla \cdot \vec{u}) + F_r \end{aligned} \quad (3.42)$$

Where, p = static pressure, μ = molecular viscosity, ρ = density, F_x & F_r are external body forces and

$$\nabla \cdot \vec{u} = \frac{\partial u}{\partial x} + \frac{\partial v}{\partial r} + \frac{v}{r}$$

CHAPTER 4

4. NUMERICAL SIMULATION

The numerical simulation is conducted in two distinct stages. Firstly, computational models are created and simulations are run on 2D laminar and turbulent models of a circular cylinder. The computed results are compared to experimental and other numerical results to validate the computational models. Secondly, the main concentration is carried out for the simulation of axisymmetric turbulent models of under-water fluid structures. Shear Stress Transport (SST) $k-\omega$ model is used to simulate the flow over some marine structures such as sphere, pod, submarine (Defence Research Establishment Atlantic, DREA) hull and axisymmetric under-water vehicle hull. All of the investigations are carried out using very efficient commercial software FLUENT 6.2.

4.1 Simulation Using FLUENT 6.2 Based on Finite Volume Method

FLUENT 6.2 uses a finite volume-based algorithm to transform the governing physical equations to algebraic equations that can be solved numerically. In such an approach, the computational domain is subdivided into individual, discrete control volumes, or cells. The governing equations about each cell are then integrated, yielding discrete equations that conserve each quantity on a control-volume basis. Consider the following steady-state conservation equation for transport of a scalar quantity ϕ written in integral form for an arbitrary control volume V (Fluent Inc., 2005):

$$\int \rho \phi \vec{v} \cdot d\vec{A} = \int \Gamma_{\phi} \vec{\nabla} \phi \cdot d\vec{A} + \int S_{\phi} dV \quad (4.1)$$

where ρ = density

\vec{v} = velocity vector (= $ui + vj$ in 2D)

\vec{A} = surface area vector

Γ_ϕ = diffusion coefficient for ϕ

$\vec{\nabla}$ = gradient of ϕ

S_ϕ = source of ϕ per unit volume

This equation is applied to each cell in the computational domain. FLUENT discretizes this integral equation as:

$$\sum_f \vec{v}_f \phi_f A_f = \sum_f \Gamma_\phi \left(\vec{\nabla} \phi \right)_n A_f + S_\phi V \quad (4.2)$$

Where, N_{faces} = number of faces enclosing cell

ϕ = value of ϕ convected through face f

\vec{v}_f = mass flux through the face

A_f = area of face f , $|A_f|$

$\left(\vec{\nabla} \phi \right)_n$ = magnitude of $\vec{\nabla} \phi$ normal to face f

V = cell volume

The equations solved by FLUENT that lead to a full description of the flow field around a given object take the same form as the discretized equation above (Fluent Inc., 2005).

4.2 Laminar and Turbulent Flow over Circular Cylinder

4.2.1 Model geometry and boundary condition

The flow field around the cylinder is modeled in two dimensions with the axes of the cylinder perpendicular to the direction of flow. The cylinder is modeled as a circle and a square flow domain is created surrounding the cylinder. The flow from left to right with the cylinder of diameter d submersed in an incompressible fluid is considered. The



computational domain consists of an upstream 23 times the radius to downstream 40 times the radius and the width of the domain is 50 times the radius of the cylinder.

The wall boundary conditions used in this study are those of impermeability and non-slip condition, i.e., $u = 0, v = 0$. In the physical domain the flow is not confined. Nevertheless, a fictitious external rectangular boundary is needed at a large distance from the cylinder in order to solve the governing equations numerically. Uniform free stream condition with velocity is applied at the inlet boundary. The periodic condition is considered at the lateral boundaries. Also the flow at exit is treated as a pressure outlet. The problem setup together with the important dimensions is shown in Figure 4.1.

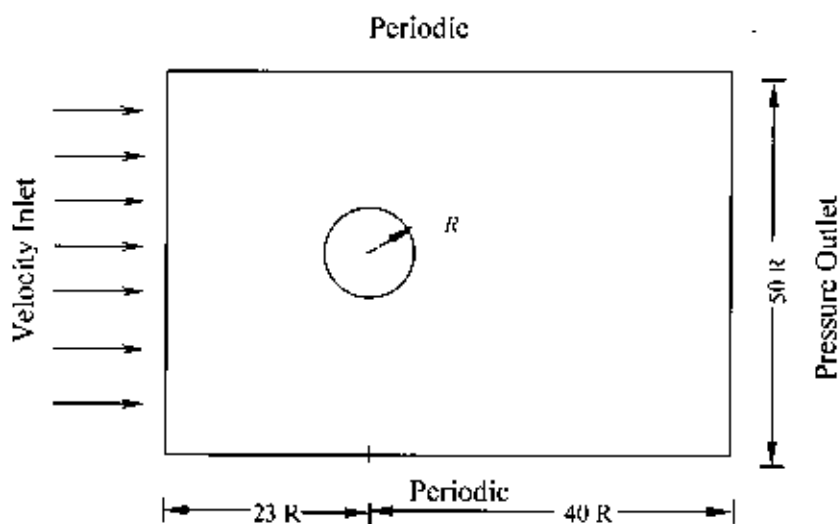


Figure 4.1: Schematic Diagram of the Flow Field around Circular Cylinder with Boundary Condition

4.2.2 Grid Generation

GAMBIT, the preprocessor of FLUENT 6.2 is used to generate the two dimensional grid around a circular cylinder in this study. A typical computational mesh is used for simulation shown in Figure 4.2. This particular mesh has approximately 15659 nodes, 30924 faces and 15380 quadrilateral cells with considerable mesh concentration both around the cylinder and in the wake. To facilitate meshing, a square with side length of three times diameter of the cylinder is created around the cylinder.

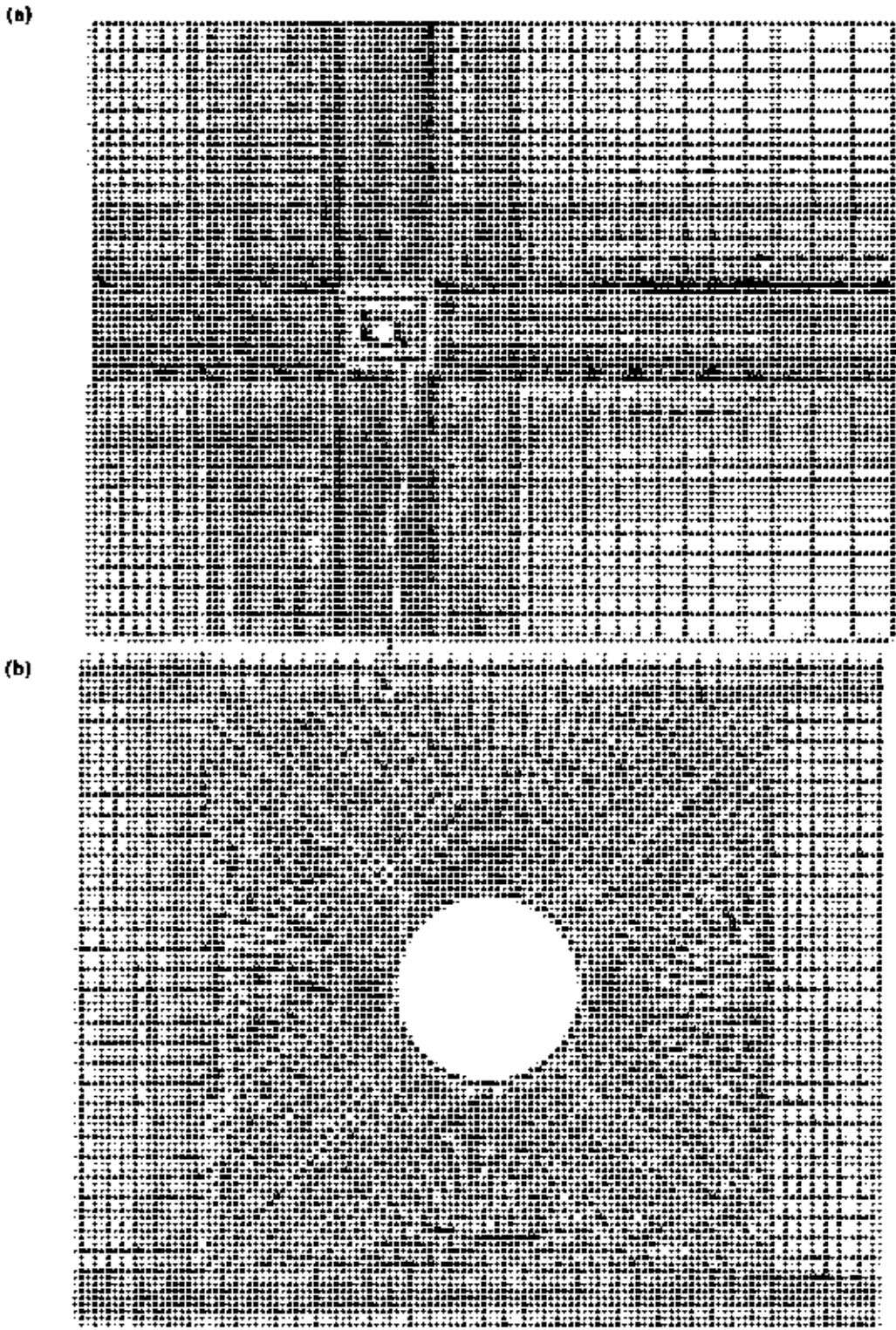


Figure 4.2: Grid Lines in Mesh: (a) Overall View, (b) Close-up View Near the Cylinder.

4.3 Axisymmetric Model Geometry and Grid Generation

GAMBIT is used to create the geometry for each of the axisymmetric models. First, it is necessary to determine the size of the numerical domain that is used for the models. Although multiple models are built with different grids in order to analyze its effects on the solution, only the optimum domain is discussed here.

4.3.1 Axisymmetric grid around sphere

The computational domain is extended ten times the sphere diameter in fore and aft of the sphere respectively. The region also extended to ten times the sphere diameter in the vertical direction from the edge shown in Figure 4.3 (a). It is ensured that in the selected model, the numerical results would be accurate and that the problem would be solvable in a reasonable amount of time.

GAMBIT is used to create an axisymmetric grid based on the sphere's geometry described above. For the purposes of grid construction, the computational domain for sphere model is divided into two regions: the boundary layer region and the free stream region. Dividing the domain in this fashion is a common practice in problems where the effects of the viscous boundary layer that forms on the body are expected to significantly affect the flow field and where enhanced grid resolution in the vicinity of the boundary layer is important. The boundary layers are attached to the spheres and the direction of the boundary layer grids is defined such that the grids extended into the interior of the domains. Based on prior experience with numerical simulations involving boundary layers and the expected growth of the boundary layer meridionally along the sphere, both boundary layer meshes are approximately 3 cm in height. Increasing the number of rows in the boundary layer meshes only served to vary cell density, and did not change the total height of the mesh. Finally, the growth factors are chosen to increase the resolution of the meshes at the base of the boundary layers (where flow parameter gradients are largest) while still maintaining high grid resolution, low cell skewness at the top of the boundary layers, and a total boundary layer mesh thickness of approximately 3 cm. Low skewness is important to ensure similar cell proportions between outer boundary layer cells and neighboring free stream region cells. The boundary layer grid parameters for the axisymmetric sphere models are shown in Table 4.1. If the growth factor is not listed in the table, it is equal to unity.

Table 4.1: Boundary Layer Parameters of Axisymmetric Sphere Grids

Meridional node count on sphere	First row thickness in boundary layer	Boundary layer growth factor	Number of rows in boundary layer
120	0.0001	1.24	20

Meshing of the free stream regions took place in two steps. First, the edges of the regions are meshed, and then, using the edge meshes, the interiors of the regions (or faces) are meshed. Since boundary layer meshing has already been performed, only the axis boundary, inlet, outlet, and top edges has to be meshed. Comparatively coarse meshes are specified on the exterior (inlet, outlet, and top) boundaries due to the expected lack of large flow property fluctuations (and thus low grid densities) in those regions. For better control of edge node spacing, the bottom boundary is constructed in multiple sections. Grading is necessary to ensure a smooth transition between the relatively small cell sizes near the boundary layer grids and the relatively large cell sizes on the outer edges of the domains. Table 4.2 shows the node spacing on the edges of the domains for each edge node distribution.

Table 4.2: The Node Spacing of Sphere on the Edges of the Domains for Each Edge Node Distribution

Node on front section 1	Growth factor on front section 1	Node on front section 2	Node on rear section 1	Growth factor on rear section 1	Node on rear section 2	Growth factor on rear section 2	Node count on top boundary
50	0.9	12	50	1.111	12	20	40

For the purpose of grid construction, the computational domain is divided into three faces: Middle face, Front face and Rear face. At first the edges of the faces are meshed, and then, using the edge meshes, the interiors of the faces are meshed. The node spacing on the edges of the domain for each node distribution is given in the Table 4.3.

Table 4.3: Axisymmetric Sphere Boundary Node Spacing Distributions

Front face		Middle face		Rear face		Normal to the axis	
No. of Nodes	Growth factor	No. of Nodes	Growth factor(both direction)	No. of Nodes	Growth factor	No. of Nodes	Growth factor
45	1.04	80	1.02	75	1.05	90	1.05

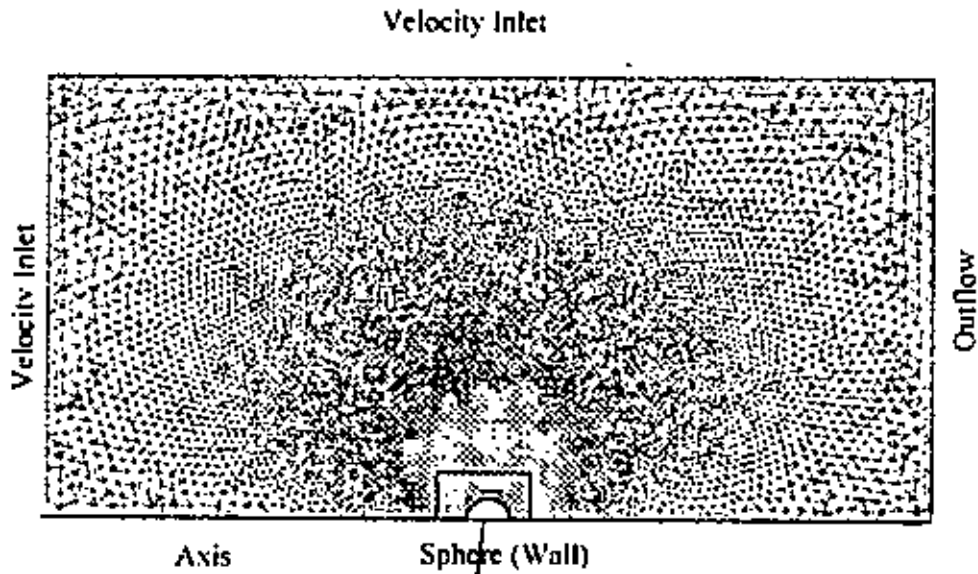


Figure 4.3: (a) Axisymmetric sphere Unstructured Grid with Boundary Conditions

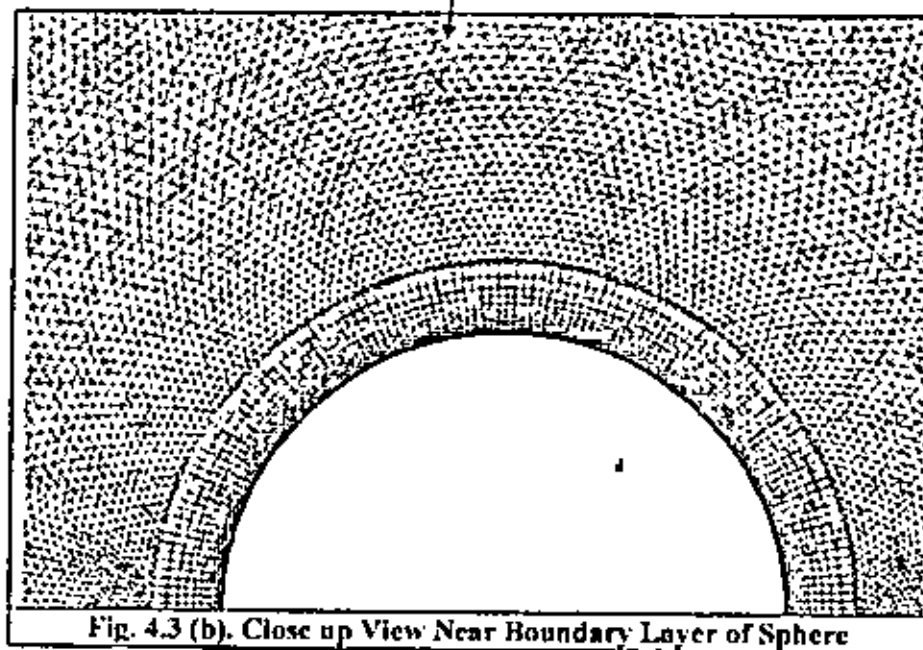


Fig. 4.3 (b). Close up View Near Boundary Layer of Sphere

Once the edges are meshed, the interior of the domains need to be meshed using automatic face mesh generation scheme of GAMBIT. The meshing scheme that is chosen is pave meshing scheme. The pave scheme creates an unstructured grid of mesh elements, which is particularly desirable for its applicability to a wide range of face geometries, its ability to deal with irregularly shaped interiors, and its ease of use. There is no restriction on mesh node spacing imposed by the pave scheme since only

triangular face elements are used. More cells are constructed near the surface of the sphere to tackle the high velocity gradient in the boundary layer region of the viscous flow. Figure 4.3(a) shows the grid for the axisymmetric sphere, which is symmetric about the axis of rotation. Also, Figure 4.3(b) shows the close up view that visualizes the boundary layer clearly.

4.3.2 Axisymmetric grid around DREA submarine bare hull

For this stage of the study, the computational domains are created around the DREA (Defence Research Establishment Atlantic) standard submarine bare hull as used by Department of Research and Development Canada, 1988. The geometry of the hull is considered to stay consistent with the experimental result. A numerical investigation has also been carried out by Baker (2004) to calculate the drag force on DREA hull using CFX. Figure 4.4 shows the surface of bare submarine (DREA) hull.

In this study, only the 2D axisymmetric geometry is considered, the vertices are created using formulas given in Appendix A. The computational domain extends one body length upstream of the leading edge of the pod, one body length above the body surface and two body lengths from the trailing edge as shown in Figure 4.5. The solution domain is ensured large enough to capture the entire viscous interaction and the wake development.

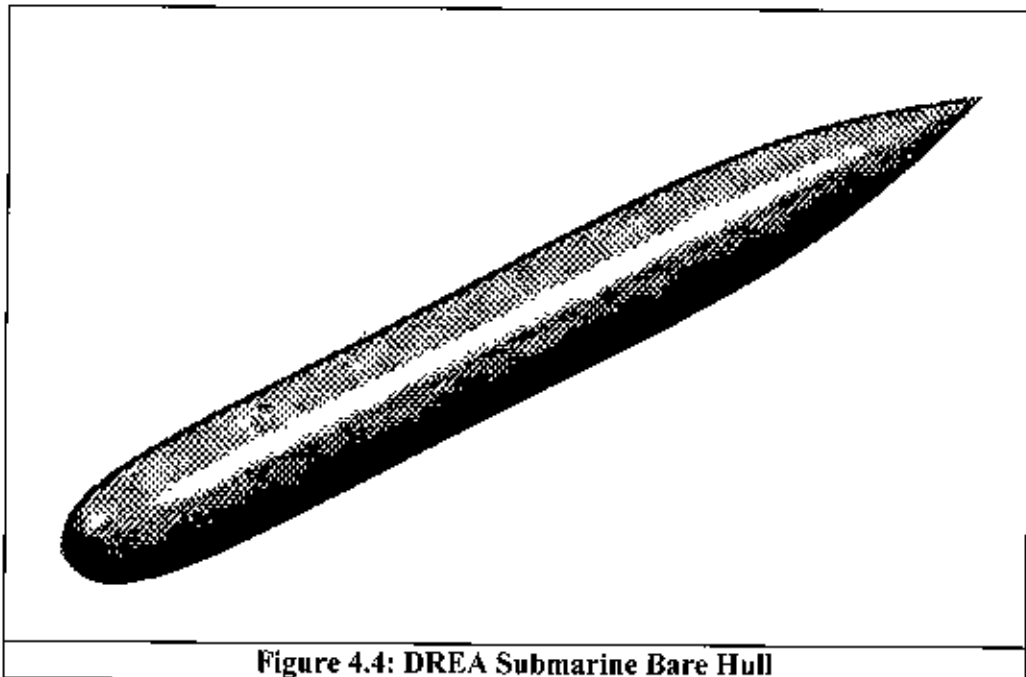


Figure 4.4: DREA Submarine Bare Hull

The mesh generation procedure for this work is based on trial and error. This needs to be fine enough to produce grid independent solutions but coarse enough to have a reasonable computation time. Figure 4.5 shows the grid for the axisymmetric model of submarine hull, which is symmetric about the axis of rotation. More cells are concentrated near the leading edge and trailing edge of the hull to capture the stagnation points. Since the fine resolution of grid points is not required near the inflow and outflow boundaries, an expansion ratio is used from the leading edge of the body to the inflow boundary and from the trailing edge to the outflow boundary. The node distribution with the expansion ratio of submarine bare hull is given in Table 4.4

Table 4.4: Axisymmetric Submarine Boundary Node Spacing Distributions

Front face		Middle face		Rear face		Normal to the axis	
No. of Nodes	Growth factor	No. of Nodes	Growth factor(both direction)	No. of Nodes	Growth factor	No. of Nodes	Growth factor
45	1.04	80	1.02	75	1.04	70	1.05

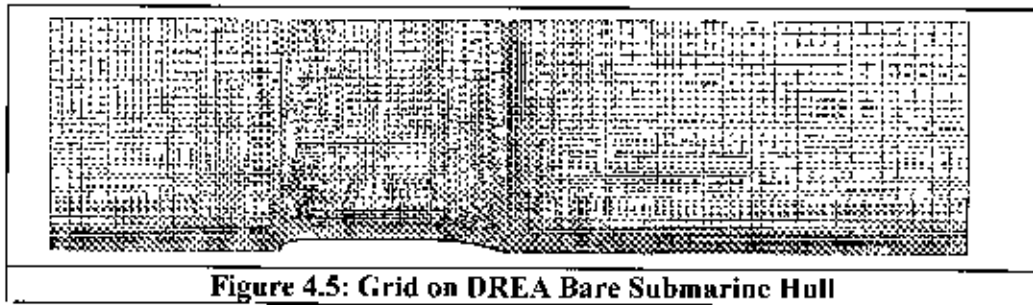


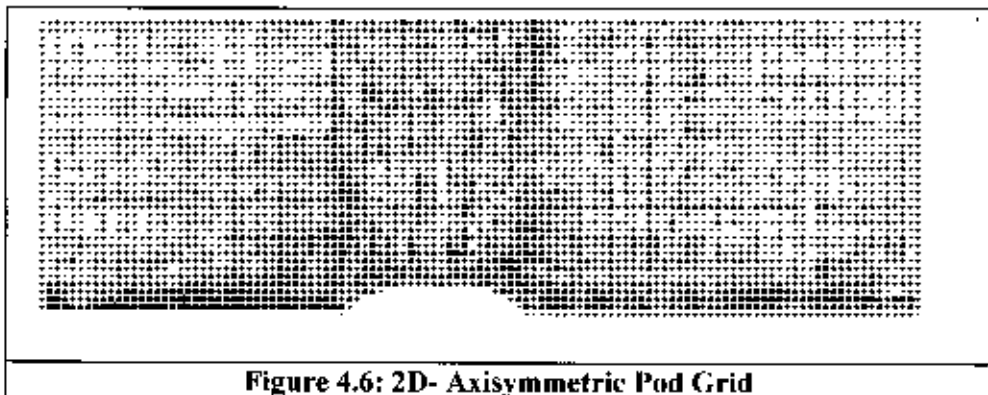
Figure 4.5: Grid on DREA Bare Submarine Hull

4.3.3 Axisymmetric grid around pod

Now a computational domain is created around an axisymmetric pod. The geometry of the pod is considered for being consistent with the numerical work of Gupta (2004) (see Appendix B). The computational domain extend 1.5 body lengths upstream of the leading edge of the pod, 1.5 body length above the body surface and two body lengths from the trailing edge as shown Figure 4.6. The solution domain is ensured large enough to capture the entire viscous interaction and the wake development. The computational domain and mesh generation are more or less identical with that of submarine (DREA) discussed in section 4.3.1.1. The node distribution with the expansion ratio of pod is given in Table 4.5

Table 4.5: Axisymmetric Pod Boundary Node Spacing Distributions

Front face		Middle face		Rear face		Normal to the axis	
No. of Nodes	Growth factor	No. of Nodes	Growth factor(both direction)	No. of Nodes	Growth factor	No. of Nodes	Growth factor
50	1.04	80	1.02	70	1.04	70	1.05

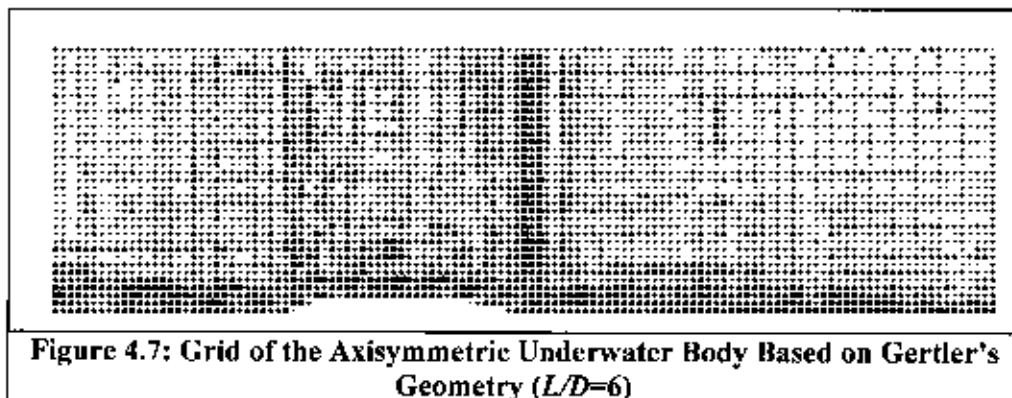
**Figure 4.6: 2D- Axisymmetric Pod Grid**

4.3.4 Axisymmetric grid around underwater vehicle hull based on Gertler's geometry

Finally, six axisymmetric underwater bodies are created with length-to-diameter (L/D) ratio ranging from four to ten. In this study, the geometries of the axisymmetric underwater bodies are constructed to be consistent with the experimental work of Gertler (1950) and the numerical work of Cheng *et al* (1995). Each body is defined by a sixth-degree polynomial derived by Gertler as shown in Appendix C. The computational domain is identical with that of submarine and pod discussed above. The boundary node spacing distributions for $L/D = 6$ is shown in Table 4.6. Also, Figure 4.7 shows the grid and boundary condition around the underwater body for $L/D = 6$. The grid generation and boundary condition of other bodies are identical to the body having $L/D=6$.

Table 4.6: Distributions of Boundary Node Spacing of Axisymmetric Underwater Body Based on Gertler's Geometry.

Front face		Middle face		Rear face		Normal to the axis	
No. of Nodes	Growth factor	No. of Nodes	Growth factor(both direction)	No. of Nodes	Growth factor	No. of Nodes	Growth factor
45	1.04	80	1.02	75	1.04	70	1.05



4.4 Solver Initialization and Flow Solution

After the grids are constructed, the next step is to import them into FLUENT 6.2, the numerical solver. Since each grid is exported from GAMBIT in FLUENT 6.2's native format, the import process is straightforward. After the grids are imported, the solver is initialized. This procedure involved several steps, such as:

- Selecting the solver formulation
- Defining physical models
- Specifying fluid properties
- Specifying boundary conditions
- Adjusting solution controls
- Initializing the flow field
- Iterating

For all of the grids generated in this study, the segregated solver formulation is used. This approach solves the continuity, momentum, and energy equations sequentially as opposed to simultaneously. Because the segregated solver is traditionally used for incompressible and mildly compressible flows, given the flow conditions being investigated, this study is well-tailored for its use. Also, the solution controls (under-



relaxation parameters, etc) are left at the default settings for all cases. Next, the flows around all of the geometries modeled in this study are approximated as steady-state condition. Although this choice precluded the ability to capture vortex shedding and other time-dependent effects, the majority of pertinent flow features and their associated drag effects (like separation point, pressure drag, and skin friction drag) could still be accurately modeled. One reason for choosing steady-state simulations is because of the reduced computational load they placed on the computer – given the total number of simulations needed, run time is a major limiting factor. The other, more compelling reason for choosing a steady-state modeling approach is that the properties of interest in this study are all steady state values. Although, in reality, separation point, skin friction, pressure, and drag all vary with respect to time on a microscopic scale, their net values and net effects can usually be considered steady properties and can accurately be modeled as such. The user interface updates based upon whether the steady or unsteady solver is selected. The time step size, the number of iterations per time step, the total number of time steps, and the convergence limit for each time step needs be specified when the unsteady solver is used. On the other hand, the total number of iterations and the convergence limit needs be specified for steady solver.

For all geometries modeled in this thesis, definition of the physical models simply involves specifying whether a laminar or turbulent simulation is desired in the solution computation. Laminar solutions are sought to compare with data in the open literature, so laminar models are specified in case of circular cylinder only. A turbulent model of circular cylinder is also simulated to compare with experimental results. Then the axisymmetric turbulent models are simulated for four axisymmetric fluid structures such as sphere, submarine (DERA) hull, pod, and axisymmetric underwater body based on Gertler's geometry. In this stage, Shear Stress Transport $k-\omega$ model is used in all of the cases. For velocity- pressure coupling the PISO algorithm (discussed in section 3.4) is used for unsteady case. The second-order discretization scheme for the momentum equation is used throughout this study.

Specifying the fluid properties and the boundary conditions is very straightforward. For every computational model in the study, the default fluid properties for water-liquid (water-liquid at standard conditions) are used. The flow velocity is used for the selection of Reynolds numbers in all of the cases except the laminar model. In case of laminar

simulation of cylinder the density is used in this regards. Also, the boundary condition types are all specified during the grid generation step, so the only addition needed is to specify the inlet velocity.

For all flow cases, the flow field is initialized from the inlet boundary condition. This process is necessary to provide a starting point for the evolution of the iterative solution process. In every case, after the flow is successfully initialized, the solution is iterated until one of the following three conditions is attained: convergence, divergence, or non-decaying oscillation of the residuals. Convergence is declared if the x-velocity, y-velocity, and continuity residuals all dropped below 0.001.

CHAPTER 5

5. RESULT AND DISCUSSION

5.1 Definitions

The major benefit of CFD analysis is its ability to compute the values of every flow parameter at each grid point in the domain studied, giving a very descriptive picture of the entire flow field. The present study can be classified to in two main parts: Firstly, the 2D laminar and turbulent flows over circular cylinder and then the axisymmetric turbulent flows over axisymmetric under-water bodies of revolution are simulated.

The drag coefficient is computed as

$$C_p = \frac{D}{\frac{1}{2} \rho_{ref} U_{ref}^2 S} \quad (5.1)$$

Where $D =$ drag force

$S =$ appropriate reference area

As explained earlier, the drag force D consisted of two parts: the pressure drag and the skin friction drag. Pressure drag is simply the component of the pressure force acting in the axial direction. Skin friction drag is a function of the fluid viscosity and the velocity profile at the surface of the body. FLUENT 6.2 directly computed both pressure drag and skin friction drag by numerically integrating the incremental value of each at every node point along the body surface. The pressure coefficient is calculated using the formula:

$$C_p = \frac{P_{gauge}}{\frac{1}{2} \rho_{ref} U_{ref}^2} \quad (5.2)$$

where

$$P_{gauge} = \text{gauge pressure} = p - p_{ref}$$

ρ_{ref} = reference density

U_{ref} = reference velocity

For this study, reference conditions are taken as those values for water liquid at standard temperature and pressure; in other words,

$$p_{ref} = 101325 \text{ N/m}^2$$

$$\rho_{ref} = 988.2 \text{ kg/m}^3$$

$$\mu_{ref} = 0.001003 \text{ kg/m-s}$$

The location of the reference pressure is always given as on the left edge of the inlet boundary. The reference velocity is used to choose the Reynolds number for different flows.

The skin friction coefficient is calculated as:

$$C_f = \frac{\tau_{wall}}{\rho_{ref} U_{ref}^2} \sqrt{\text{Re}} \quad (5.3)$$

where τ_{wall} = wall shear stress

Re = Reynolds number based on body diameter/length.

Reynolds number for this study is computed as

$$\text{Re}_{D_j} = \frac{\rho_{ref} U_{ref} L}{\mu_{ref}} \quad (5.4)$$

Where, L is the characteristic length. The boundary layer separation point occurs when skin friction on a body surface goes to zero. Thus, it is simple to determine the boundary layer separation point for each computational model by analyzing plots of C_f versus

axial position. Also, the dimensionless frequency of vortex shedding is the Strouhal number, expressed as $St = \frac{fd}{U}$ (5.5)

Where, f is the frequency of the vortex shedding ($=1/T$), d is the diameter of the circular body and U the free stream velocity. And the dimensionless wall vorticity defined as $\omega_w = \omega R/U$ (5.6)

Finally, the difference of the computed result from experimental result is calculated using the formula:

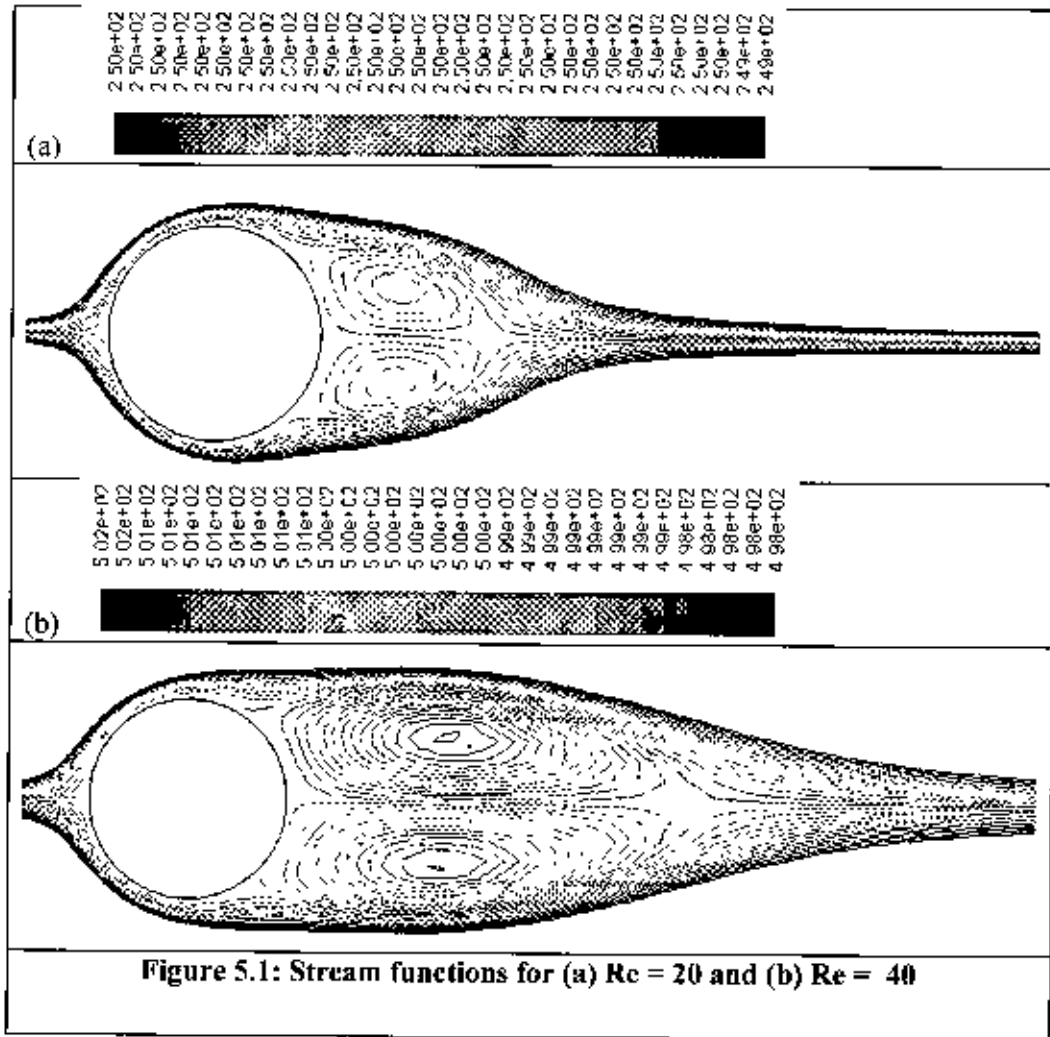
$$\% \text{difference } \phi = \frac{|\phi_{\text{cal}} - \phi_{\text{exp}}|}{\phi_{\text{exp}}} \times 100 \quad (5.7)$$

Where, ϕ is the required parameter.

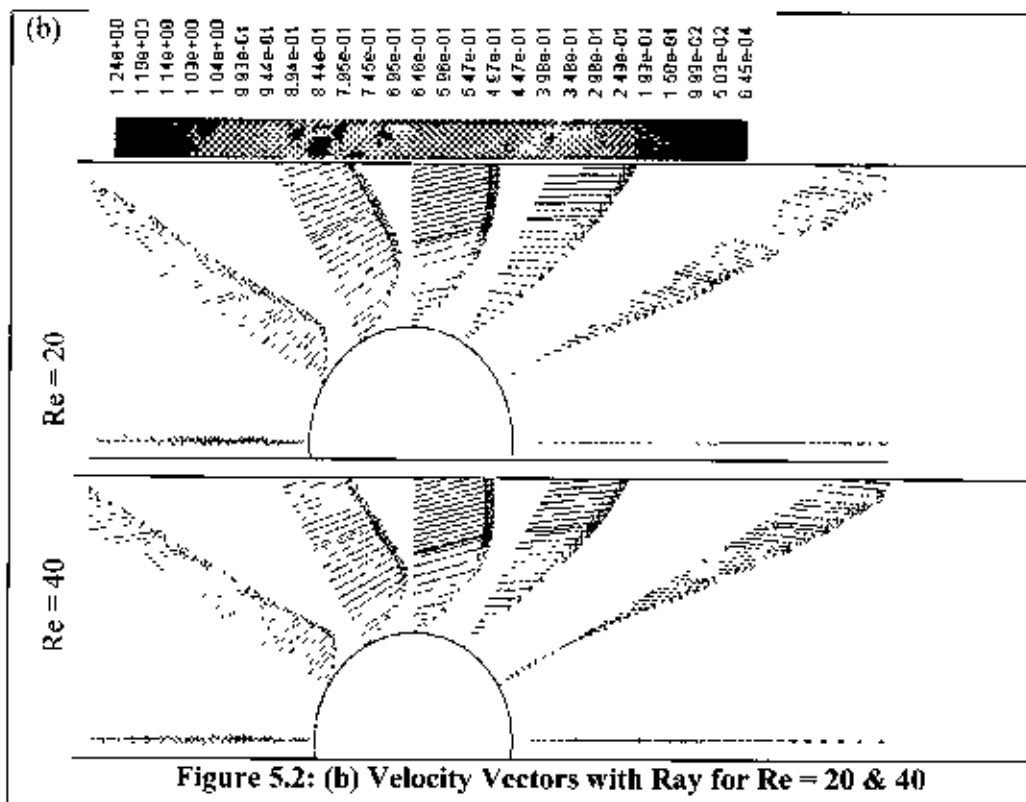
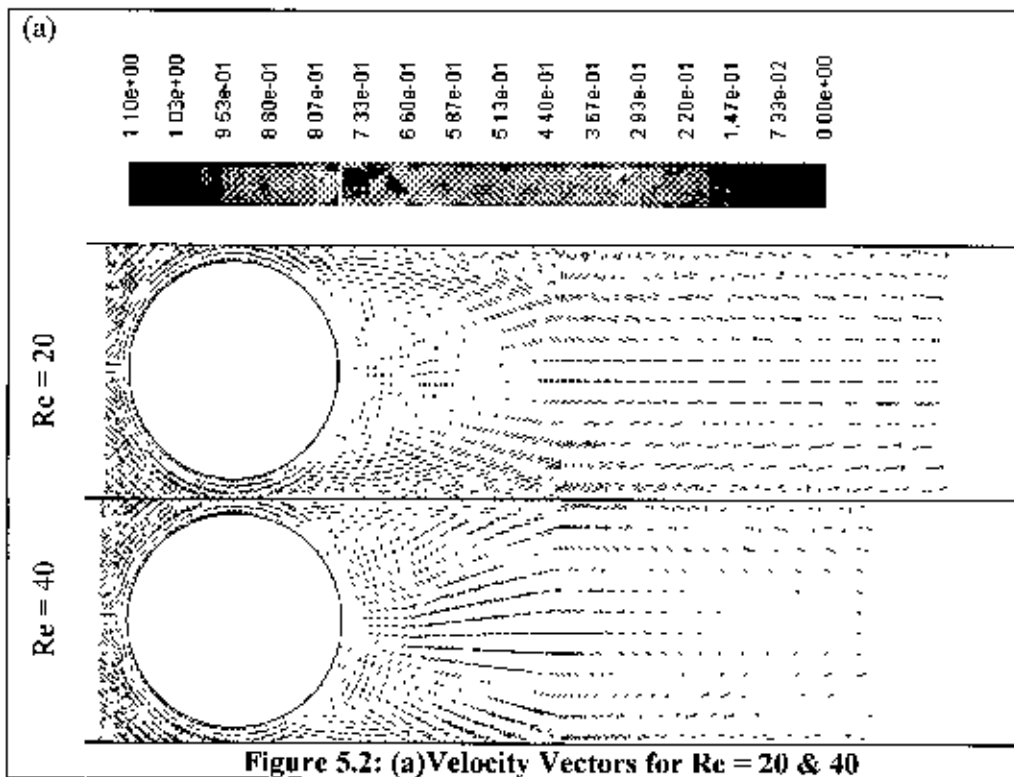
5.2 Flow over Circular Cylinder

5.2.1 The laminar flow

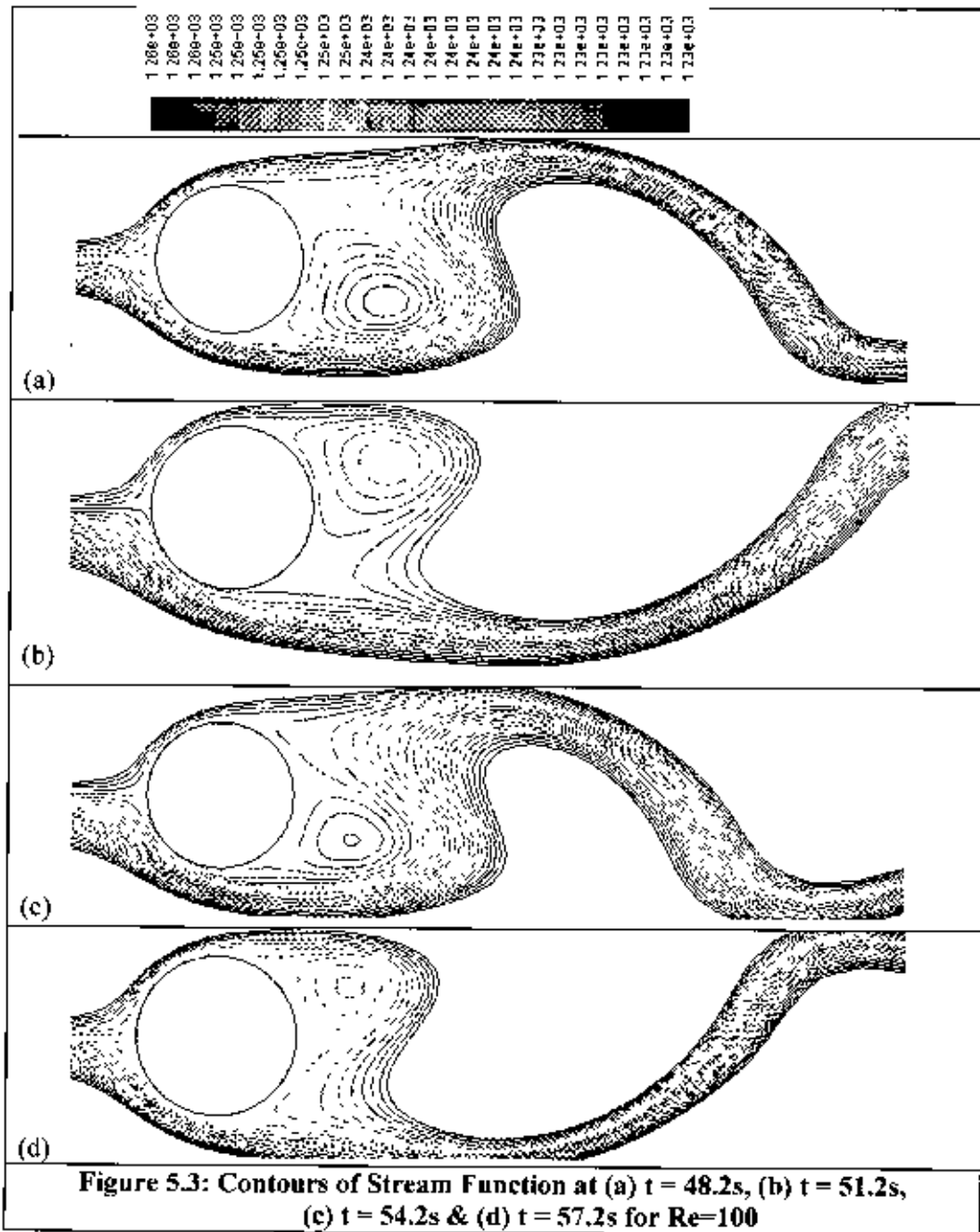
The steady laminar flow around 2D circular cylinder is reported first to allow comparison with experimental results. For Reynolds numbers = 20, the flow reaches a steady state at $t = 7\text{sec}$ whereas for $Re=40$, it takes $t = 15\text{sec}$ to reach steady state (Braza 1986). The stream functions for these Reynolds numbers are shown in Figure 5.1. Two symmetric vortices are clearly observed behind the cylinder. The velocity vectors in the wake of the cylinder are also shown in Figure 5.2(a) for $Re = 20$ & 40 respectively. The boundary layer profile is clearly observed at several rays extending from the cylinder, namely at angles of 0° , 30° , 60° , 90° , 120° , 150° , and 180° from the front stagnation point as shown in Figure 5.2(b). As Reynolds number becomes higher than 40 the flow reports a loss of symmetry in the wake and alternating eddies are formed and convected in the wake. This generates the alternating separation of vortices, which are convected and diffused away from the cylinder, forming the well-known Karman vortex streets. Such destabilizing effects always occur during any physical experiment on the flow around a circular cylinder. The Strouhal number as defined by Equation (5.5) is found to be 0.164 for $Re=100$. This result agrees well with the experimental value (0.164–0.165) reported by Tritton (1959).



The results of unsteady laminar flow for $Re = 100$ are presented in Figures 5.3-5. The instantaneous stream lines for $Re = 100$ are shown in Figure 5.3 at the four phases during one cycle of vortex shedding. In Figure 5.4 & Figure 5.5 the directions of the velocity vectors and corresponding contours of pressure are plotted respectively at those phases for the same Reynolds number. The alternating formation, convection and diffusion of the vortices are clearly shown.



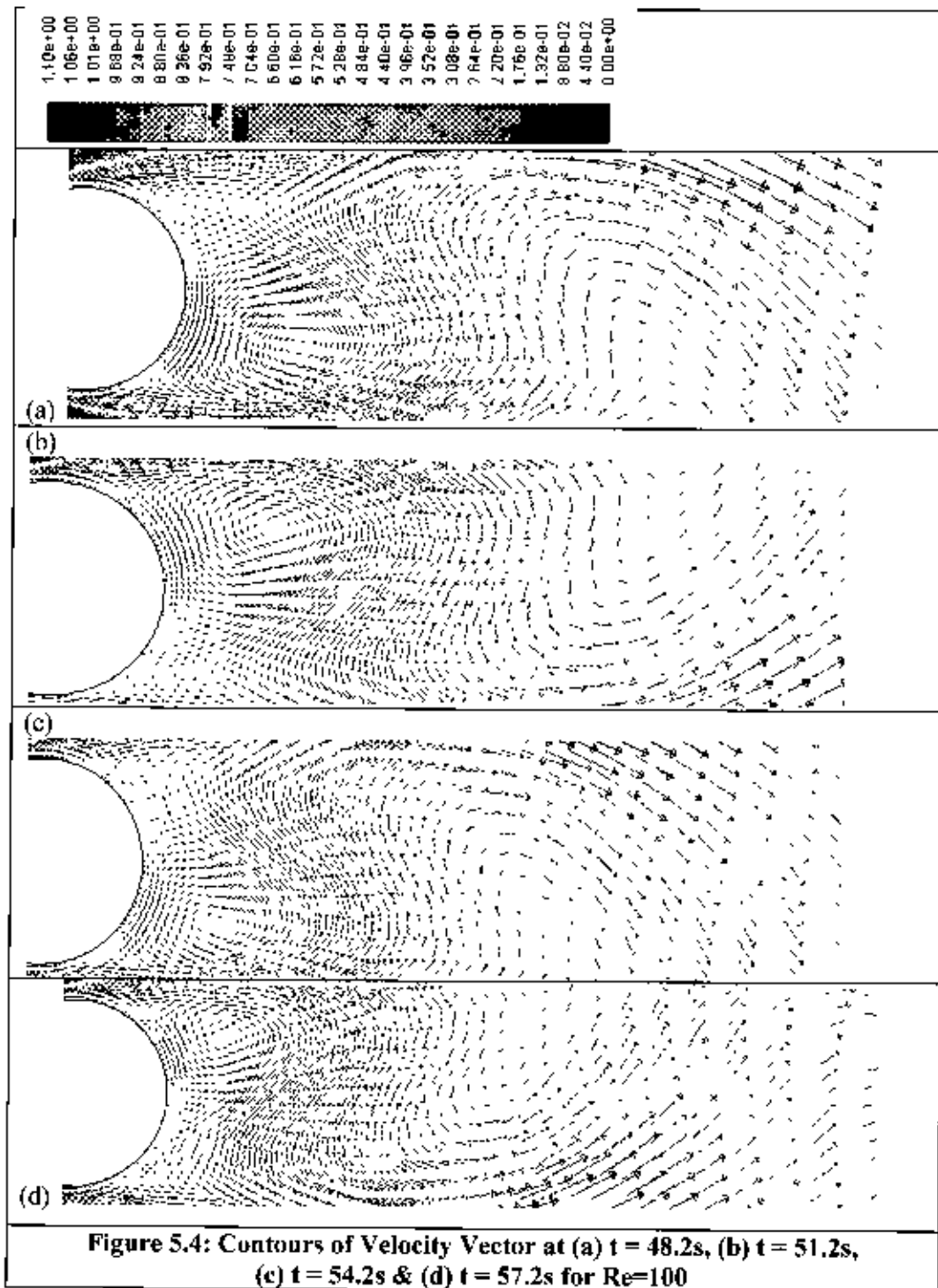
105896

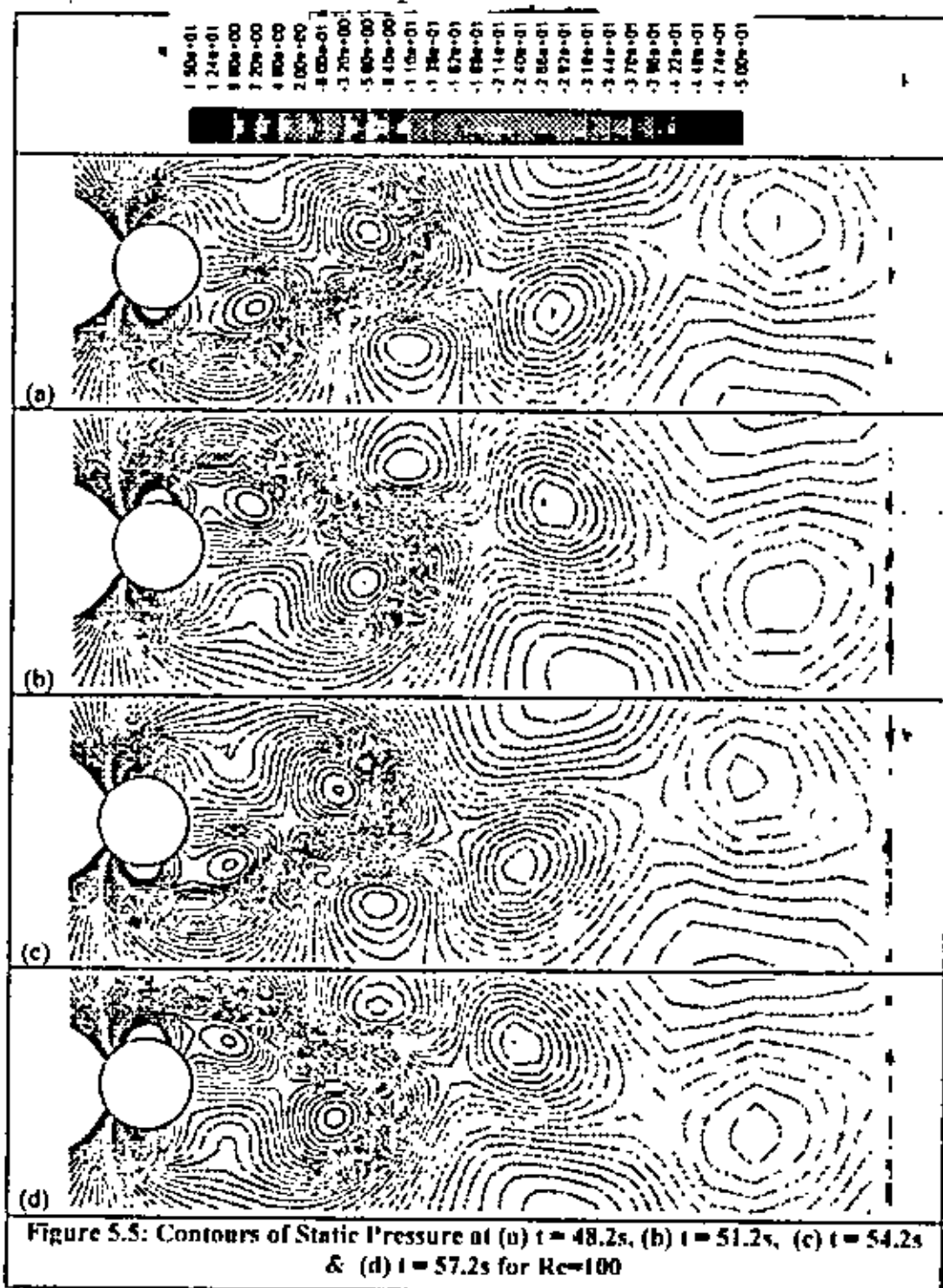


5.2.2 The Turbulent Flow

The experimental work of Roshko (1954) locates the beginning of the laminar-to-turbulent transition at Reynolds numbers 200 – 300. Beyond this Reynolds number but less than 3×10^5 the wake of the cylinder is completely turbulent and the boundary layer

separation is laminar (Sumer, 1997). It is known that the flow around the cylinder is two dimensional only when $Re < 200$.





For larger Reynolds number, the vortex shedding occurs in cells and therefore the flow is generally simulated in 3-D. But the 3-D simulation is very much complicated and computational cost is very high. Therefore, the turbulent flow over a circular cylinder

for Reynolds numbers 1000 & 3900 is investigated here using 2-D finite volume method.

In this research, the turbulent flow for both Reynolds numbers is simulated using three turbulence models namely, $k-\epsilon$ Standard, $k-\epsilon$ Realizable and Shear-Stress Transport (SST) $k-\omega$ model. The vortex shedding is observed and the drag and lift forces are also calculated using these methods. For unsteady case, time interval has been chosen small enough to capture the vortex shedding. The easiest way to set up the right time step size is one that ensures the maximum Courant number very near to unity. To avoid running the case for very long time, a small perturbation has been introduced in the domain. This perturbation is generally in the form of very small velocity in perpendicular direction to the flow direction. This assists the solver to start vortex shedding quickly. Since there is nothing to sustain this perturbation in the domain for very long time, it dies out and did not affect the calculation of C_L and C_D . The dimensionless frequency of vortex shedding is the Strouhal numbers found by different methods are shown in Figure 5.6. The vortex shedding is visualized by means of the contours of stream function, velocity vectors and static pressure. Figure 5.7 shows the stream function during one cycle of lift coefficient at $Re = 1000$. At the same time the velocity vector and pressure fields are also shown in Figure 5.8 and 5.9 respectively.

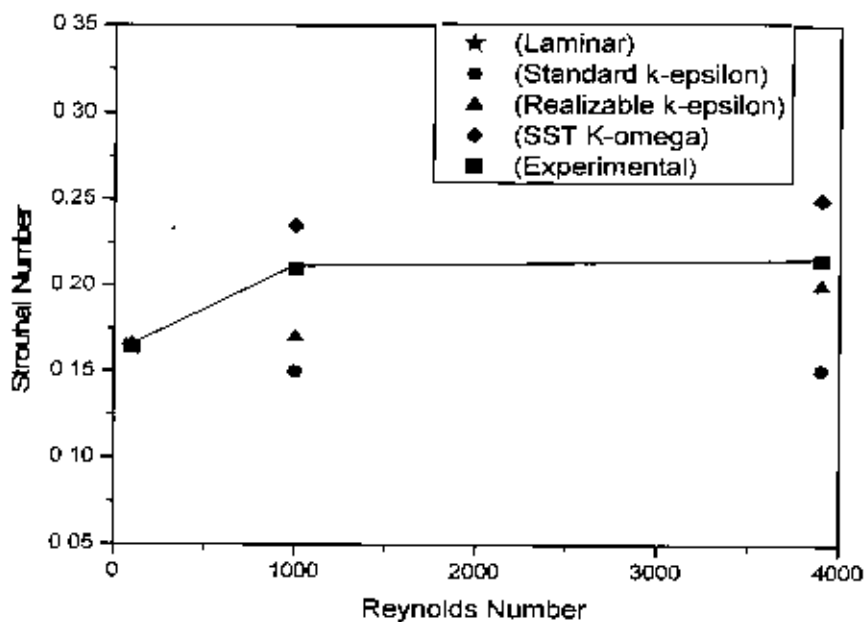
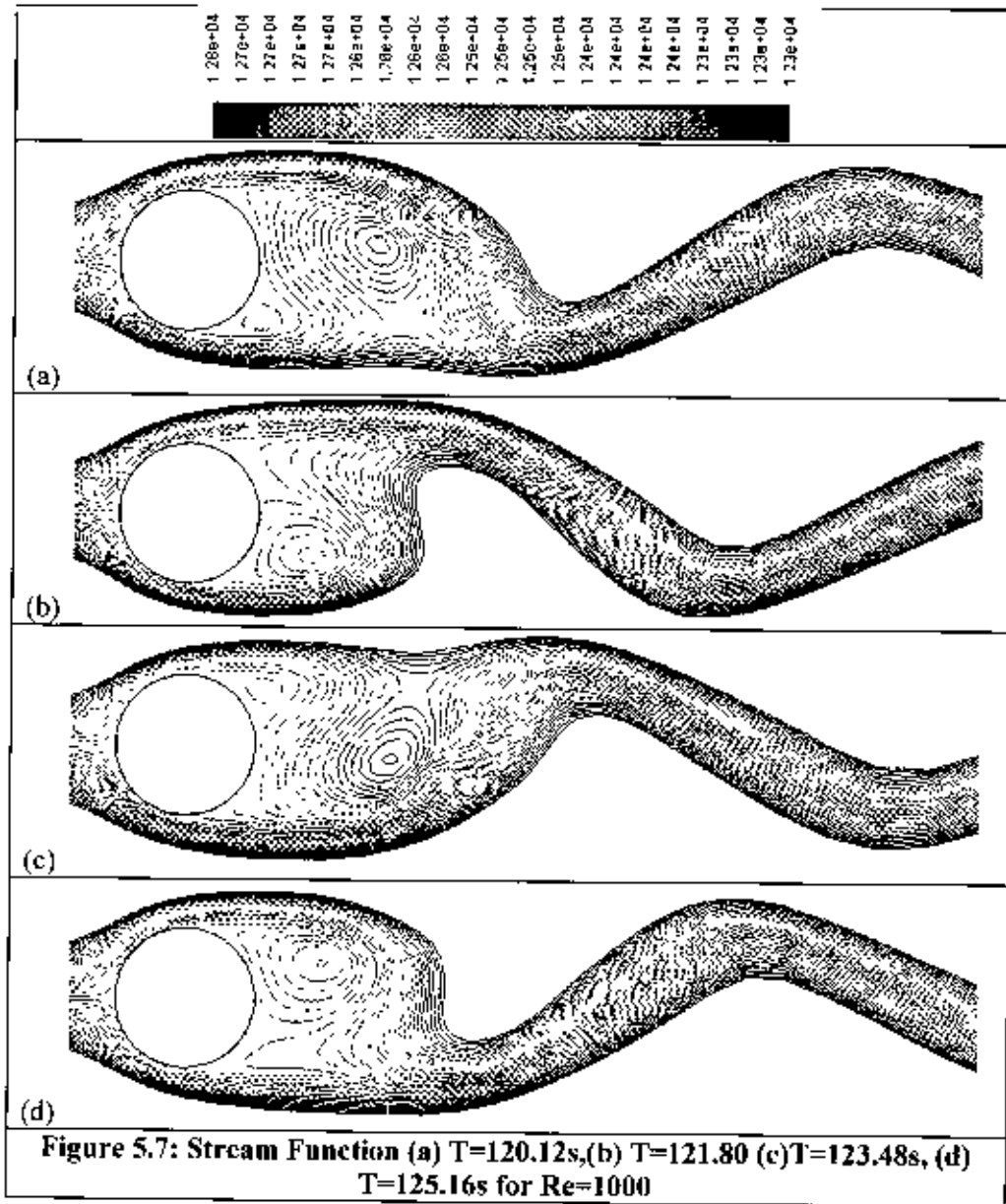
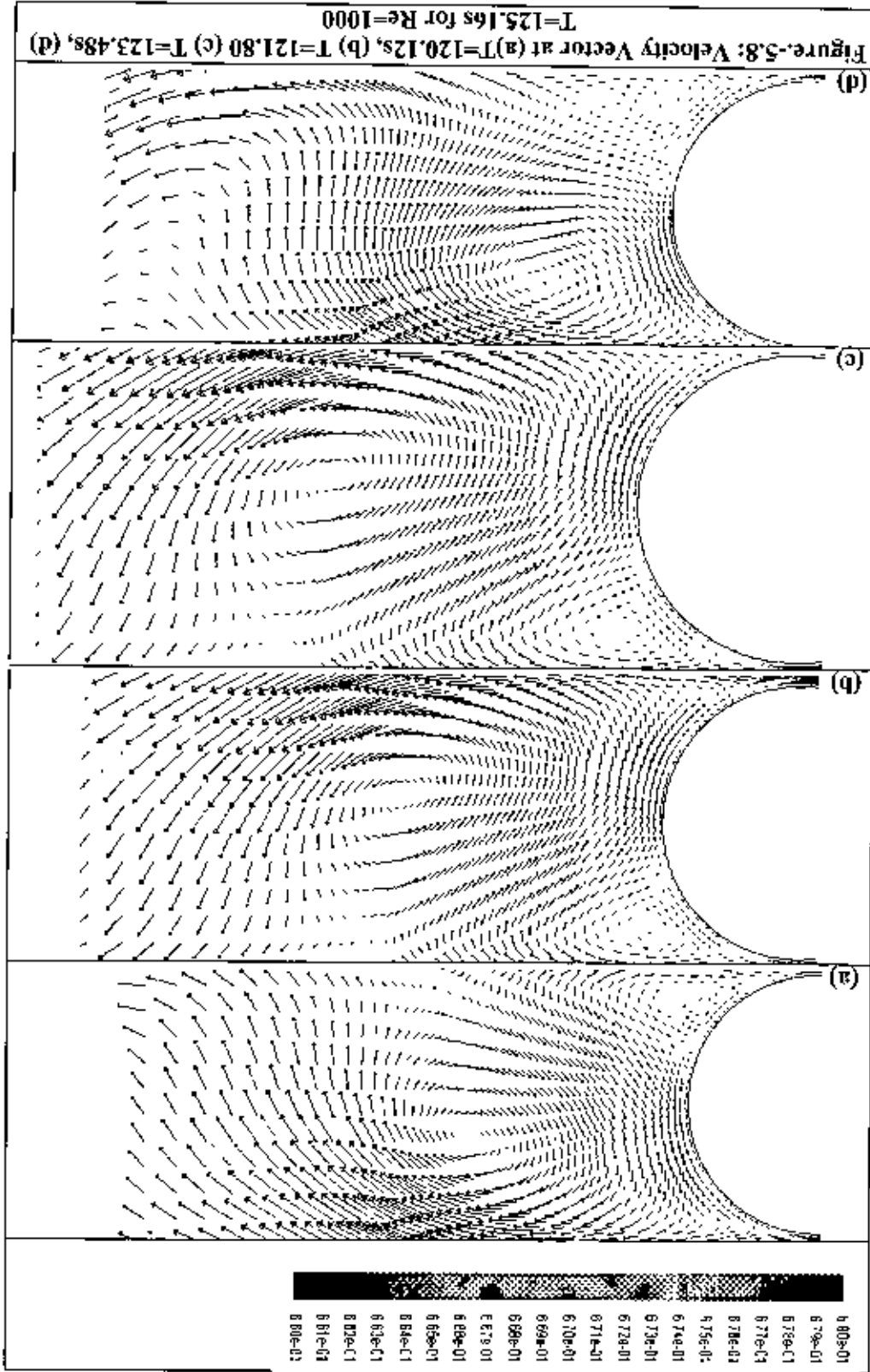


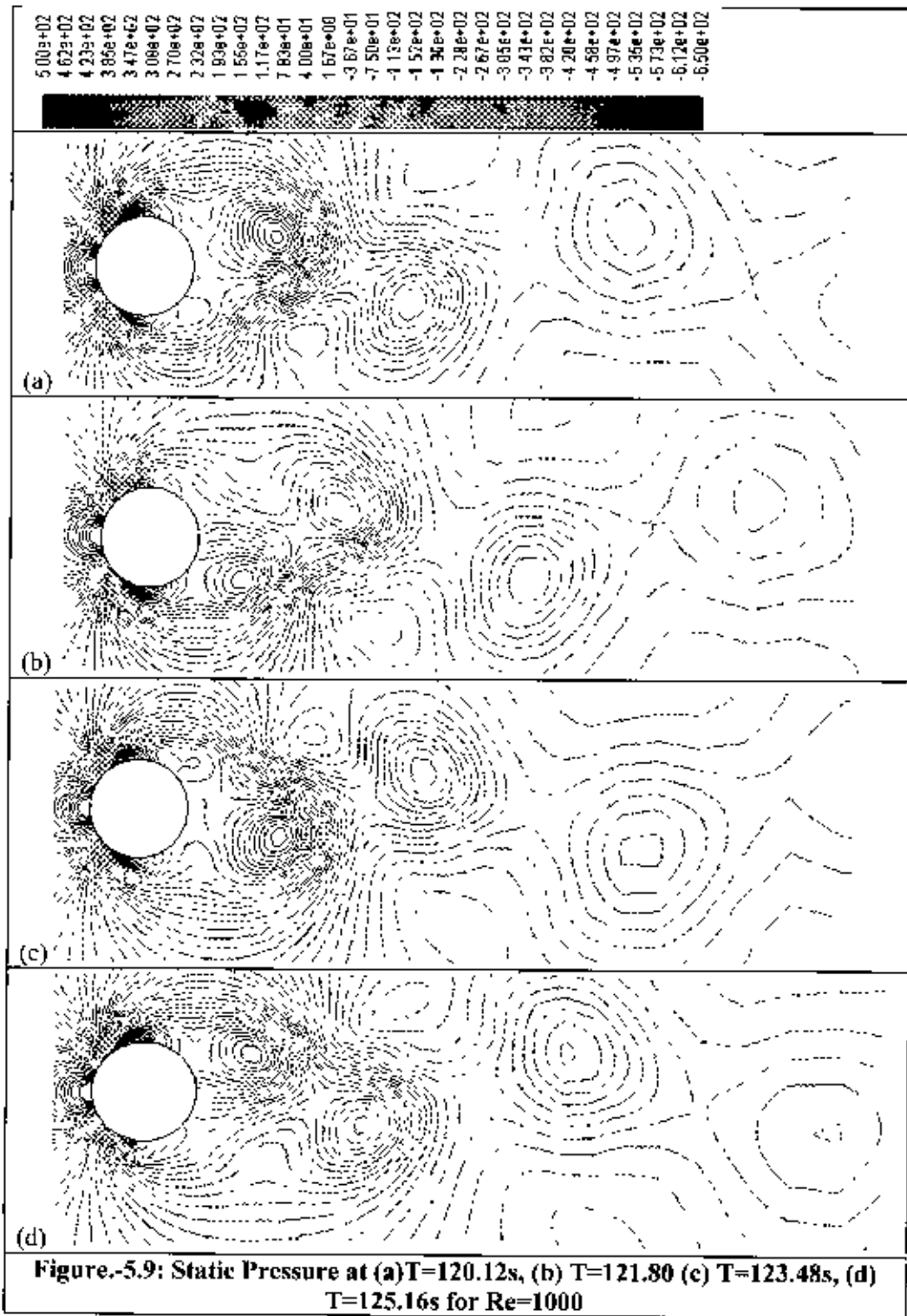
Figure 5.6: Strouhal Number Vs Reynolds Number

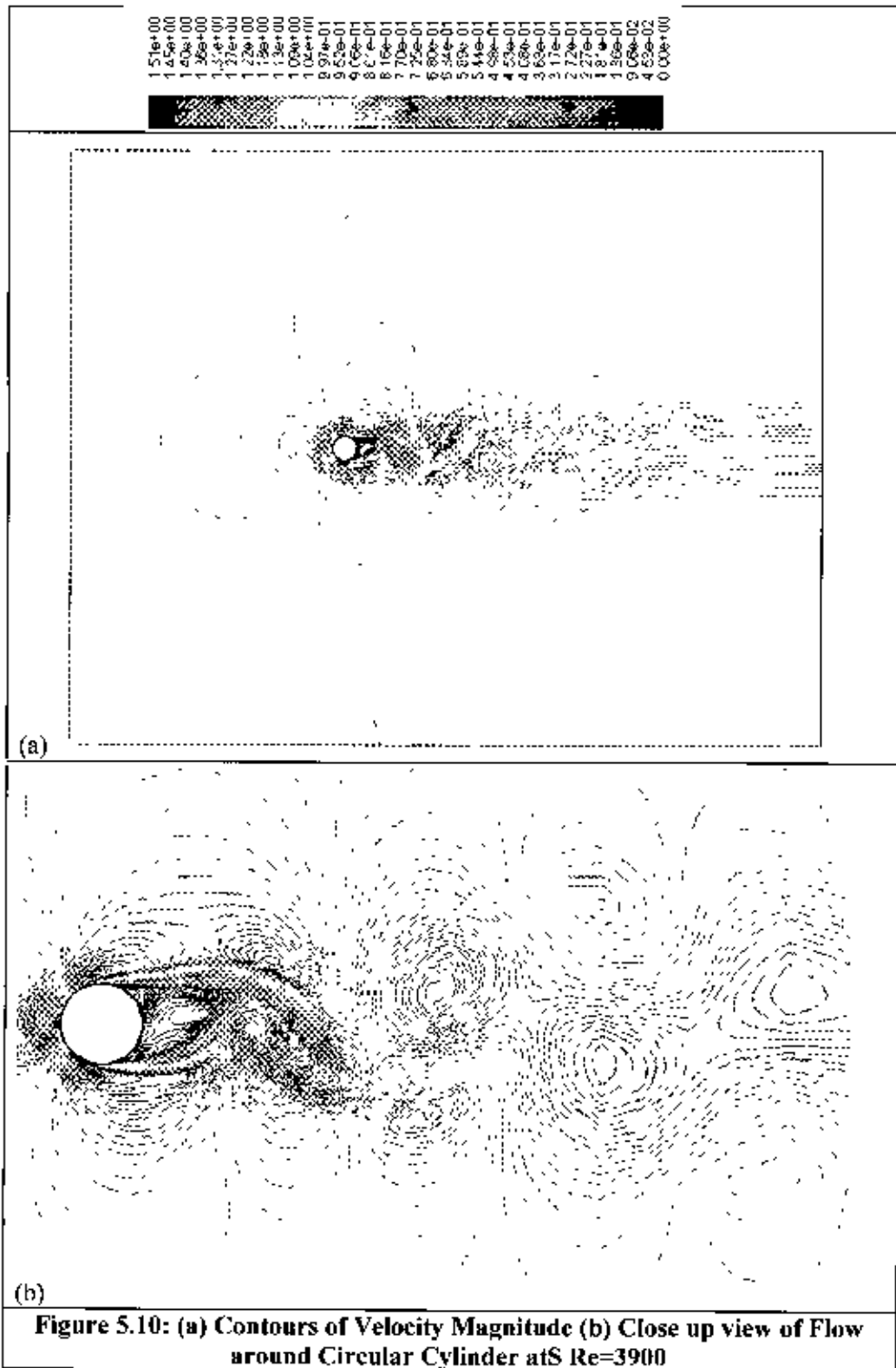


The alternating vortex shedding clearly observed in these figures. Figure 5.10 shows the contours of velocity magnitude around circular cylinder at $Re = 3900$. Figure 5.11 shows the stream function & Figure 5.12 vorticity magnitude during one cycle of lift coefficient at $Re = 3900$.

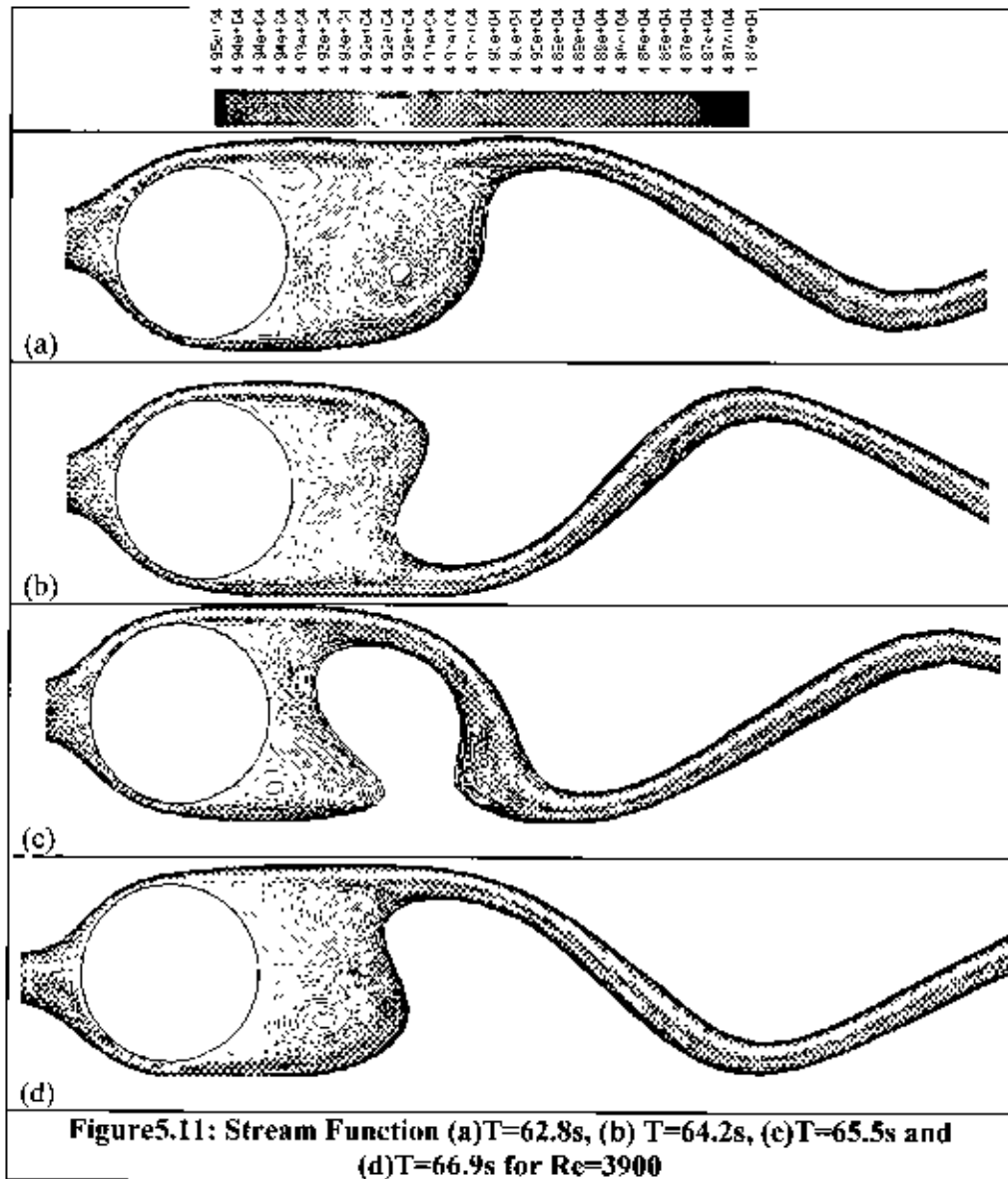
The alternating formation, convection and diffusion of the vortices are clearly shown again. The results in this section show that the vortex shedding is an intrinsic







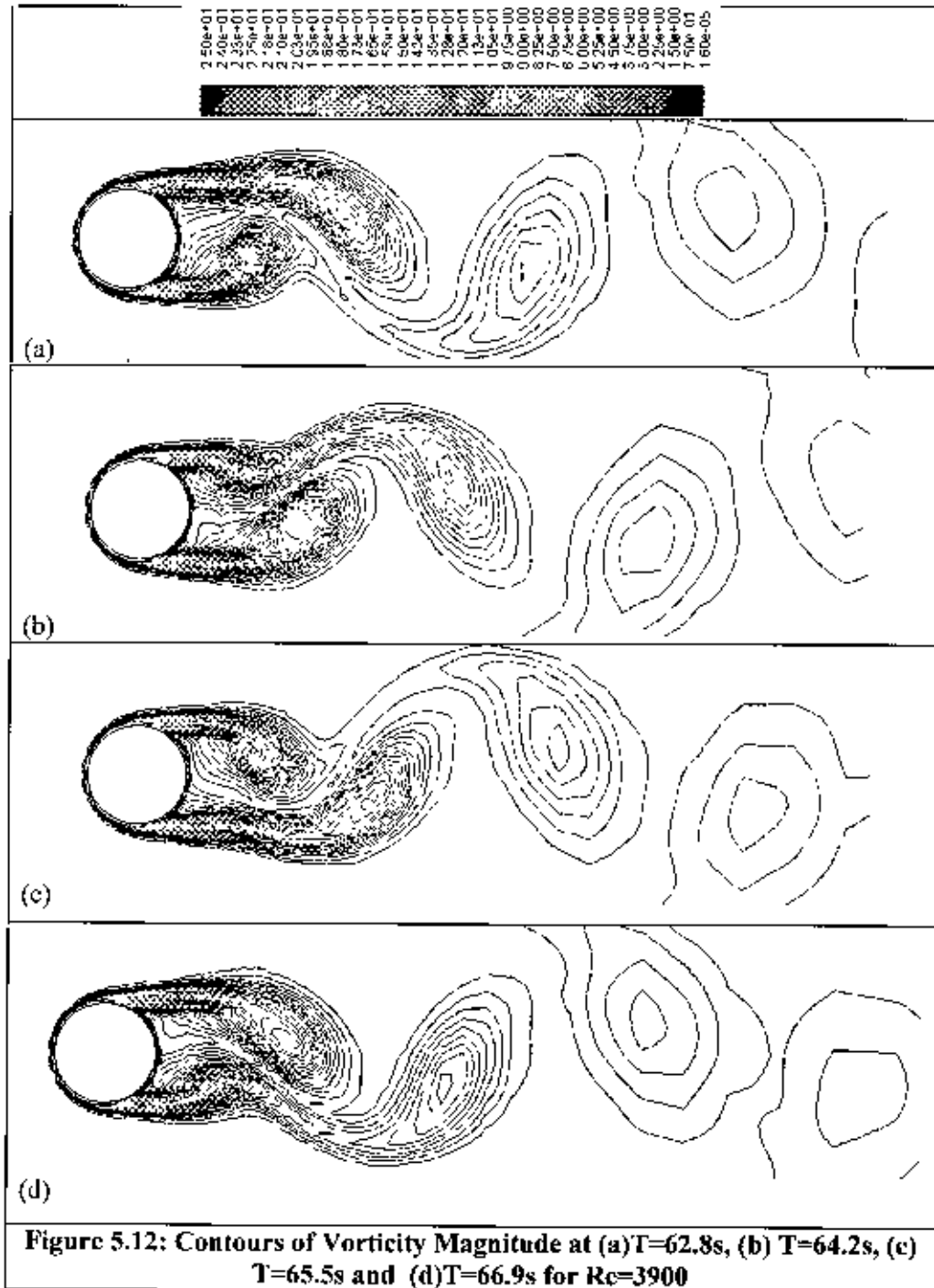
phenomenon of the flow, well predicted by the solution of the Navier- Stokes equations. The vortex shedding is generated by a loss of symmetry of the two dimensional symmetric structures in the wake of the circular cylinder.



5.2.3 Forces on the cylinder

The drag force is a result of the convective motion of the cylinder through the fluid. Because of this motion and of the no-slip condition of the wall, a tangential velocity gradient is created in the direction normal to the wall. The mean value of the drag coefficient calculated by the present method for different Reynolds numbers is very

close to the experimental results of Tritton (1959) and Anderson (2005). The total drag consist of two components: the pressure force (C_p) and the viscous force (C_f) calculated by Equations (5.1-3).



For $Re = 100$, the mean value of the pressure drag, C_p is 0.917, which corresponds to 75% of the total drag. This value is closer to the experimental result (0.995) of Roshko (1954) than that (1.02) of Braza *et al.*(1986). In this case, the lift force is zero as it considered only the vertical component of force.

Figure 5.11 shows the distribution of the wall vorticity (Equation 5.6) with respect to angular positions and the comparison with the numerical results of Braza *et al.*(1986) for $Re = 20, 40$ & 100 . The computed results are in good agreement with those of Braza. In Figure 5.12, the distribution of wall pressure at $Re = 20, 40$ and 100 are compared with numerical results of Braza *et al.*(1986). The predicted wall pressure by this method agrees well with the results computed by Braza *et al.*(1986). Numerical values of the components of total drag coefficient are shown in Table 5.1.

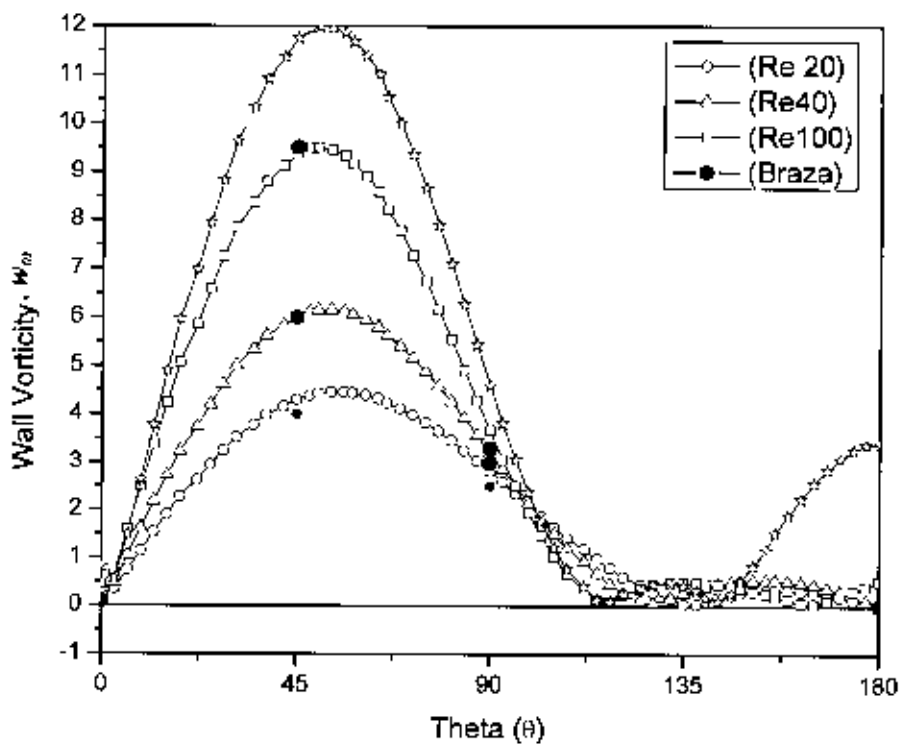


Figure 5.13: Wall Vorticity Vs Angular Position

The drag coefficients of the turbulent flow at $Re = 1000$ & 3900 have also been calculated using three turbulence models. The predicted C_D values by standard k-

epsilon model are quite closely to the experimental values shown in Table 5.2. It is observed that, for the visualization of vortex shedding the Realizable $k-\epsilon$ turbulence model is more effective, as this model captures the separating flow better than standard $k-\epsilon$ model.

Table 5.1: Components of Total Drag Coefficient

Re	Pressure Coefficient	Viscous coefficient	Total Drag Coefficient
100	0.917	0.329	1.245
1000	0.876	0.119	0.995
3900	0.877	0.12	0.997

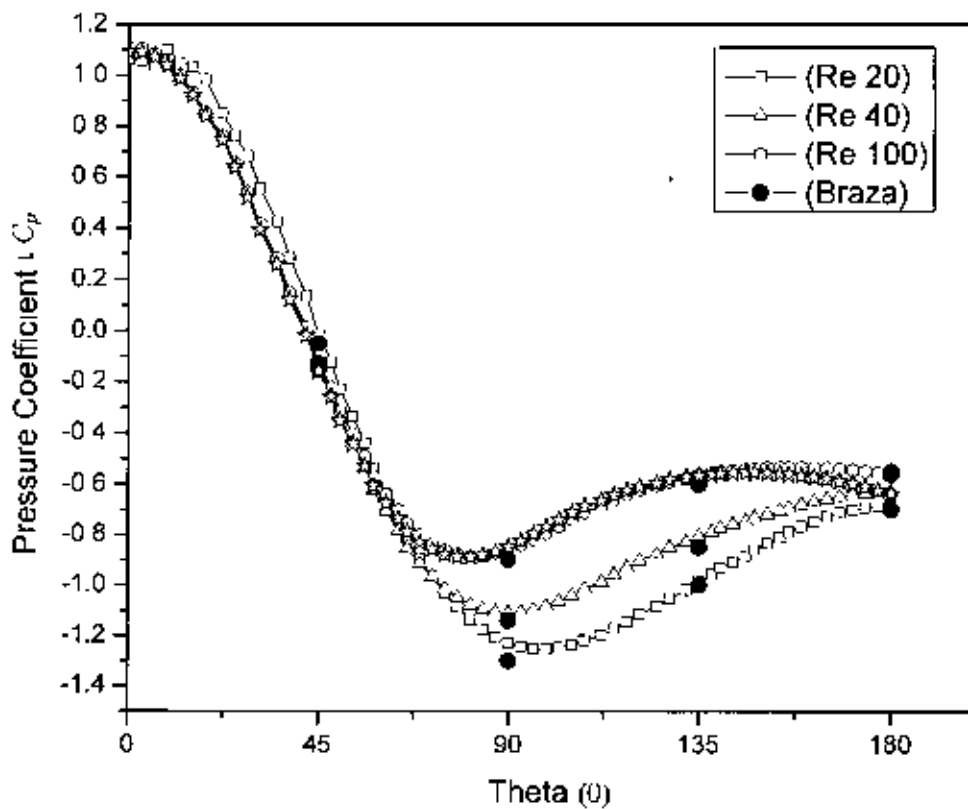
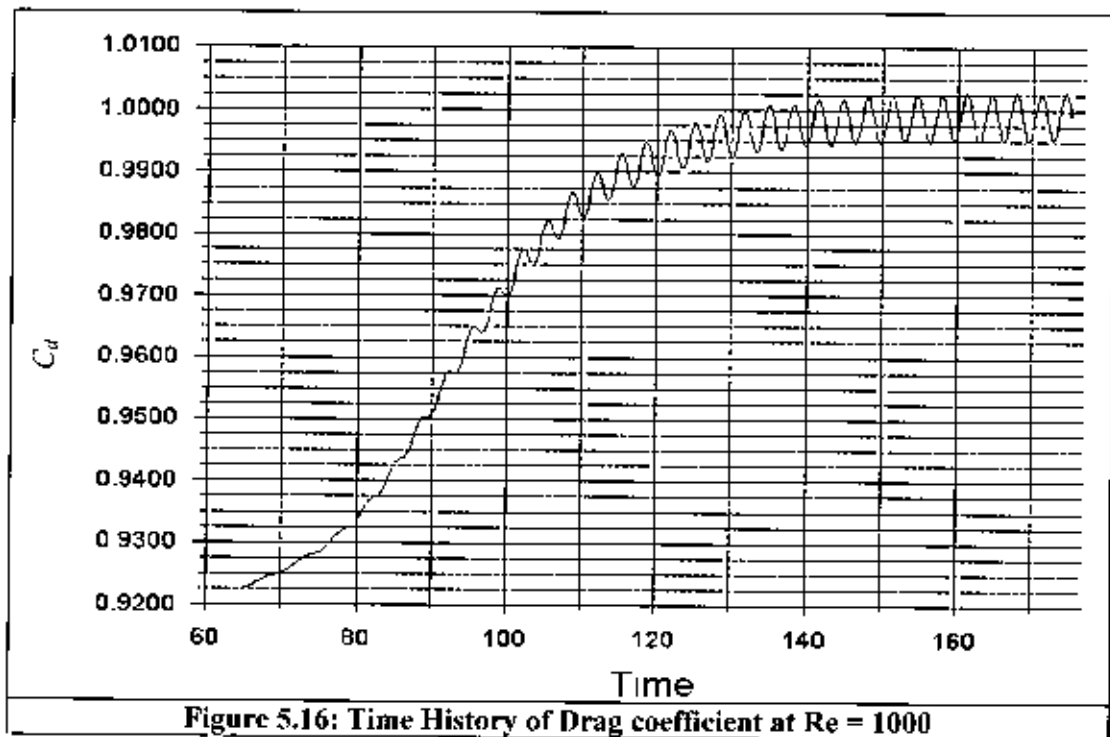
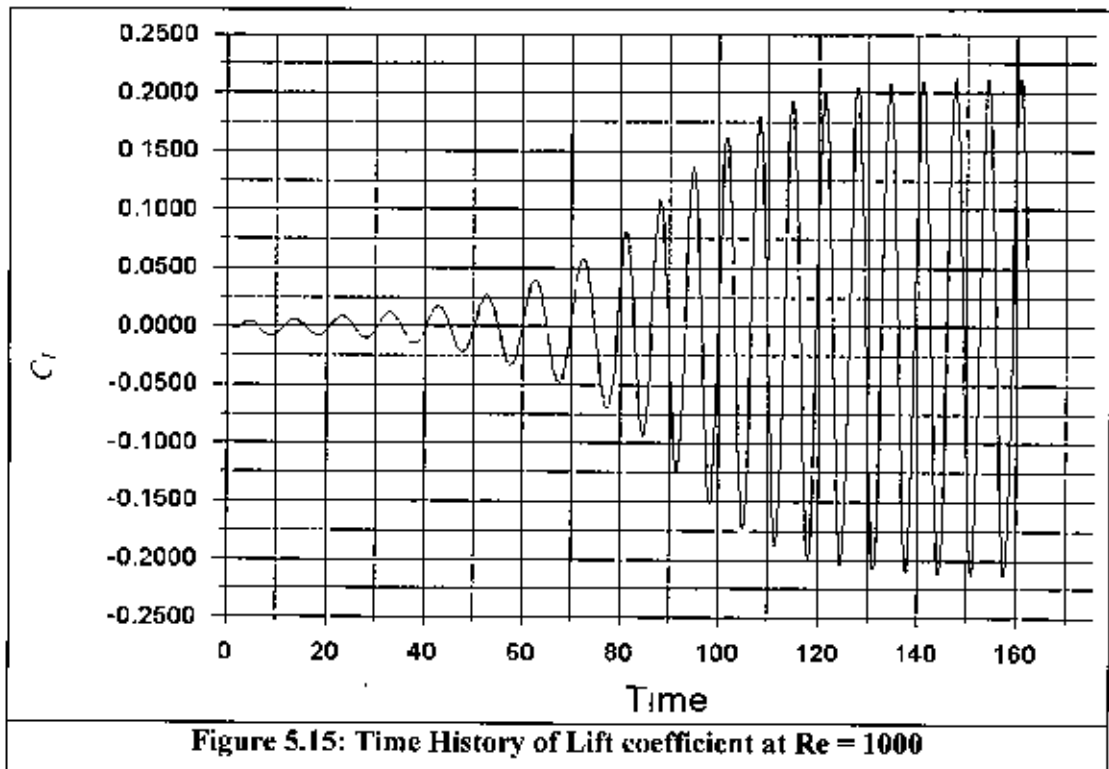


Figure 5.14: Pressure Coefficient Vs Angular Position

On the other hand, the SST $k-\omega$ model is much more recommendable for high Reynolds numbers. The global periodic character of the flow is found to be essentially the same as the Reynolds number increases. For the Reynolds numbers of 1000 and 3900 it should

be recalled that the unsteady lift and drag coefficient oscillates periodically. Figure 5.15 and Figure 5.16 show the lift and drag coefficient for $Re=1000$ respectively.



The drag coefficients as a function of different Reynolds numbers are compared with experimental and other numerical results in Figure 5.17 and in Table 5.2. In most of the cases, the computed results show better agreement with experimental data compared to other predicted values.

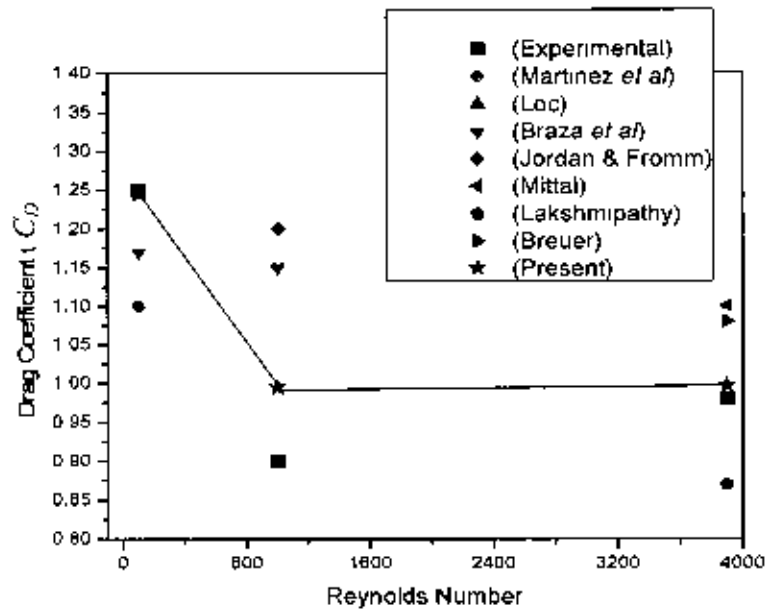


Figure 5.17: Drag Coefficient Vs Reynolds Number

Table 5.2: Comparison of Drag Coefficient at Different Reynolds Numbers

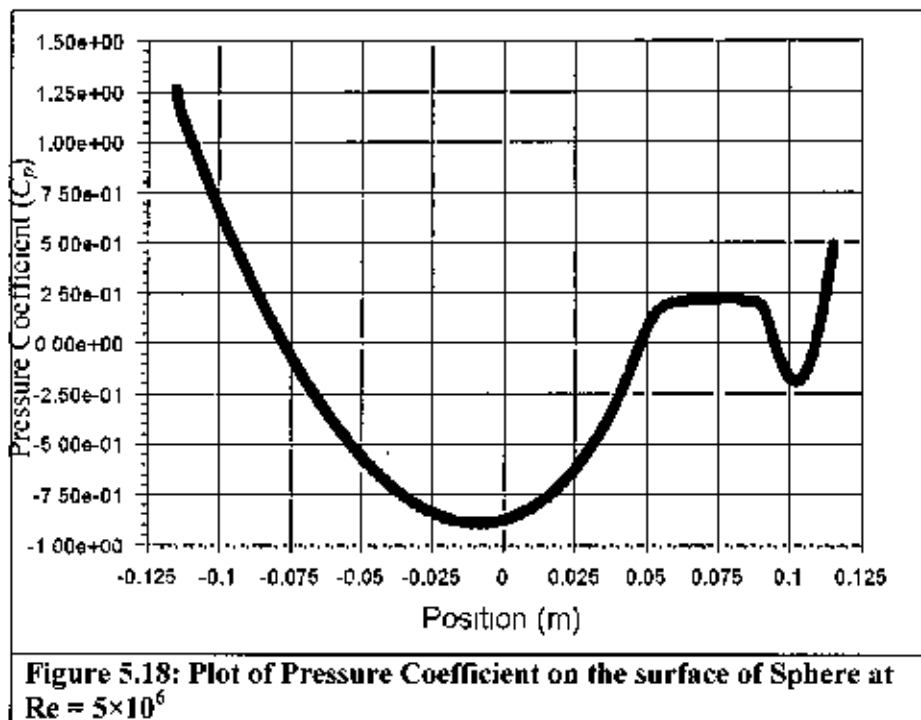
Re	100	1000	3900
Experimental	1.24-1.26 (Tritton, 1959)	0.9 (Anderson, 2005)	0.9817-0.05 (Lourenco & Shih (1993))
Tuann & Olson (1978)	1.25	--	--
Martinez <i>et al</i> (1978)	1.1	--	--
Loc (1980)	1.15	--	--
Braza <i>et al.</i> (1986)	1.17	1.15	--
Jordon & Fromm(1972)	--	1.2	--
Beaudan & Moin (1994)	--	--	1.74
Lakshmi pathy	--	--	0.87
Breuer (1998)	--	--	1.08
Present	1.245	0.995	0.997

5.3 Flow Around Axisymmetric Body of Revolution

In this part two dimensional axisymmetric model is used to simulate the flow around four under-water axisymmetric bodies such as, sphere, DREA submarine bare hull, pod and axisymmetric underwater body based on Gertler's geometry.

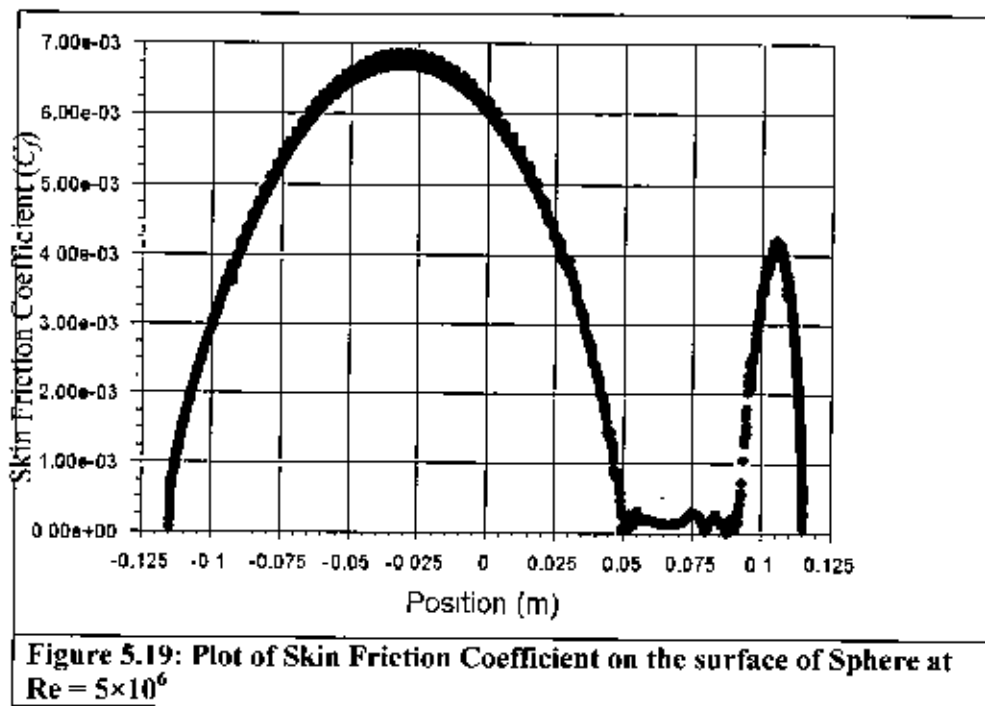
5.3.1 Flow around sphere

In the case of axisymmetric turbulent flow around sphere, the computed results are compared to Achenbach's (1972) experimental data for transcritical flow at $Re = 5 \times 10^6$. According to the experimental observation of Achenbach's (1972) the flow around sphere can be classified into four regions depending on the Reynolds number. In the subcritical region ($Re < 3 \times 10^5$) the drag coefficient is namely independent of Reynolds number. The critical region ($3 \times 10^5 < Re < 4 \times 10^5$) is characterized by a rapid drop of the drag coefficient. The minimum being reached at the critical $Re = 3.7 \times 10^5$, with further increase in Reynolds number. C_D slightly increases again which is known as supercritical flow ($4 \times 10^5 < Re < 2 \times 10^6$) and it seems that the curve is going to reach another maximum. The transition from supercritical to transcritical ($Re > 2 \times 10^6$) is rather floating.



Achenbach's experiment is performed at a transcritical Reynolds number where the flow is considered fully turbulent and thus can be directly compared to the turbulent computational models. In the present study, the turbulent flow simulated using Spalart-Allmaras (S-A) and shear stress transport $k-\omega$ turbulence model at $Re = 5 \times 10^6$.

The predicted pressure coefficient over the surface of the sphere is compared with Achenbach's experimental data in Figure 5.18. The computed results are very close to the experimental ones. Figure 5.19 shows the comparison between computed values of skin friction coefficient over the sphere and Achenbach's experimental results. In this case, the computed skin friction coefficient curves does not track well with Achenbach's data forward of the separation point. However, the general trends of the curves are the same. The accuracy of skin friction coefficient prediction in numerical simulations is highly dependent on the accurate resolution of the turbulent boundary layer near the surface of the body. Accurate calculation of near-wall effects requires an extremely fine mesh in that region. Since boundary layer separation arises due to pressure variations, accurate separation point predictions are dependent on accurate pressure calculations, which require a less fine mesh than skin friction calculations.



However, the discrepancies between actual and computed C_f curves are not expected to greatly affect the reliability of the total drag prediction since skin friction drag accounts only for 10 to 20 percent of the total drag in this case.

Figure 5.20(a) shows the velocity vectors around sphere. The separated region and vortex shedding are clearly visible in the close up view near wall as shown in Figure 5.20(b). Table 5.3 shows the angular position of separation points as well as the percentage of difference (calculated by Equation 5.7) from experimental values. The numerical predictions of separation point matched Achenbach's experimental data well.

Table 5.3: Angle of Separation for Axisymmetric Turbulent Flow around Sphere

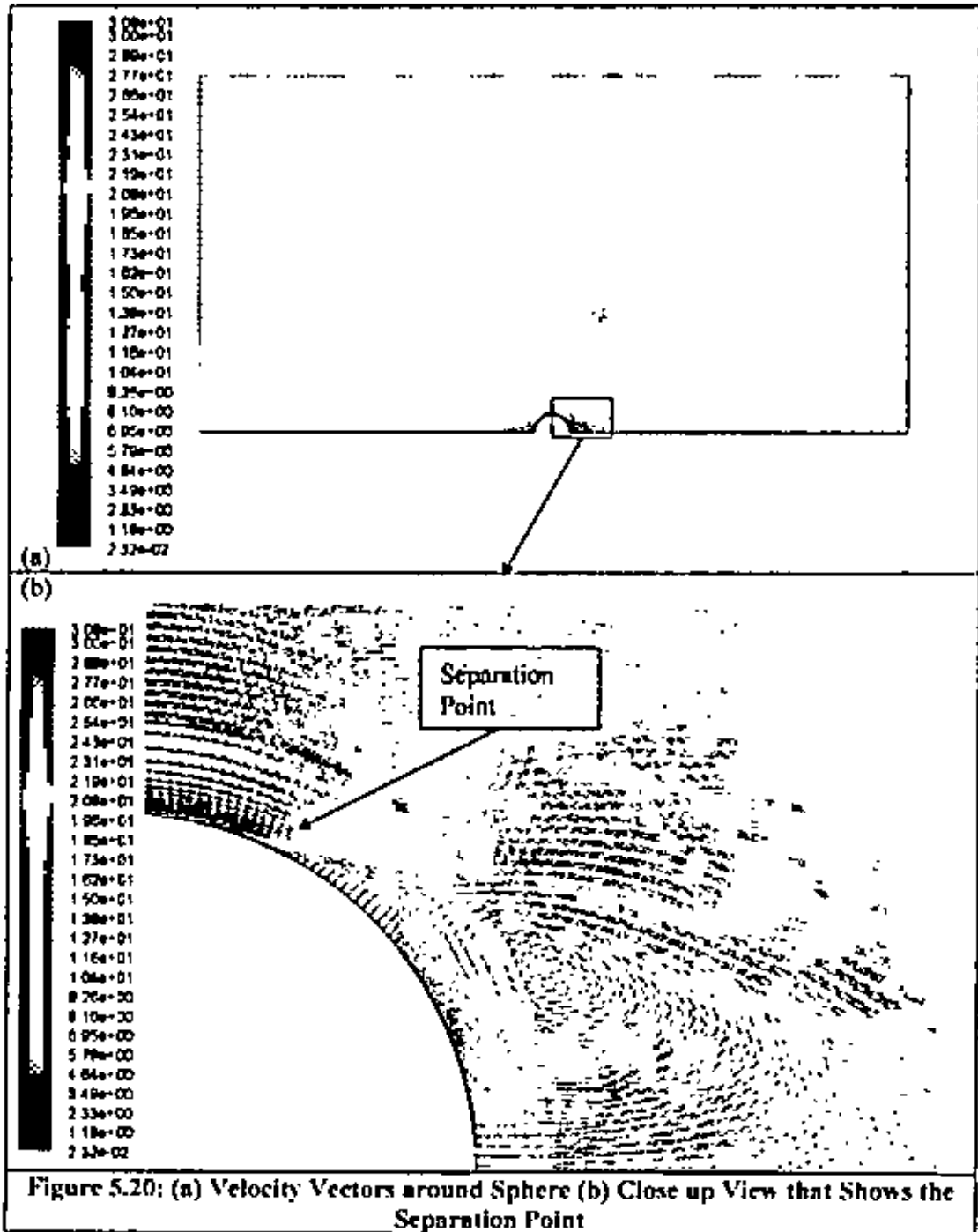
	Separation points (in degrees)	Percent difference
Present	126	6.8 %
Achenbach's (1972) exp. result	118	

Table 5.4 shows values of drag coefficient predicted by two turbulence models and also experimental values measured by Achenbach. Percentage of difference (calculated by Equation 5.7) between the numerical and experimental values are also included.

Table 5.4: Drag Coefficient for Axisymmetric Turbulent Flow around Sphere

	Spalart-Allmaras Turbulent model	SST $k-\omega$ model	Achenbach's exp. (C_D)
Drag coefficient, C_D	0.163	0.154	0.18
Percent difference	9 %	14 %	

Achenbach measured drag coefficients from 0.09 to 0.18 as Reynolds number varied from 4×10^5 to 5×10^6 . This implies that drag is Reynolds number-dependent in the supercritical to transcritical range, and that the small discrepancy between Achenbach's drag coefficient and the numerically computed drag coefficient may be due to Reynolds number mismatch more than inaccuracies in the numerical method. Achenbach also presents other drag coefficient results in his paper that are obtained through integration



rather than direct measurement; those results predict an even larger range of drag coefficient variation (from 0.07 to 0.24 within the same Re range). Further, the pressure coefficient plot shows that more pressure recovery occurred on the aft region of the sphere using two turbulence models than that occurred on Achenbach's measurement. The higher pressure recovery of the numerical models explains the reduced drag coefficients prediction compared to Achenbach's result.

5.3.2 Flow around DREA submarine bare hull

One of the greatest advantages of CFD over experimentation is the ease and availability of flow visualization. This section shows some of the more relevant flow parameters. Generally, with a reasonable grid and a reasonable level of convergence, the results obtained from these simulations will not look much different from one that is fully converged and deemed mesh insensitive. Moreover, it is ensured that the computational domain and the grid number of the following cases is sufficient enough to compute the drag forces and the flow visualizations.

Here, turbulent flow is simulated past axisymmetric underwater vehicle hull form. The submerged body used in this research is a standard DREA (Defence Research Establishment Atlantic) bare submarine hull as shown in Figure 4.4. Shear Stress Transport (SST) $k-\omega$ model is used for capturing turbulent flow. For comparison of the computed result with experimental value, the flow is simulated at $Re = 23003039$ (23 million). A numerical investigation for estimating drag force on submarine hull has also been done using CFX by Baker (2004). The computed result with the experimental and Baker's numerical result is shown in Table 5.5.

Table 5.5: Drag coefficient with it's components for DREA submarine bare hull

Pressure Coefficient (C_p)	Frictional Coefficient (C_f)	Drag Coefficient(C_D)	Experimental value (C_D)	Baker's CFX result (C_D)
0.000213	0.000827	0.00104	0.00123 (± 0.000314)	0.00167

The above table shows that the present result is more accurate than that of Baker's. The difference between the computed and the experimental result is 15% where as it is 33% for Baker's CFX result (the percentage of difference is calculated using Equation 5.7).

Another remarkable matter observed in Table 5.5 is that, in case of submarine hull the frictional coefficient dominates the pressure drag coefficient but the opposite phenomenon occurs in case of sphere. Here the frictional coefficient is 79.5% of the total drag coefficient, whereas it is only 10% in case of sphere. This is expected because the DREA submarine hull is a long body having a large length-diameter ratio. In this

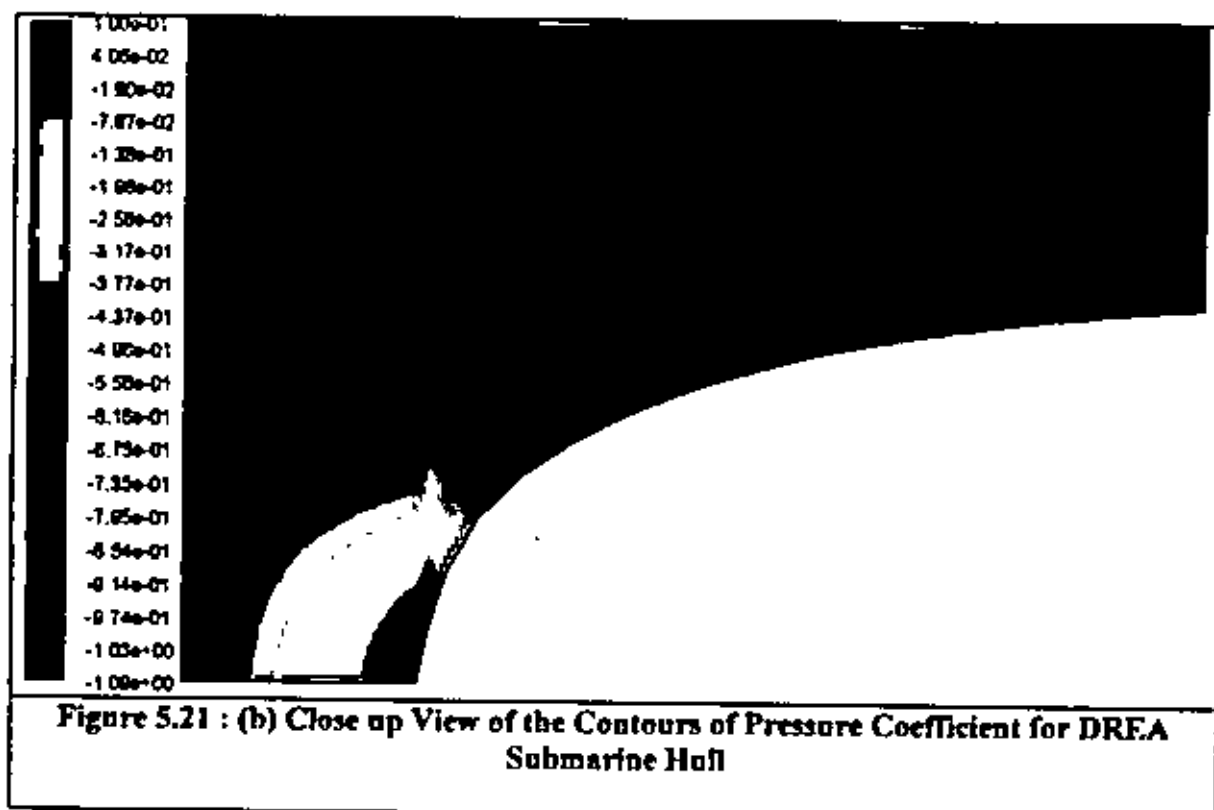
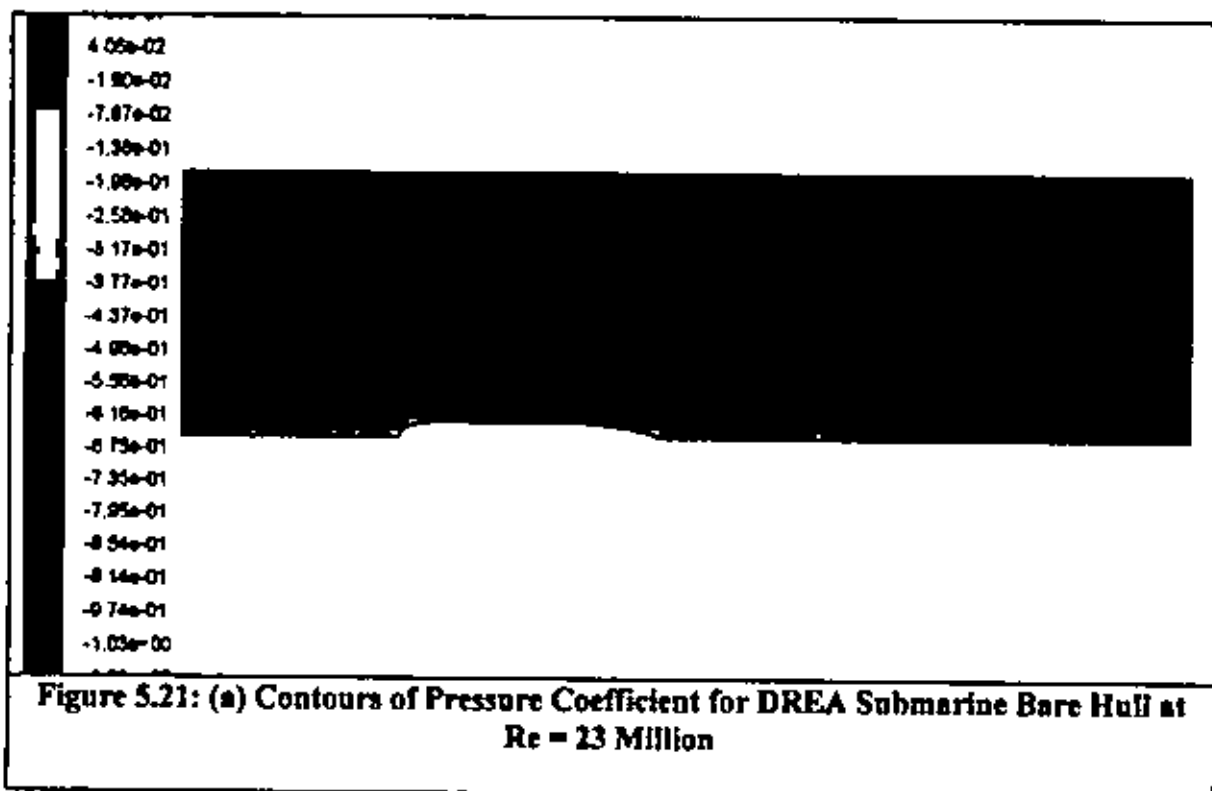
case, the arbitrary area L^2 is used to be consistent with experimental data from the wind tunnel test. (Department of Research and Development Canada -1988)

Figures 5.21-24 show the different flow visualization over the submarine. As axisymmetric model is used in this study, all of the figures show only half section of the body.

The contour of the pressure coefficient around the submarine hull is shown in Figure 5.21(a) at $Re = 23$ million (velocity of 3.422 m/s). The stagnation point of high pressure at the front tip of the hull, the favorable pressure gradient at the front section and the adverse pressure gradient at the rear section of the hull are clearly shown. Since the reference pressure is set to zero the pressures shown are relative. Figure 5.21 (b) shows a close up of the front section of the hull. Here the stagnation point and the favorable pressure gradient are even more visible (red color).

Figure 5.22(a) shows the contour of velocity magnitude for the submarine hull at $Re = 23$ million. When compared to the pressure plot it can be seen that the stagnation point of high pressure corresponds to the low velocity point at the front, the favorable pressure gradient in the front section corresponds to a high velocity and the adverse pressure gradient at the rear corresponds to a lower velocity. Figure 5.22(b) shows a close up view of the front section of the velocity profile. Here it is apparent by the colors close to the shape that the no slip boundary condition set for the surface of the hull is in effect. It is also more apparent that the stagnation point is actually a stagnation point with zero velocity (the blue region).

The wall shear plots are a good indication of the viscous drag over the hull surface. They can also be used to check if there is any separation because the wall shear goes to zero where the boundary layer separates. Viscous effect occurred only on the boundary surface of the body shown in Figure 5.23(a). It shows a large wall shear affect in the favorable pressure gradient area at the front section of the hull. The very peak of the front section has a reduced wall shear, which makes sense physically because there is a reduced flow velocity in this region due to the stagnation point. This illustrates how this region largely affects the viscous losses (blue color). This figure also shows the boundary surface region closer, which indicates a high shear stress (red color).



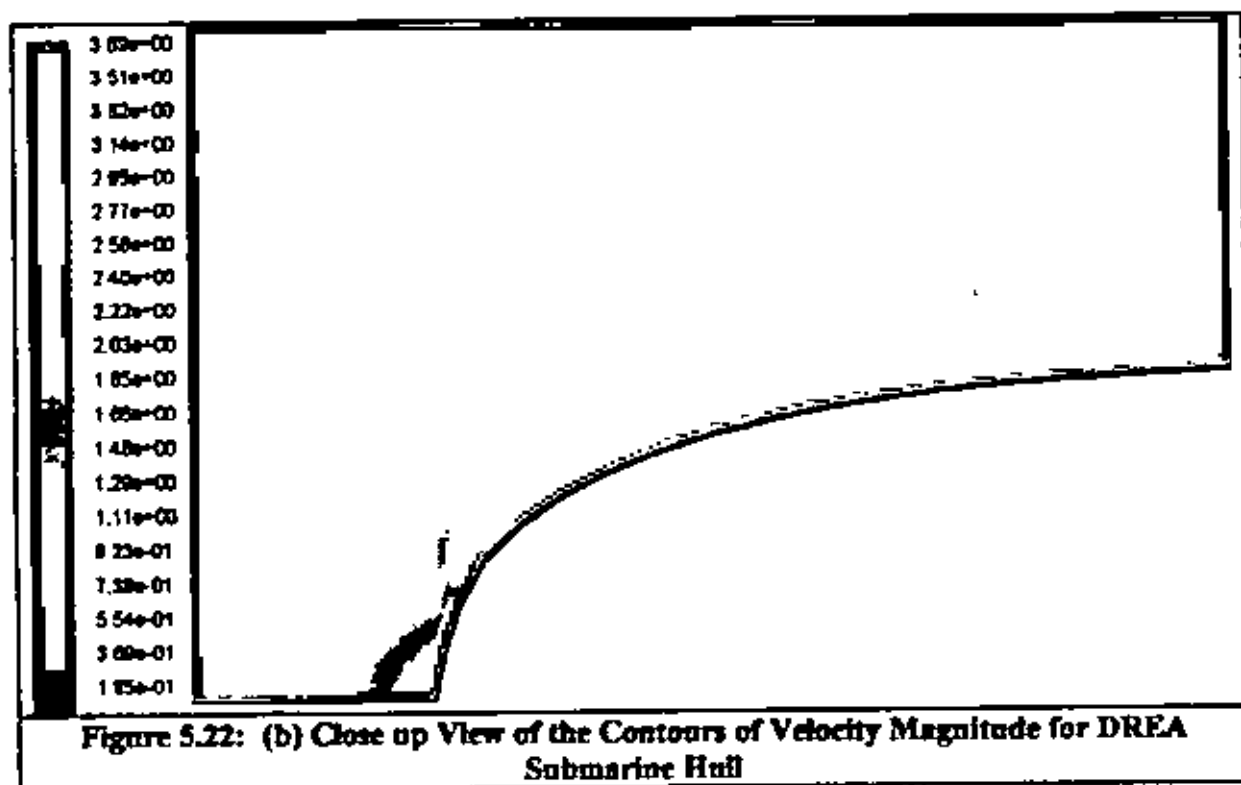
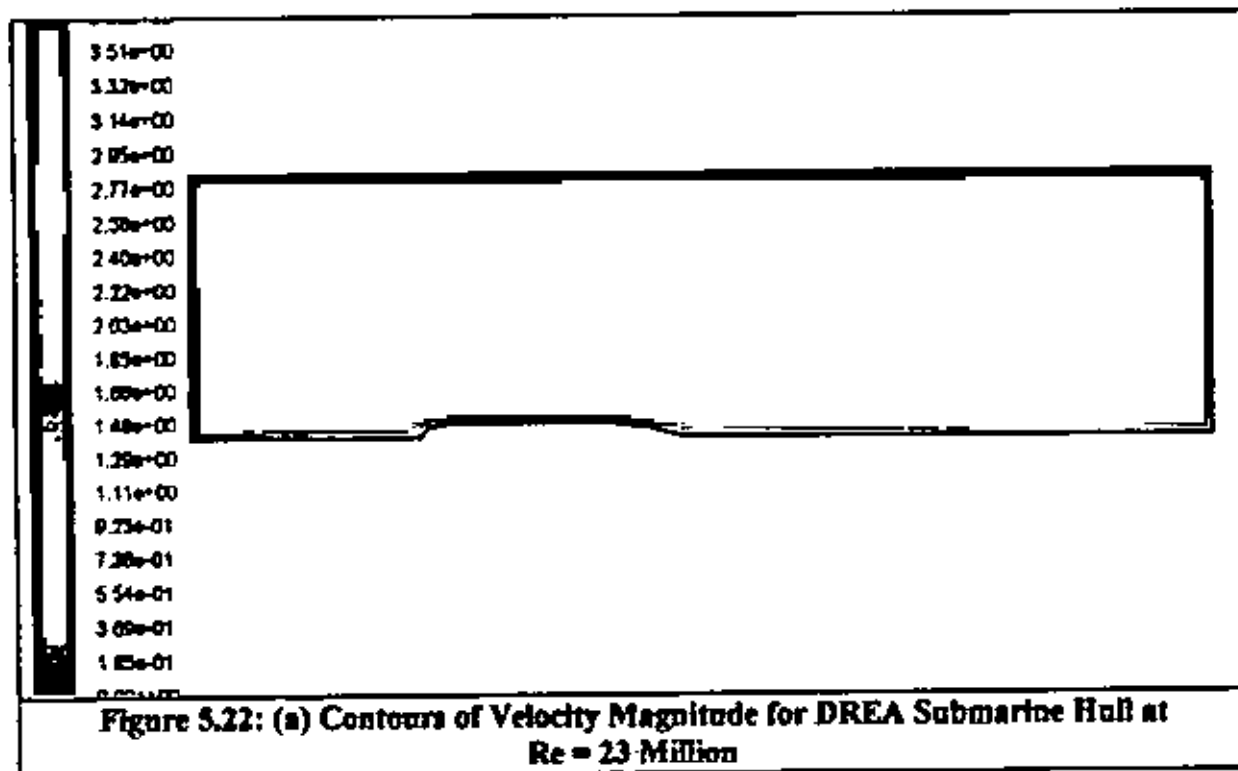




Figure 5.23: (a) Contours of Wall Shear Stress for DREA Submarine Hull at $Re = 23$ Million

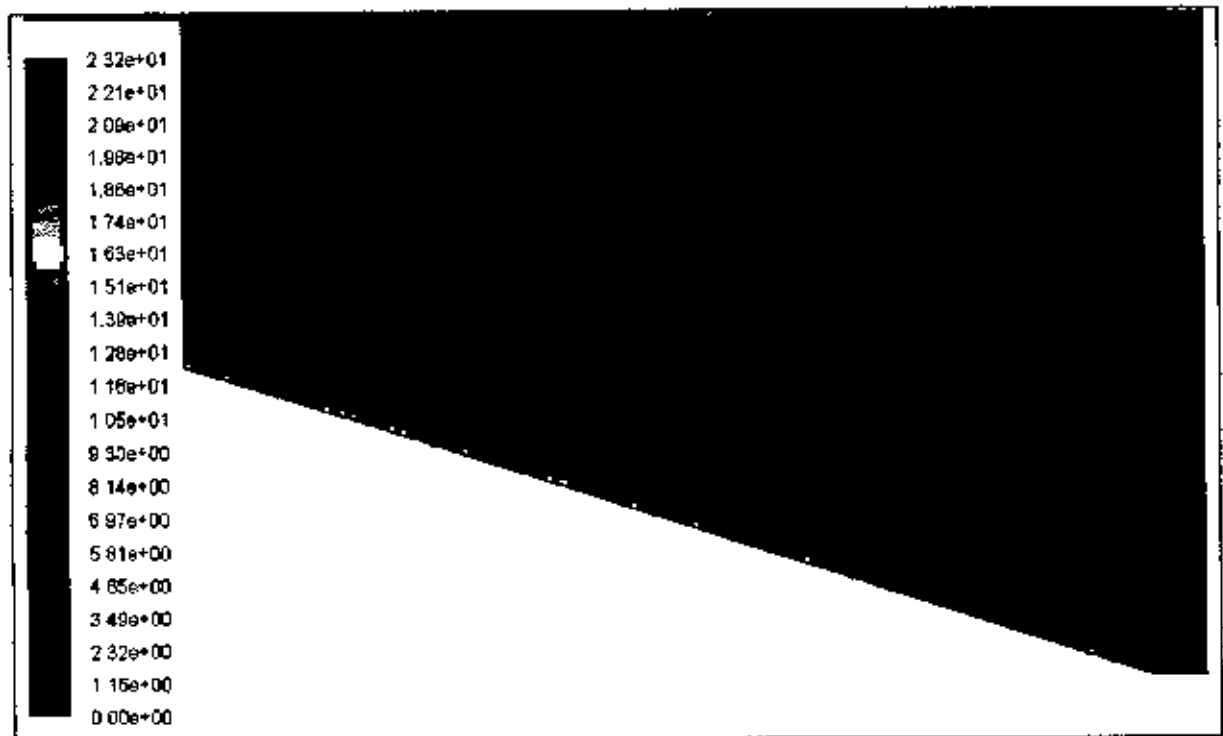


Figure 5.23: (b) Close up View of the Rear Section of Contours of Wall Shear Stress for DREA Submarine Hull

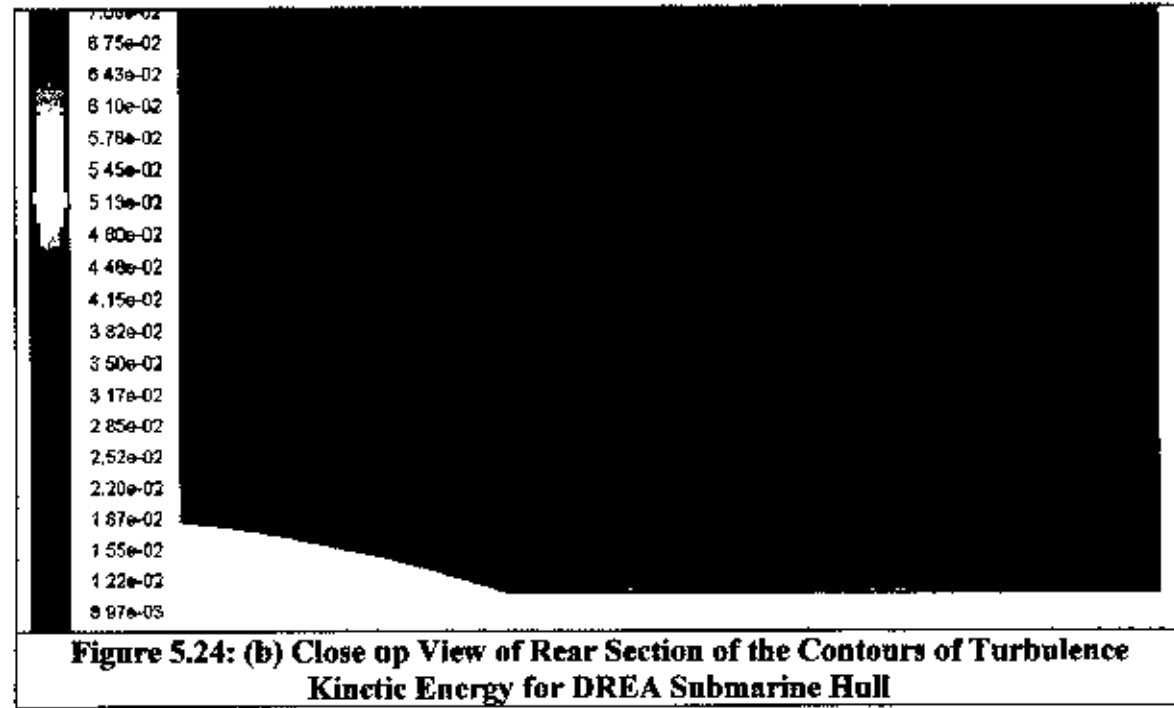
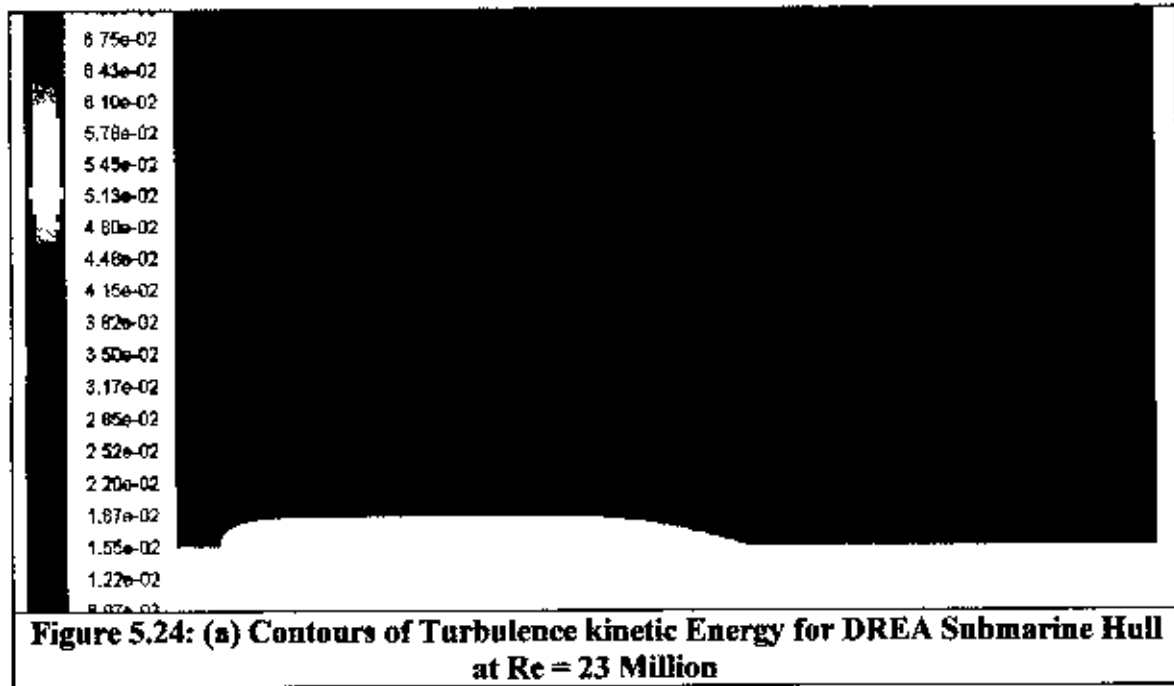


Figure 5.23(b) shows the tail section of the submarine hull. This is where the wall shear plot is beneficial in determining if there is any separation. The wall shear goes nearly to zero but then increases again. This is happened because, in this part of the body the boundary layer may have separated and then reattached, which is a common phenomenon.

Finally, turbulence kinetic energy is related to the turbulence model used in this simulation. Turbulence originates from the boundaries of a domain, so in this case the only place for turbulence to be generated is from the body, since it is the only region with a no slip condition. Turbulence kinetic energy is a measure of the energy built up as turbulence. In Figure 5.24(a) the kinetic energy is shown to build up as flow passes along the hull and then propagate from the rear. Figure 5.24(b) shows a close up view of this turbulent energy being dissipated to the free stream.

5.3.3 Flow around axisymmetric pod

Podded propulsion systems are becoming increasingly popular in modern commercial marine vessels on account of the increase of their efficiency. The study of flow around pod is of increasing importance due to extensive use of podded propulsors.

Table 5.6: Run parameters for Axisymmetric Viscous Model

Solver	2DDP
Model	SST $k-\omega$
Density	1000
Viscosity	0.001
Inflow	$u=1, v=0$
Reynolds Number	3×10^6
Turbulence Kinetic Energy, k	9.227×10^{-3}
Specific Dissipation Rate, ω	0.2641
C_μ	0.09
Turbulence Length, l	0.21

In this study, only the pod (without strut) is considered. The geometry of the pod is discussed in Section 4.3.1.2. Though, the shape of the pod body is more or less similar to submarine hull discussed in the previous section, the concentration is given here on the investigation of force acting on the body instead of flow visualization. The shear stress transport (SST) $k-\omega$ model is used to simulate the turbulent flow at $Re = 3 \times 10^6$ on the axisymmetric pod geometry. The parameters used for the axisymmetric flow solver are given in Table 5.6.

The grid generation is (discussed in section 4.3.1.2) ensured the optimal result of calculating drag force on pod body. The time step size is selected so that the maximum cell Courant number is very near to unity. In Figure 5.25, the result of C_D versus time shows the convergence of the solution. The minimum spacing is generally based on Y^+ (discussed in section 3.3.3), a dimensionless parameter representing a local Reynolds number in the near wall region. It is important for the near wall treatment for turbulent flow. Figure 5.26 shows the maximum value of $Y^+ = 25$ obtained using SST $k-\omega$ model, which is acceptable when disabling transient flow. Surface pressure coefficient, frictional coefficient and overall volumetric drag coefficients are important quantities for assessing the hydrodynamic efficiency of podded propulsor system. The main focus of this study is to calculate these forces. The computed total drag coefficient with its component at $Re = 3 \times 10^6$ is given in Table 5.7.

Table 5.7: Total Drag Coefficient with its Component at $Re = 3 \times 10^6$ Computed on Pod Hull

pressure coefficient (C_p)	frictional coefficient (C_f)	drag coefficient (C_D)
2.199×10^{-1}	3.89×10^{-3}	6.09×10^{-3}

From this table, it is observed that, in case of pod the frictional coefficient is also the major portion of total drag like submarine hull due to its long body surface. However, in this case, frictional coefficient is 64% of total drag coefficient whereas it is 79.5% in case of submarine. This is happened due to the fact that the pod body has lower L/D ratio (3.6) than submarine body ($L/D=8.75$). Small difference in shape at the nose and tail section of the bodies may also be responsible for this.

Surface area is one of the important parameters for calculation of skin friction coefficient. In this case, following formula is used to calculate the pod surface area.

$$Area = \sum_i \left(\sqrt{(R_{i-1} - R_i)^2 + (x_{i-1} - x_i)^2} \times (R_{i+1} + R_i) \times \pi \right) \quad (5.1)$$

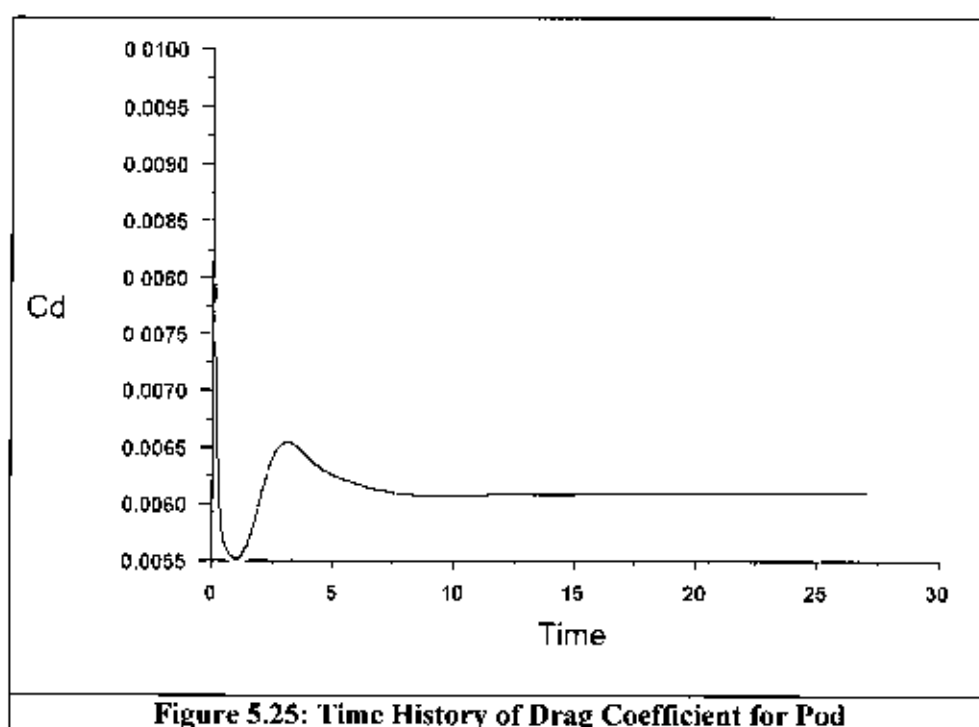
Where, R_i are the radii at corresponding axial location x_i .

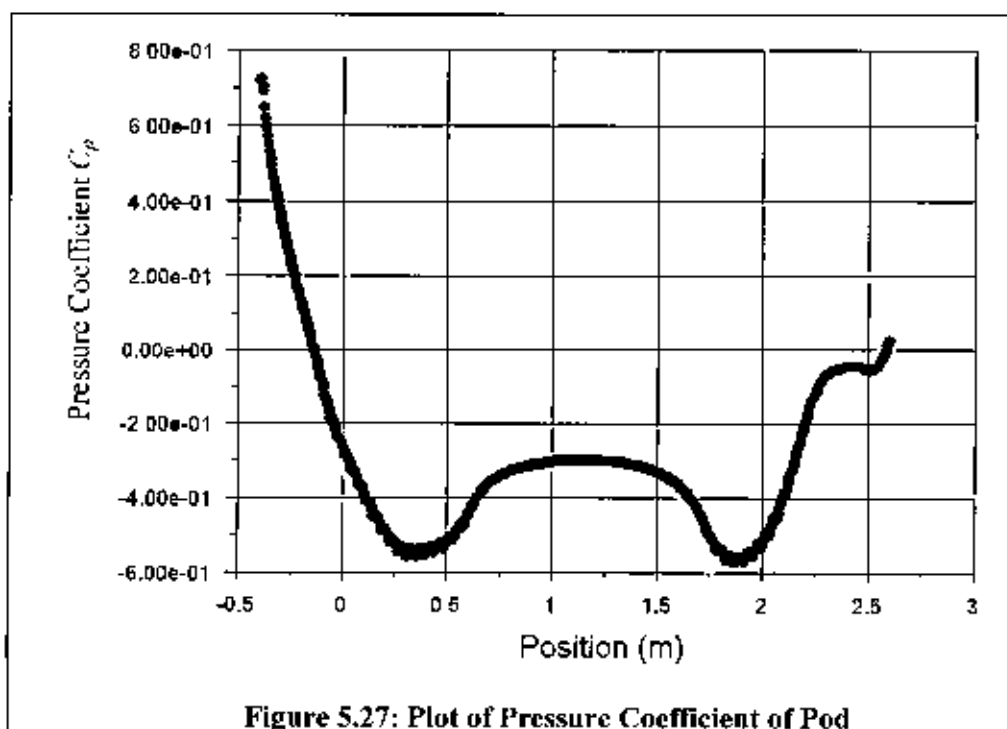
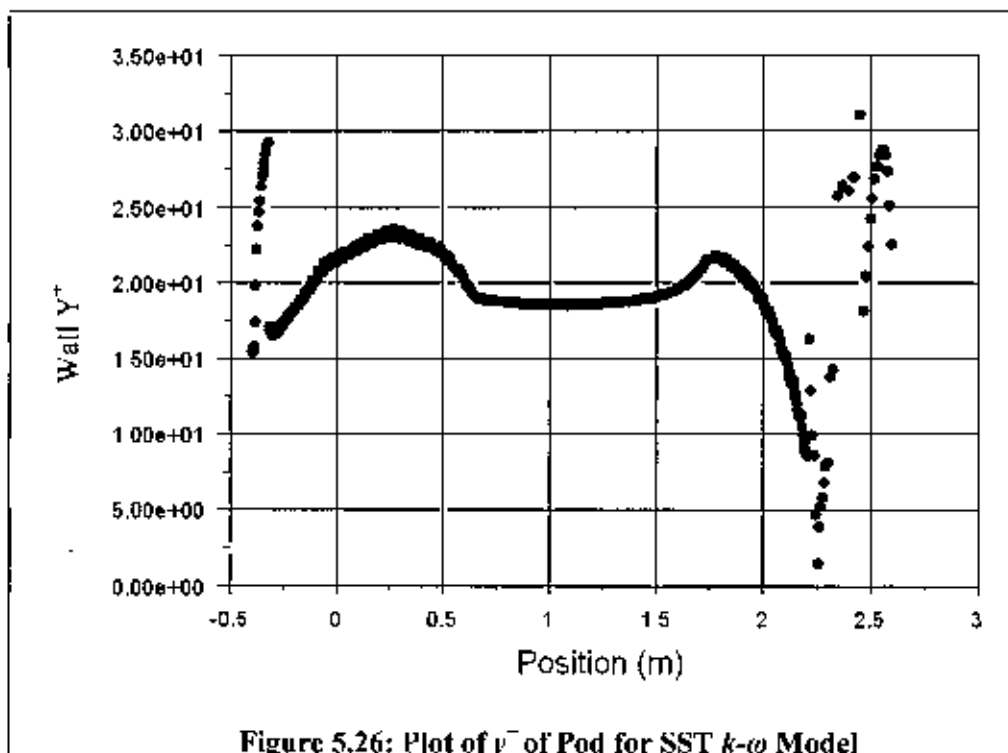
Table 5.8 shows the comparison of the computed frictional coefficient with results of Gupta (2004) and Blasius (1908). It is observed from the above table that the computed result shows better agreement than that of Gupta.

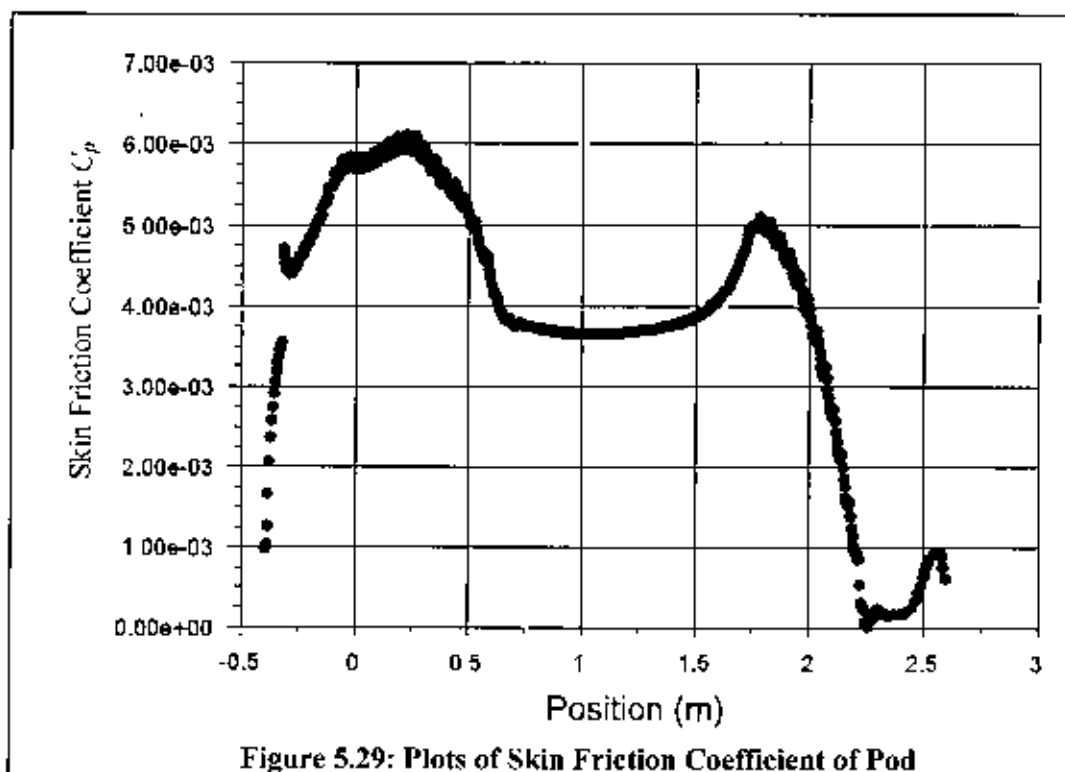
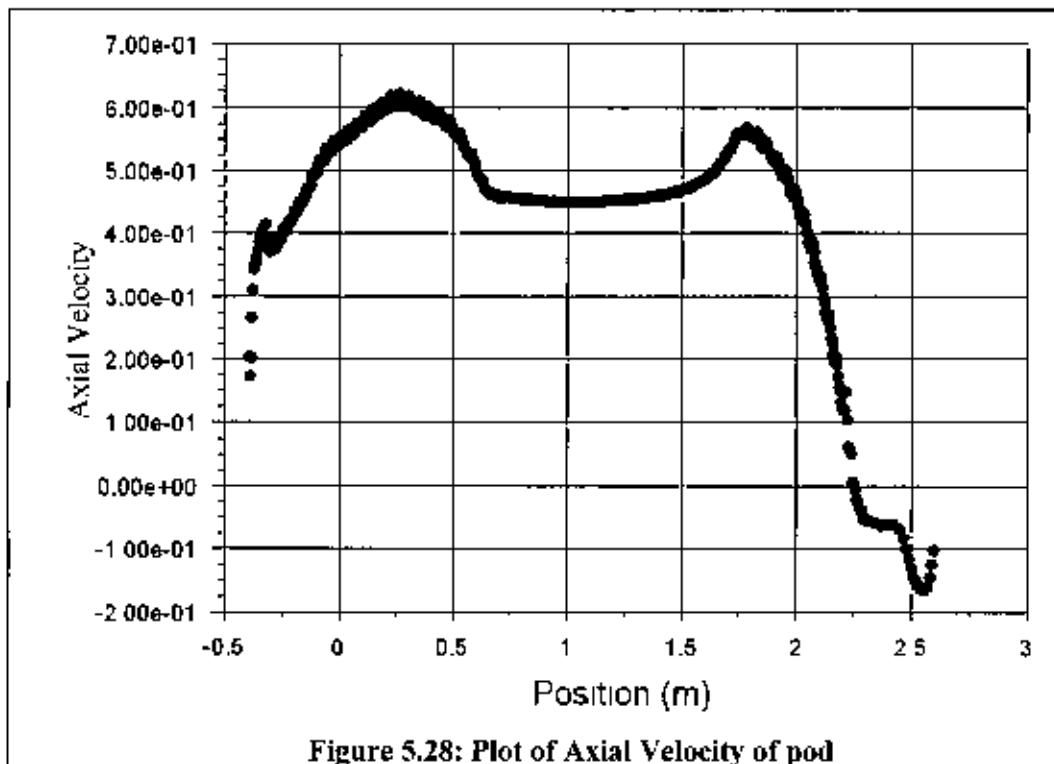
Table 5.8: The Frictional Coefficient of Pod

Present Result (C_f)	Gupta's result (C_f) (Calculated by RSM model)	Blasius theoretical result (C_f)
3.89×10^{-3}	5.0838×10^{-3}	3.207×10^{-3}

Figure 5.27 and Figure 5.28 show the pressure coefficient and axial velocity on the pod respectively and both of them agree well with that of Gupta (2004). In this case, the radial velocity is zero everywhere as the flow is simulated at a zero angle of attack. It is known that the easiest way of calculating the separation point is from its wall shear stress. At the separated point the wall Shear stress become zero. From Figure 5.29 it is observed that the wall shear goes to zero but then increase again. This phenomenon demonstrates that boundary layer may have separated and then reattached.







5.3.4 Flow around underwater vehicle hull based on Gertler's geometry

The focus of this study is to examine the drag force on seven bodies with length-to-diameter ratios (L/D) ranging from four to ten. Each body is defined by a sixth-degree polynomial based on Gertler (1950. Systematic model test for streamlined axisymmetric bodies performed in the David Taylor Model Basin in Washington, Gertler (1950) gave some guidelines for design of deeply submerged bodies. Axisymmetric model is used as it is an ideal candidate for a parametric study with their easily defined geometry, straightforward grid generation, and available experimental data. It is ensured that total number of grid points, location of outer computational boundaries, and minimum spacing (initial spacing normal to body surface) (discussed section 4.3.1.4) are sufficient enough for the prediction of drag force on the body. It is also seen that extending the outer boundary has a lesser effect on the result.

In this study, the investigation of turbulent flow is confined only to zero degree angle, as a non-zero angle of attack is beyond the capacity of axisymmetric model. Different turbulent models are used for the simulation of flow around axisymmetric underwater body based on Gertler's geometry.

Table 5.9: Computed Drag Coefficient using Different Turbulence Model for Axisymmetric Body with $L/D=4$

Turbulence model	Drag coefficient, $C_D(\times 10^{-3})$	Experiment, $C_D(\times 10^{-3})$	% difference
Sparat Allmaras (S-A)	5.50	3.208	71%
$k-\varepsilon$ (standard)	6.0		87%
$k-\varepsilon$ (reliable)	4.23		32%
$k-\omega$ (standard)	6.01		90%
(SST) $k-\omega$	3.435		7.1%

From the computed result it is observed that the shear stress transport (SST) $k-\omega$ turbulence model gives better result for the bodies where skin-friction coefficient

dominates the drag pressure coefficient. Table 5.9 shows the computed drag coefficient and differences from the experimental value using different turbulent modes in case of axisymmetric body with $L/D=4$.

Then the investigation is extended for other bodies with different length-diameter ratio. The calculations and experiments are performed for a Reynold's number of 2×10^7 . Table 5.10 shows the computed drag coefficient using shear stress transport $k-\omega$ turbulence model. It also percentage of difference from experimental results calculated by Equation (5.7). The table shows best performance of the present 2-D axisymmetric SST $k-\omega$ turbulence model compared to other turbulence models.

Table 5.10: Computational versus Experimental Results for Axisymmetric Bodies of Revolution using SST $k-\omega$ Turbulence Model

L/D	Present result ($\times 10^{-3}$)			Experiment ($\times 10^{-3}$)	% difference
	C_p	C_f	C_D	C_D	
4	0.600	2.835	3.435	3.208	7.1%
5	0.410	2.730	3.140	2.988	5.1%
6	0.300	2.720	3.020	2.848	6.0%
7	0.293	2.665	2.958	2.758	7.2%
8	0.209	2.684	2.893	2.718	6.4%
9	0.187	2.635	2.822	-	-
10	0.182	2.633	2.815	2.703	4.1%

From Table 5.10 it is also observed that drag coefficient is decreasing with the increase of length-diameter ratio. In other words, the drag force is inversely proportional to L/D ratio of the body. It happened because the shape of the body is transforming from thick to slender with the increase of L/D as the body length is fixed. The fineness ratio L/D influences substantially the resistance of submarines, since the wetted surface depends strongly on it for a given volume. Therefore reducing the wetted surface reduces the resistance.

It is customary to decompose the resistance of the naked hull of a deeply submerged submarine into skin friction resistance and form resistance. The skin friction resistance is due to the viscous shear of water flowing over the hull. It is essentially related to the length-diameter ratio of the body. For a given volume, a sphere ($L/D=1$) has the smallest

skin friction resistance whereas for a flat plate ($L/D=\infty$) it is the highest. Table 5.11 shows the percentage of skin friction coefficient on drag coefficient for length-diameter ratio from 4 to 10 at $Re = 2 \times 10^7$.

Table 5.11: Skin-friction Coefficient as Percentage of Total Drag Coefficient for $L/D=4-10$

L/D	Frictional coefficient, C_f ($\times 10^{-3}$)	Drag coefficient, C_D ($\times 10^{-3}$)	% of C_f in C_D
4	2.835	3.435	82.5%
5	2.730	3.140	86.9%
6	2.720	3.020	90.1%
7	2.665	2.958	90.1%
8	2.684	2.893	92.7%
9	2.635	2.822	93.4%
10	2.633	2.815	93.5%

Several prediction methods have been investigated to calculate the drag for this series of bodies. Table 5.12 provides a comparison of the current results with the experimental and other three methods; one, based on a differential boundary layer formulation (theory of Cebeci and Smith), another based on a simple drag formula by White (1977) and the other computed numerically using ISFLOW by Lin *et al* (1995). The computed results are in good agreement with the experimental measurements and other results.

Table 5.12: Drag Coefficient ($C_D \times 10^{-3}$) from Different Prediction Methods at $Re = 2 \times 10^7$ for $L/D = 4-10$

L/D	White's formula(1977)	Boundary layer theory	Lin <i>et al.</i> (1995) (ISFLOW)	Present	Experimental
4	3.108	3.028	3.213	3.435	3.208
5	2.998	2.958	2.948	3.140	2.988
6	2.928	2.898	2.858	3.020	2.848
7	2.858	2.858	2.761	2.958	2.758
8	2.808	2.818	2.691	2.893	2.718
9	--	--	--	2.822	--
10	2.738	2.778	2.629	2.815	2.703

It is known that the total drag coefficient (C_D) is composed of pressure coefficient (C_p) and frictional coefficient (C_f) (Table 5.10), which are obtained by integrating the pressure distribution and viscous shear stress, respectively, over the body surface. Figure 5.30 shows the plot of skin frictional coefficient for $L/D = 4-10$ serially. The separation of flow goes away with the increase of length-diameter ratio. Finally, the plots of pressure coefficient are shown in Figure 5.31 or $L/D = 4-10$ of the axisymmetric underwater body based on Gertler's geometry.

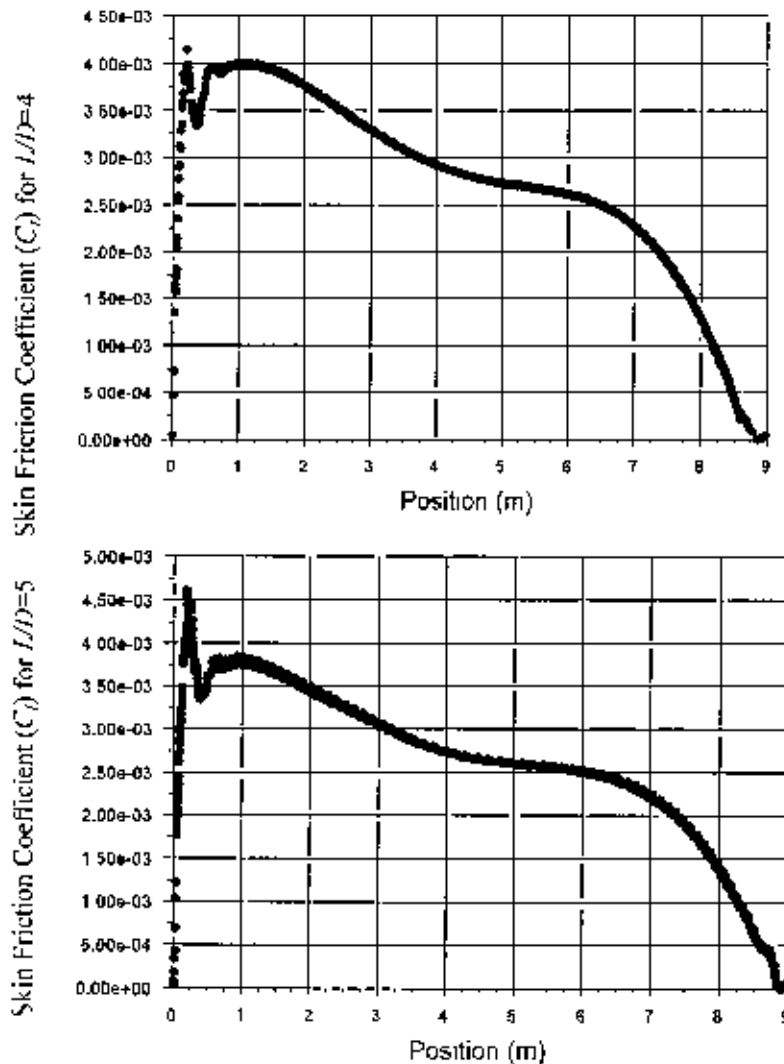


Figure 5.30(a): Effect of L/D ratio on Skin-friction Coefficient for Axisymmetric Body Based on Gertler's Geometry at $Re = 2 \times 10^7$

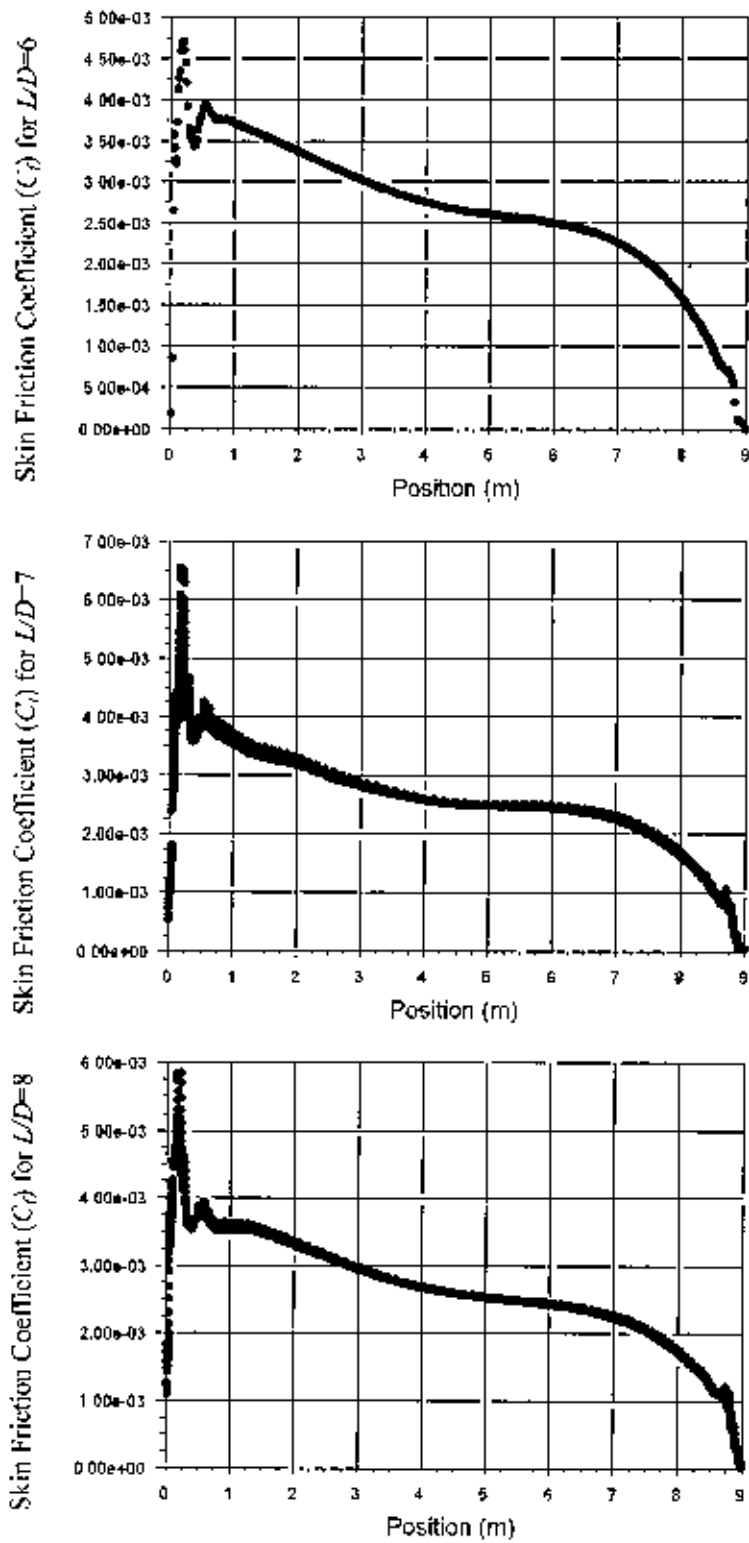


Figure 5.30(b): Effect of L/D ratio on Skin-friction Coefficient for Axisymmetric Body Based on Gertler's Geometry at $Re = 2 \times 10^7$

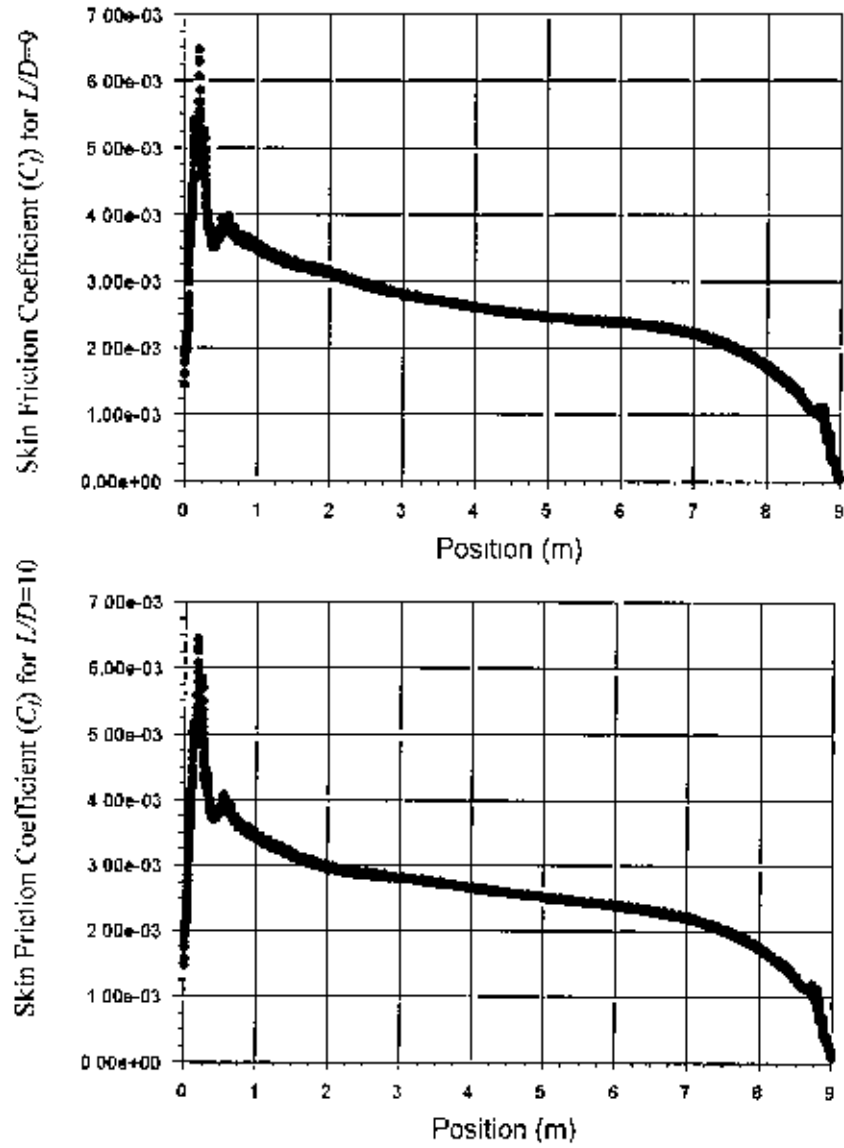


Figure 5.30(c): Effect of L/D ratio on Skin-friction Coefficient for Axisymmetric Body Based on Gertler's Geometry at $Re = 2 \times 10^7$

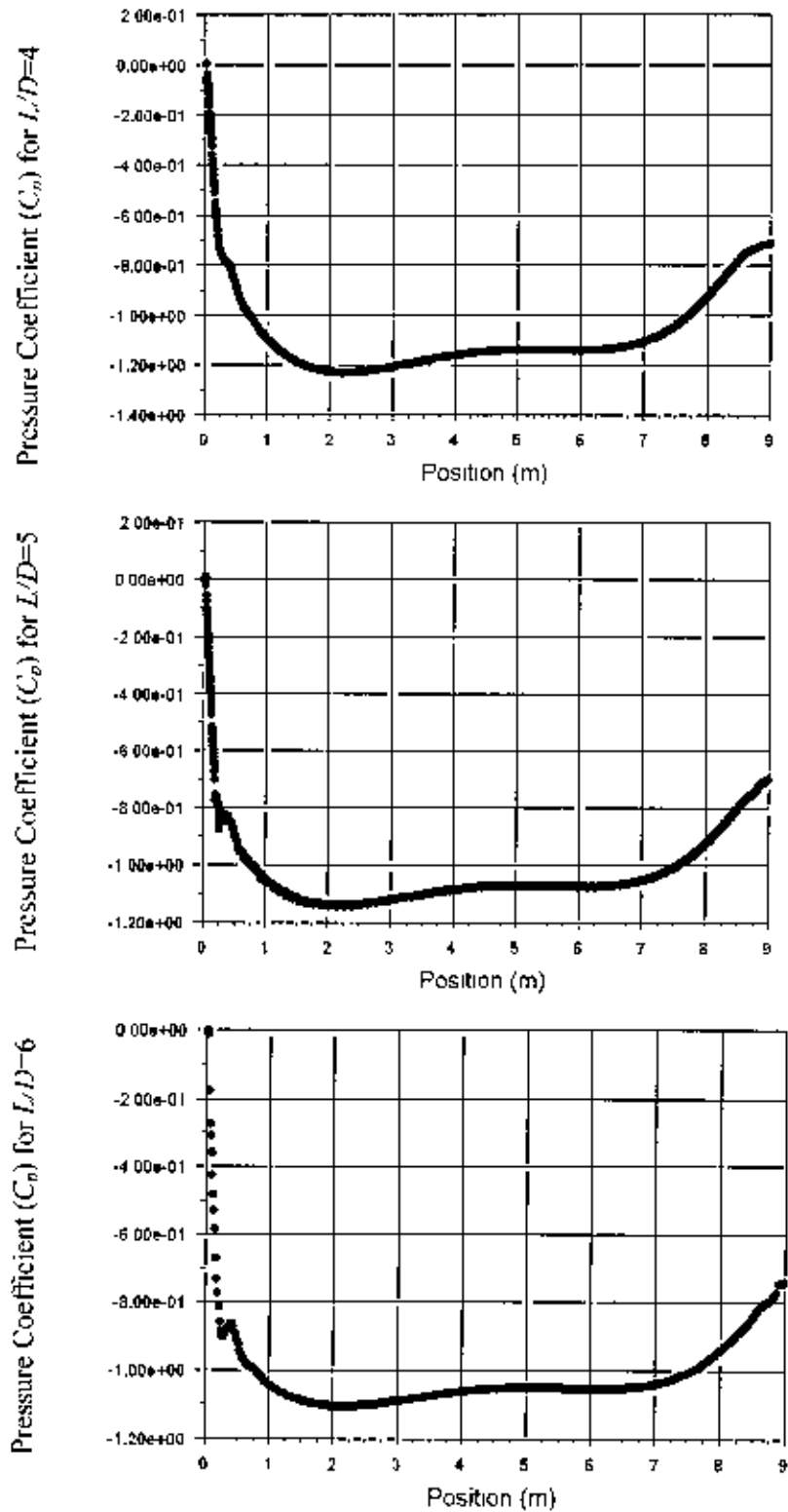


Figure 5.31(a): Effect of L/D ratio on Pressure Coefficient for Axisymmetric Body Based on Gertler's Geometry at $Re = 2 \times 10^7$

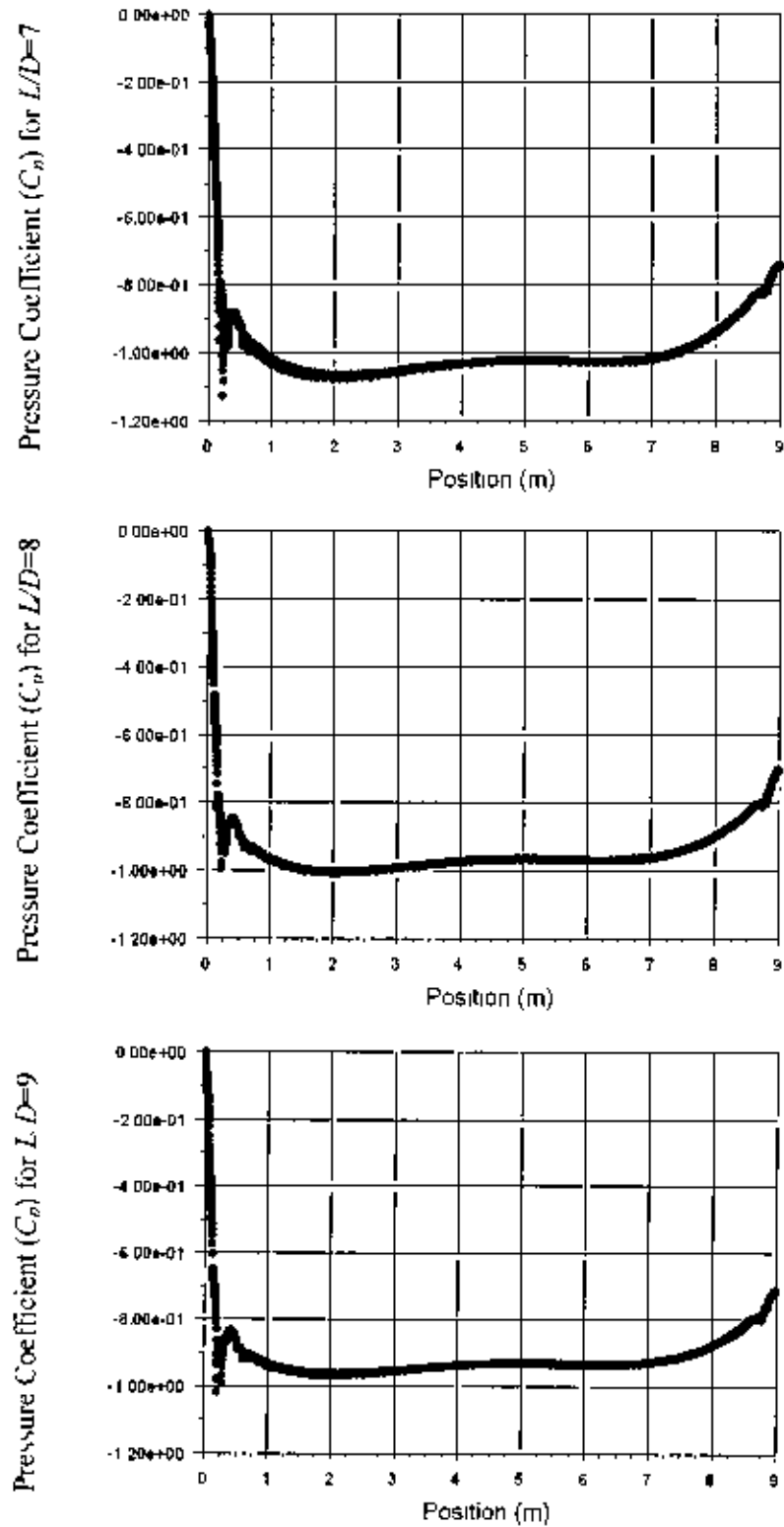


Figure 5.31(b): Effect of L/D ratio on Pressure Coefficient for Axisymmetric Body Based on Gertler's Geometry at $Re = 2 \times 10^7$

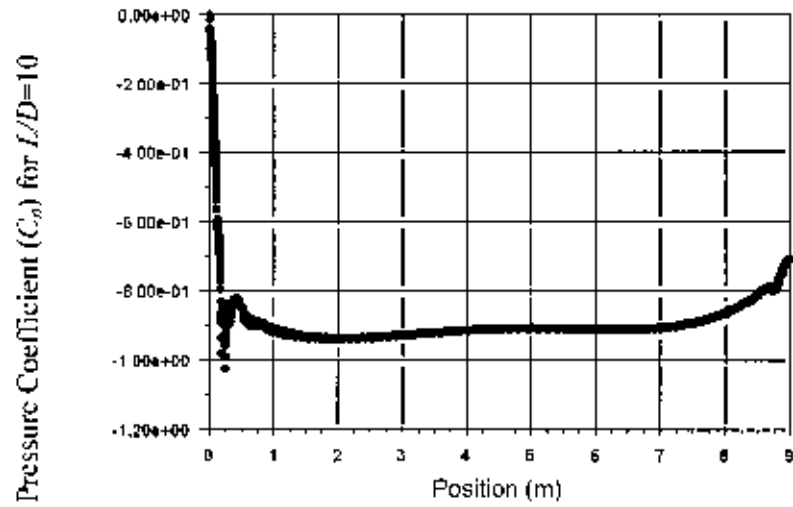


Figure 5.31(c): Effect of L/D ratio on Pressure Coefficient for Axisymmetric Body Based on Gertler's Geometry at $Re = 2 \times 10^7$

CHAPTER 6

6. CONCLUSION AND RECOMMENDATIONS

6.1 Conclusion

Two dimensional finite volume method has been applied to solve fluid structure interaction problems. Firstly laminar and turbulent flows around circular cylinder are studied and then turbulent flow around axisymmetric bodies of revolution, such as, sphere, DREA standard bare submarine hull, pod and underwater vehicle hull based on Gertler's geometry. From above studies, following conclusion can be drawn:

- (i) **Flow around Cylinder:** Flow around circular cylinder is studied at Reynold's numbers of 20, 40, 100, 1000 and 3900. At low Reynold's numbers ($Re=20, 40$ and 100), flow remains laminar but at $Re=100$, the flow in the wake of the cylinder becomes asymmetric and Karman vortex streets are found. At Reynold's number larger than 40, unsteady solver is needed to model vortex shedding in the wake of the cylinder. Drag coefficients, Strouhal numbers, wall vorticity, pressure coefficient computed by unsteady laminar flow solver at $Re=100$ agrees well with experimental/numerical results obtained by other researchers. Although most of the researchers prefer three dimensional solver to model turbulent flow at higher Reynold's number, two dimensional finite volume method as computationally cost effective is successfully applied here at $Re=1000$ & 3900 . Three turbulence models, such as, $k-\epsilon$ standard, $k-\epsilon$ Realizable and shear stress transport (SST) $k-\omega$ models are used with unsteady viscous flow solver. It is also observed that standard $k-\epsilon$ model computes drag coefficients accurately, where the realizable $k-\epsilon$ turbulence model is more effective for visualization of vortex shedding. The SST $k-\omega$ model is much more recommendable for high Reynolds numbers.
- (ii) **Flow around sphere:** Two dimensional axisymmetric flow solver is used to simulate turbulent flow around sphere at Reynold's number of 5×10^6 . Two turbulence models, such as, Spalarat-Allmaras (S-A) model and shear stress

transport (SST) $k-\omega$ model are used. Drag coefficients and separation angle computed by the implicit pressure based unsteady axisymmetric flow solver agrees well with experimental results. However, Spalart-Allmaras (S-A) turbulence model show better performance than shear stress transport (SST) $k-\omega$ model for the bodies where pressure coefficient is the major (in this case 90%) portion of total drag coefficient.

- (iii) **Flow around DREA standard submarine bare hull:** Turbulent flow around DREA standard submarine bare hull is analyzed by two dimensional axisymmetric solver at $Re = 23003039$ using shear stress transport (SST) $k-\omega$ turbulence model. The computed value of drag coefficient agrees satisfactorily with experimental results. In this case, the frictional coefficient is 79.5% of the total drag coefficient of the hull. This may be attributed due to the fact that the length-diameter ratio of the hull is very high (8.75).
- (iv) **Flow around axisymmetric pod:** The shear stress transport (SST) $k-\omega$ turbulence model is incorporated into axisymmetric solver for simulation of turbulent flow around pod surface at $Re=3 \times 10^6$. The shear stress transport (SST) $k-\omega$ turbulence model computes the value of drag coefficient more accurately than Reynold's stress model (RSM). In the present case, the frictional coefficient is 64% of the total drag coefficient of the pod.
- (v) **Flow around underwater vehicle hull based on Gertler's geometry:** Axisymmetric flow solver incorporating shear stress transport (SST) $k-\omega$ turbulence model is used to analyze the turbulent flow around underwater vehicle hull form having different L/D ratios ranging from 4 to 10 at $Re = 2 \times 10^7$. Computed values of drag coefficients agree satisfactorily with experimental values. The drag coefficient decreases with increase in L/D ratios. Also, the frictional coefficient in percentage of total drag coefficient is proportional to length-diameter ratio of axisymmetric body.

In general it can be concluded that, the shear stress transport $k-\omega$ model shows better performance than other turbulence model for bodies where the frictional force dominates the pressure drag force.

6.2 Recommendations for further study

There are many scopes for further study in this area. Some of those are:

- Free surface effects may be investigated
- The flow may be modeled for non-zero angle of attack
- More study may be done to model the laminar-to-turbulent flow transition.

REFERENCE

- Achenbach, E., "Experiments on the Flow past Spheres at Very High Reynolds Numbers". *Journal of Fluid Mechanics*, vol. 54.3, pp. 565-575, 1972.
- Anderson, J.D., *Fundamentals of Aerodynamics*, 4th Ed., Mc Grow-Hill. Columbus, USA, 2005.
- Arnone, A., Liou, M.S. and Povinelli, L.A., "Integration of the Navier–Stokes Equations using Dual Time Stepping and a Multigrid Method", *AIAA Journal* vol.33, pp. 985–990, 1995.
- Baker, C. "Estimating Drag Force On Submarine Hulls", Report. Department of Mechanical Engineering, University of new Brunswick, Canada, 2004.
- Bakic, V., *Experimental Investigation of Turbulent Flows around a Sphere*, Ph.D. Thesis, TUHH Hamburg, Germany, 2002.
- Barton I.E., "Comparison of SIMPLE- and PISO-Type Algorithms for Transient Flows", *International Journal for Numerical Methods in Fluids*, vol. 26, pp. 459-483.
- Blasius, H., "Grenzschichten in Flüssigkeiten mit kleiner Reibung", *Z. Math. Phys.* vol 56, pp. 1-37, 1908.
- Braza, M., Chassaing, P. and Minh, H.H., "The Numerical Study and Physical Analysis of the Pressure and Velocity Fields in the Near Wake of a Circular Cylinder", *J. Fluid Mech.*, vol. 165, pp. 79, 1986.
- Braza, M., Chassaing, P. and Minh, H.H., "Prediction of Large-Scale Transition features in the wake of a Circular Cylinder", *Phys. Fluids*, vol. A2 (8), pp. 1461-1471, 1990.
- Choi, J.K. and Kinnas, S., "Prediction of Unsteady Effective Wake by an Euler Solver/Vortex-Lattice Coupled Method", *Journal of Ship Research*, vol. 47, pp.131-144, 2003.
- Choi, J.K., *Vertical Inflow – Propeller Interaction Using Unsteady Three-Dimensional Euler Solver*, PhD Thesis, Department of Civil Engineering, The University of Texas at Austin, 2000.

Chomaz, J.M., Bonneton, P. and Hopfinger, E.J., "The Structure of the Near Wake of a Sphere Moving Horizontally in a Stratified Fluid", *Journal of Fluid Mechanics*, vol. 254, pp.1–21, 1993.

Department of Research and Development Canada- Atlanta, "National Defense (1998): Fall 1988 Wind Tunnel Test of the DRLA Six Meter long Submarine Model- Force Data analysis". Ottawa, 1988.

Department of Research and Development Canada- Atlanta. "National Defense (1988); Flow Visualization Test of DREA Standard Submarine Model October-November". Ottawa. 1988.

Fan, Y.S.. An Investigation of the Transonic Viscous Drag Coefficient for Axisymmetric Bodies, Masters Thesis, Naval Postgraduate School. Monterey, California, 1995.

Fluent Inc., *FLUENT 6.2 User's Guide*, 2005.

Gertler, M., "Resistance Experiments on a Systematic Series of Streamlined Bodies of Revolution for Application to the Design of High Speed Submarines", DTMB Report C-297, 1950.

Gregory, J.S., *Computational Fluid Dynamics Testing for Drag Reduction of an Aircraft Laser Turret*, Masters Thesis, Dept. of Air Force. Air Force Institute of Technology, Ohio. 2000.

Gupta, A., Numerical Prediction of Flows around Padded Propulsors, Masters thesis, Department of Civil Engineering, The university of Texas, Austin, 2004.

Hoffmann, K. A. and. Chiang, S. F., *Computational Fluid Dynamics (Third Edition)*, Vol. 2, Wichita KS: Engineering Educational System. 1998.

http://www.cfd-online.com/Wiki/Turbulence_modeling

Joubert, P.N.. "Some Aspects of Submarine Design Part 2. Shape of a Submarine 2026", Report, Department of Defense. Defense Science and Technology Organization University of Melbourne, Australia, 2006.

Kalro, V. and Tezduyan, T., "3D Computation of Unsteady Flow past a Sphere with a Parallel Finite Element Method", *Computer Methods in Applied Mechanics and Engineering*, vol.151, pp. 267–276. 1998.

- Kim, H.J. and Durbin, P.A., "Observations of the Frequencies in a Sphere Wake and of Drag Increase by Acoustic Excitation". *Physics of Fluids* vol. 31, 3260–3265, 1988.
- Kinnas, S.G.II., Gupta, A., and Lee, H., "Numerical Prediction of the Performance of Podded Propulsors and Ducted Propellers". In *Proceedings of the 13th Offshore Symposium on The Application of Emerging Technologies Offshore*. Houston, Texas, 2004.
- Kumar, V., *Introduction to Finite Volume Method*. M. Sc. Thesis, University of Erlangen-Nurnberg, Germany, 1999.
- Lakshminpathy, S., *PANS Method for Turbulence Simulation of High and Low Reynolds Number Flow Past a Circular Cylinder*. M. Sc. Thesis, Dept. of Aerospace Eng. Texas A. & M. University, USA, 2004.
- Lin, C.W., Percival, S. and Gotimer, E.H., "Viscous Drag Calculations for Ship Hull Geometry". Technical Report. Design Evaluation Branch, Hydromechanics Directorate, David Taylor Model Basin, Carderock Division Naval Surface Warfare Center, Bethesda, MD USA, 1995.
- Mishra, B., *Prediction of Performance of Podded Propulsors via Coupling of a Vortex-Lattice Method with an Euler or a RANS Solver*, Masters thesis, Department of Civil Engineering, The University of Texas, Austin, 2005.
- Payne, R.B., "Calculations of Unsteady Viscous Flow past a Circular Cylinder", *J. Fluid Mech.*, vol. 4, pp.81. 1958.
- Priyono, E., *An Investigation of the Transonic Pressure Drag Coefficient for Axisymmetric Bodies*, Masters Thesis, Naval Postgraduate School, Monterey, California, 1994.
- Rahman, M.M., Karim, M.M. and Alim M.A., "Numerical Investigation of Unsteady Flow past a Circular Cylinder using 2-D Finite Volume method". *Journal of Naval Architecture and Marine Engineering*, vol. 4, pp. 27-42, 2007.
- Reichl, P., Hourigan, K. and Thompson, M.C., "Flow Past a Circular Cylinder Close to a Free Surface", *J. Fluid Mech.* vol. 533, pp. 269-296, 2005.
- Sakamoto, H. and Haniu, H., "A Study of Vortex Shedding from Spheres in a Uniform Flow". *Journal of Fluids Engineering*, vol. 112, pp. 386–392, 1990.

- Schwabacher, G.J., Computational Fluid Dynamics Testing for Drag Reduction of an Aircraft Laser Turret. Masters thesis, Department of the Air Force, Air Force Institute of Technology, Air University, Wright-Patterson Air Force Base, Ohio, 2000.
- Sohaib M., Bilal, S. H., Rafi, S., Zahid, Z. and Khan, M., "Calculation of Flow over Underwater Bodies with Hull and Sail", 2nd Int. Bhurban Conference on applied Science and technology, Bhurban, Pakistan, 2003.
- Stern, F., Kim, H., Zhang, D., Kerwin, J., and Jessup, S., "Computation of Viscous Flow around Propeller-body Configurations: Series 60 $C_b = 0.6$ Ship Model", Journal of Ship Research, vol. 38(2), pp. 137–157, 1994.
- Sumer, B. M., "Hydrodynamics around Cylindrical Structures", World Scientific, Singapore, 1997.
- Sun, R. and Chwang, T.A., "Hydrodynamic Interaction Between a Prolate Spheroid and a Sphere", Structural Control Health Monitoring, vol.13, pp. 147–168, 2006.
- Taneda, S., "Visual Observations of the Flow past a Sphere at Reynolds Numbers Between 10^4 and 10^6 ", Journal of Fluid Mechanics, vol. 85, pp. 187–192, 1978.
- Tritton, D.J., "Experiments on the Flow around a Circular Cylinder at Low Reynolds Number", J. Fluid Mech. vol. 6, pp. 547, 1959.
- Vartdal, I., Gjerde, K. M., Bloch, F., and Sittanggang, P., "Application of Various CFD Methods in the Development of the Podded Propulsion System", presented at the International CFD Conference in Ship Hydrodynamics, Ulsteinvik, Norway, 1999.
- Versteeg, H. K. and Malalasekera, W., An Introduction To Computational Fluid Dynamics- The Finite Volume Method. Longman Scientific & Technical, England, 1995.
- White, N.M., "A Comparison between a Single Drag Formula and Experimental Drag Data for Bodies of Revolution", DTNSRDC Report 77-0028, 1977.
- White, N.M., "A Comparison between the Drags Predicted by Boundary-Layer Theory and Experimental Drag Data for Bodies of Revolution", DTNSRDC SPD-784-01, 1978.

Reference

White, F., *Fluid Mechanics*, WCH/McGraw-Hill, Toronto, 1999.

Wilcox, D.C., *Turbulence Modeling for CFD*, DCW Industries, California, USA, 1994.

APPENDICES

Appendix A:

DREA Standard Model:

Parent axisymmetric hull form: length l , maximum diameter d , $l/d = 8.75$. Profile radii are specified in three regions as shown in Figure A1:

Region 1: nose, length: $0.2l$

$$\frac{r_1(x)}{l} = \frac{d}{l} \left[2.56905 \sqrt{\frac{x}{l}} - 3.48055 \frac{x}{l} + 0.49848 \left(\frac{x}{l} \right)^2 + 3.40732 \left(\frac{x}{l} \right)^3 \right]$$

Where, $0 \leq \frac{x}{l} \leq 0.2$

Region 2: mid body, circular cylinder:

$$\frac{r_2(x)}{l} = \frac{d}{2l}, \quad \text{where, } 0.2 \leq \frac{x}{l} \leq 1 - \frac{3d}{l}$$

Region 3: tail, length: $3d$

$$\frac{r_3(x)}{l} = \frac{d}{2l} - \frac{l}{18d} \left[\frac{x}{l} - \left(1 - \frac{3d}{l} \right) \right]^2, \quad \text{where, } 1 - \frac{3d}{l} \leq \frac{x}{l} \leq 1$$

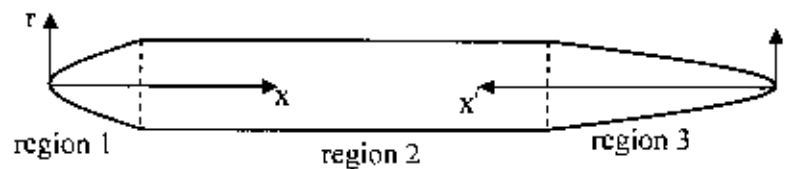


Figure A1: DREA Standard Barc Submarine Hull

Hull Volume = $0.00816191 l^3$

Hull Centre of Buoyancy at $x/l = 0.444842 l$

Appendix B:

Vertices of the pod with $L/D = 4$ used in 2D- axisymmetric run.

X	R or Y
-0.4	0.00E+00
-0.2888889	0.1017893
-0.1777778	0.1859307
-0.0666666	0.255594
0.0444444	0.3092671
0.1555558	0.3507179
0.2666668	0.3811607
0.3777778	0.4008887
0.4888889	0.4122172
0.6	0.415965
0.6222789	0.416
0.6873106	0.416
0.78982663	0.416
0.92152184	0.416
1.0717269	0.416
1.2282733	0.416
1.3784784	0.416
1.5101736	0.416
1.6195069	0.416
1.72884	0.416
1.8381736	0.416
1.940689	0.416
2.005721	0.416
2.028	0.4159999
2.127662	0.4127163
2.227324	0.4019396
2.326986	0.3824254
2.426648	0.3527355
2.526309	0.311508
2.625971	0.2573541
2.725633	0.1888398
2.825295	0.1048245
2.924951	3.38E-03
2.928	0

Appendix C:

Axisymmetric underwater body based on Gertler's geometry

Formula: $y^2 = a_1x + a_2x^2 + a_3x^3 + a_4x^4 + a_5x^5 + a_6x^6$

$$a_1 = +1.000000$$

$$a_2 = +2.149653$$

$$a_3 = -17.773496$$

Where $a_4 = +36.716580$

$$a_5 = -33.511285$$

$$a_6 = +11.418548$$

Model Particulars:

(i) $L/D = 4$

Length (m)	9.000
Diameter (m)	2.250
Wetted surface area (m ²)	50.18

(ii) $L/D = 5$

Length (m)	9.000
Diameter (m)	1.800
Wetted surface area (m ²)	39.75

(iii) $L/D = 6$

Length (m)	9.000
Diameter (m)	1.500
Wetted surface area (m ²)	32.94

(iv) $L/D = 7$

Length (m)	9.000
Diameter (m)	1.286
Wetted surface area (m ²)	28.15

(v) $L/D = 8$

Length (m)	9.000
Diameter (m)	1.125
Wetted surface area (m ²)	24.58

(vi) $L/D = 9$

Length (m)	9.000
Diameter (m)	1.000
Wetted surface area (m ²)	21.78

(vii) $L/D = 10$

Length (m)	9.000
Diameter (m)	0.900
Wetted surface area (m ²)	19.64

